Numerical Studies of Three-Dimensional Equilibrium and Stability for Stellarator/Heliotron Configurations

Katsuji Ichiguchi

1989

Numerical Studies of Three-Dimensional Equilibrium and Stability for Stellarator/Heliotron Configurations

Katsuji Ichiguchi

1989

Abstract

The magnetohydrodynamic (MHD) equilibrium and stability for the three-dimensional stellarator/heliotron configurations are investigated mainly with numerical approaches.

By using the three-dimensional MHD code, BETA code, we study both the currentless and flux conserving torus (FCT) equilibria and ideal stability against the $m = 1$ and $n = 1$ internal mode in a Heliotron E model configuration, where m and n are poloidal and toroidal mode numbers, respectively. The beta limit of the first stability region is $\bar{\beta} \lesssim 2\%$, where $\bar{\beta}$ denotes an average beta value. For $\bar{\beta} \gtrsim 5\%$, a second stability region appears. It is found that the stability is sensitive to additional vertical magnetic fields. When the magnetic axis is shifted inward, the stability degrades, whereas, when it is shifted outward, the instability disappears for the above range of beta values. The stability is also examined in another heliotron configuration which has a rotational transform larger than unity for all flux surfaces. Its first stability beta limit is larger than that for the Heliotron E. For this configuration, an unstable free boundary mode with $m = 1$ and $n = 1$ is found.

The MHD equilibrium and local stability of a spatial axis stellarator with a circular cross section, Asperator NP-4, are also calculated by using the BETA code. The equilibrium results are compared with analytic expressions given by Solov'ev and Shafranov to examine the applicability of the theory. Agreements are found with respect to the equilibrium properties, such as the rotational transform, the shift of magnetic axis due to the finite pressure, and the formation of a magnetic well. Toroidal effects on both the curvature

and the torsion of the spatial magnetic axis must be estimated analytically with sufficient accuracy to obtain agreement.

The stability code named RESORM solving the reduced MHD equations as the initial value problem is developed so as to examine the resistive instabilities in the toroidal stellarator/heliotron configuration. Intrinsically this code can be applied to the ideal instabilities by assuming zero resistivity. Currentless equilibria in the Heliotron DR plasma are investigated by applying this code and the STEP code. It is found that the critical beta value determined by the ideal global modes is $\beta_0 \simeq 1.2\%$ by the both codes and the Mercier criterion by the STEP code gives $\beta_0 \simeq 0.7\%$, where β_0 is a beta value at the magnetic axis. By the RESORM code the resistive modes become unstable with substantial growth rates for $\beta_0 < 1.2\%$, since the magnetic Reynolds number is not large, $S \sim 10^5$, in Heliotron DR. For the Mercier stable beta value of $\beta_0 < 0.7\%$, the growth rate is proportional to $S^{-1/3}$, while in the Mercier unstable region the S-dependence deviates from this one because of the effects of the ideal instability. The effect of the magnetic axis shift on the ideal and resistive MHD stability is also studied by the both codes.

The numerical results by the above mentioned codes are compared with the experimental data in both Heliotron E and Heliotron DR. The experimental stability beta limit is a little lower than the theoretical low n ideal mode stability result. It is concluded that the resistive interchange mode is the crucial instability in heliotron configurations and the MHD fluctuation including the internal disruption is excited by this mode at beta value lower than the ideal stability limit.

Acknowledgements

I would like to thank Emeritus Professor H.Nishihara and Professor T.Obiki for providing me the opportunity to study the plasma physics as my graduate work. I am also indebted to Emeritus Professor K.Uo and Professor A.Iiyoshi for affording me the chance to study the Heliotron E and Heliotron DR theoretically.

I wish to express my greatest gratitude to Professor M.Wakatani for guiding me with his patient support. Without his many useful suggestions and encouragements with generosity all over my work, the completion of this thesis would not have been possible.

I would like to acknowledge the encouragements and useful comments by Professor M.Fukao and Professor K.Itoh. I would like to thank Professor I.Kimura and Professor M.Sato for useful comments on the manuscript.

I am very grateful to Professor P.R.Garabedian for many valuable suggestions about the BETA code. It is a pleasure to thank Doctor J.L.Johnson for fruitful discussions about the analyses of the spatial axis stellarators. I would also like to thank Doctor B.A.Carreras for useful comments on some aspects of my numerical results.

I have much helped by Doctor Y.Nakamura in the computational works and the theoretical background of the STEP code. I thank Doctor H.Sugama and M.Yagi for useful discussions about the theoretical analyses of MHD instabilities. I am also indebted to Professor S.Morimoto, Doctor H.Zushi and N.Yanagi for many useful discussions about the experimental results in Heliotron E and Heliotron DR.

I also acknowledge encouragements and supports by all members of Plasma Physics Laboratory in Kyoto University and the plasma physics group at Nuclear Engineering Department in Kyoto University.

Finally, I would like to thank Miss M.Okuda for her assistance of typing this thesis.

Contents

Chapter 1

Introduction

1.1 Motivation

Recently, many efforts have been made for the thermonuclear fusion research using the magnetically confined plasmas. The most successful experimental data have been obtained in the large tokamak devices such as JET(EC), TFTR(USA) and JT–60(Japan). The geometrical property in the tokamak configuration with axisymmetry makes theoretical studies analytically tractable. In order to confine high temperature plasmas in toroidal systems, nested magnetic surfaces are necessary or existence of MHD equilibrium is required. In axisymmetric tokamaks, a toroidal plasma current is driven to provide a poloidal magnetic field which is crucial to construct the magnetic surfaces. However, existence of such a plasma current in tokamaks introduces current driven MHD instabilities when it exceeds a threshold

value. Usually the maximum current is limited by the disruptive instability which releases almost all thermal energy in a short time on the order of 100 μsec. The disruption is universal and seen in every tokamak. Another difficulty is that a non-inductive current drive is required to realize continuous operation of tokamak. This is one of the current research subjects in tokamaks and there is no final solution with reasonable efficiency at present.

From the point of the continuous operation without the disruption the stellarator/heliotron configuration is an alternative approach. The experimental studies for the devices of this type have been made significant progress recently. Heliotron E at Kyoto University (Japan) is one of the largest stellarator/heliotron devices [1]. The concept of this configuration is characterized by that nested magnetic surfaces are generated by only the external windings and the global plasma current is not necessary. Also it has a large rotational transform and a high shear. Thus confined plasmas become non-axisymmetric and theoretical analyses become more complicated than those in tokamaks. Since the plasma can be confined without the global current, the stellarator/heliotron is free from the disruptive instability. We can operate the machine continuously, in principle, if super-conductive coils are equipped.

In Heliotron E experiments of 1983 [2], sawtooth-like fluctuations and internal disruptions are observed in the soft X ray measurement which have coincidence with magnetic fluctuations. At the internal disruption 20 $\sim$ 30% of plasma energy is lost by the enhancement of the energy and particle transport. One of our main concerns is what type of instability triggers the internal disruption and what is the threshold beta value for such an

instability. We study MHD equilibrium and stability problems in several stellarator/heliotron configurations with the numerical methods. In order to explore the applicability of the MHD model to the stellarator/heliotron, we compare our theoretical results with the experimental data of Heliotron E and Heliotron DR.

The MHD equations are obtained from the moment equations of the Boltzmann equation for the velocity distribution function with the Maxwell distribution under the assumptions of small gyroradii, high collisionalities, and lower characteristic frequencies than plasma oscillations [3]. Thus MHD becomes a useful model in describing the macroscopic dynamics of magnetically confined plasmas, although the kinetic effects are completely eliminated to simplify the model.

When we investigate the toroidal plasma based on the MHD equations, we let the plasma be initially in a static MHD equilibrium where the force balance is satisfied at any point on nested flux surfaces. Since the MHD equilibrium properties are related to a design of magnetic field coils, we investigate them in stellarator/heliotron configurations numerically by including the three-dimensional geometry with sufficient accuracy.

In order to confine high temperature plasmas long enough to achieve the Lawson criterion for the self-ignition of the thermonuclear fusion[4], the equilibrium must be stable for all possible perturbations. When the plasma is unstable to a global perturbation with a large growth rate, it will grow to such a high level that the plasma confinement is deteriorated by it. Thus it is also crucial to examine whether the obtained equilibrium is stable or not. The pressure driven instability becomes the most dangerous one in the

stellarator/heliotron configuration without the net toroidal current. This type of instability depends on beta value and pressure profile. The average beta value is defined by the volume average of the ratio of the internal plasma pressure, P, to the magnetic pressure, $B^2/2\mu_0$, as

$$\bar{\beta} = \int \frac{P}{B^2/2\mu_0} dV, \tag{1.1}$$

which represents efficiency of the magnetic field to confine a plasma. Although a high beta plasma is attractive from the fusion reactor point of view, free energy related to the plasma pressure increases according to the increase of beta and pressure gradient, and it may cause the MHD instabilities for $\bar{\beta} > \bar{\beta}_c$, where $\bar{\beta}_c$ is called the critical beta. We study the correlation between the theoretical value of $\bar{\beta}_c$ and the appearance of MHD fluctuations.

Usually high temperature and low density plasmas can be assumed to have infinite conductivity. The instabilities under this assumption are called ideal ones. In the ideal MHD model, the perturbations grow with keeping the topology of the magnetic field. In the low temperature and high density plasmas, the resistivity may not be negligible in the MHD stability analysis. It is known that small resistivity significantly changes the properties of MHD instabilities in sheared magnetic fields[5]. This type of instabilities occurs even in plasmas stable to ideal MHD instabilities. They are called resistive modes or resistive instabilities. Since the resistivity dissipates the current, resistive instabilities are accompanied with reconnection of magnetic field lines or topology change of magnetic surfaces. In the beta limit study, both contributions from the ideal and resistive instabilities will be analyzed in this thesis.

The stellarator/heliotron configurations do not have geometrical symmetry like tokamaks. Thus, the analyses of the equilibrium and the stability become three-dimensional intrinsically. For MHD studies in non-symmetric stellarator/heliotron, two kinds of theoretical approach have been developed. One is the method using the stellarator ordering and the averaging over the helical ripples in the toroidal direction . Originally an averaged equilibrium equation and the energy principle for ideal linear stability in stellarators were derived by using the stellarator expansion[6,7]. Recently it is recognized that reduced MHD equations can also be derived based on the stellarator expansion. This method has the merit to exploit the numerical techniques developed in tokamak equilibrium and stability studies because the helical variations in the toroidal direction are averaged out and only the axisymmetric part remains. The other approach is the numerical calculation to solve the three-dimensional MHD equations directly. In this scheme realistic three-dimensional geometry can be included principally, however, it usually takes a long computation time and requires a large region in the core memory in order to obtain accurate results. Without super-computers it is impossible to use the three-dimensional code efficiently. We used FACOM VP-100 first in 1985. After that we used more efficient VP-200 and VP-200E super computers.

In this thesis we pursue both approaches. At first, we apply the three-dimensional equilibrium, stability and transport code, or the BETA code developed by Bauer, Betancourt and Garabedian [8,9] to investigate the ideal equilibrium and stability, to heliotron configurations and a spatial axis stellarator. For the approach using the stellarator expansion, we use the STEP

code developed by Anania and Johnson [10,11] to study the ideal equilibrium and ideal stability of Heliotron DR. We have developed the RESORM code in order to study both the ideal and resistive instabilities based on the reduced MHD equations. Finally, comparison between the theoretical and experimental results is carried out for Heliotron E and Heliotron DR. Top views of the helical and vertical coils in these devices are shown in Fig.1.1 and Fig.1.2.

1.2 Brief history of MHD studies for stellarator/heliotron configurations

As mentioned in Sec.1.1, there is no geometrical symmetry in stellarator/heliotron configurations. Consequently various approximations were tried to study MHD equilibrium and stability in obtaining analytically tractable expressions. The most successful approximation was the stellarator expansion method developed by Greene and Johnson [6]. They assumed that the magnetic field can be expanded with the inverse aspect ratio, $\epsilon = \bar{a}/R \ll 1$, where $\bar{a}$ and R are an average minor radius and major radius, respectively. With this ordering parameter, it is assumed that the helical field generated by the helical windings has the order of $\epsilon^{1/2}$ and $\bar{\beta} \sim O(\epsilon)$. These two points are essential in the stellarator expansion and called stellarator ordering. Applying this ordering to the MHD equilibrium equations, the equation similar to the Grad-Shafranov equation can be derived for the stellarator/heliotron. The stellarator ordering is also applicable to the energy principle[12] which is used to study the linear stability of equilibria obtained from the Grad-Shafranov type equation[7].

The equilibrium equation derived by Greene and Johnson is essentially two dimensional after helical variations along the toroidal direction are averaged out in the stellarator expansion. This property makes numerical schemes for the MHD studies of tokamaks usable for stellarator/heliotron configurations. Anania and Johnson developed the STEP code[10,11] based

on the stellarator expansion method to study the MHD equilibrium and the ideal MHD stability of stellarator plasmas by modifying the PEST code[13, 14] for ideal MHD instabilities in tokamaks. Furthermore, Nakamura et al. modified the STEP code[15] by including higher order toroidal corrections in order to apply the code to the low aspect ratio devices with $R/\bar{a} \gtrsim 5$.

Kovrizhnykh and Shchepetov[16] independently derived the equilibrium equation by averaging the helical field without the stellarator ordering, and their approach is an extension of the stellarator expansion and called stellarator approximation. Carreras et al.[17] also derived the Grad-Shafranov type equation by using the approximation similar to Kovrizhnykh and Shchepetov. These equations are essentially same as the one derived by Greene and Johnson, when the higher order terms with respect to ϵ are neglected. Todoroki[18] developed the HERATO code based on the stellarator approximation and the coordinate transformation to study the ideal linear stability. It is considered as an extension of the ERATO code[19] based on the energy principle for tokamaks to stellarators.

The above mentioned stellarator expansion or stellarator approximation is already established for the planner axis helical configurations such as standard stellarators, heliotrons and torsatrons. However, we cannot apply the same approximation directly to spatial axis stellarators because helical excursions of the spatial axis is usually large to produce a deep magnetic well and large rotational transform per field period. This point is beyond the assumption for the usual stellarator expansion. Solov'ev and Shafranov used a curvilinear coordinate system and derived the equation for the Shafranov shift, or the shift of the magnetic axis due to the plasma pressure, by applying

the perturbation method to the MHD equilibrium equation in the neighborhood of the helical magnetic axis[20]. Hender and Carreras[21] divided all equilibrium functions into the averaged part and the rapidly oscillating part in the magnetic coordinates. They obtained the Grad-Shafranov type equation for the averaged part. A Poisson type equation was also derived for obtaining the rapid oscillating part. When both solutions are obtained, an equilibrium including three-dimensional structures is realized. Koniges and Johnson[22] exploited a modified ordering to include the helical excursion of the spatial axis stellarator in the stellarator expansion approach. Here they assumed that rotational transform per field period is small, which gives a limitation on the application of this method.

In order to study the nonlinear dynamics of resistive instabilities in tokamak plasmas, the initial value approach based on the reduced MHD equations has been successfully developed. By using the high-beta tokamak ordering of $\bar{\beta} \sim \epsilon$, the incompressible MHD equations are reduced to the three-field fluid equations for a poloidal flux, a stream function and a pressure[23]. For stellarators Strauss[24] employed the stellarator ordering in the reduction process of the MHD equations and applied the averaging method for the helical variations to obtaining the final reduced MHD equations. Wakatani[25] expressed an effective poloidal flux and an average curvature due to the helical magnetic field in terms of the rotational transform in the vacuum configuration based on the stellarator expansion method, and derived the reduced MHD equations equivalent to those by Strauss by adding these terms to the tokamak reduced MHD equations. The incompressible MHD equations without the ordering with respect to the aspect ratio are derived recently, which are

straightforwardly reduced to the three-field reduced MHD equations by introducing the stellarator ordering. A numerical code solving the incompressible MHD equation has been developed by Oak Ridge MHD group as the initial value problem , which is called FAR code [26].

On the other hand, several numerical codes to obtain the three-dimensional equilibria without any averaging procedure and to examine the stability of them have been developed successfully with the recent development of the super-computer equipped vector processors. Almost all the three-dimensional codes adopt the variational principle that the MHD equilibrium corresponds to the minimum energy state of the potential energy with the constraint of currentless equilibrium or FCT equilibrium[27], and use the Richardson method or the conjugate gradient method to guarantee monotonical decrease of the potential energy.

There are two types in the codes with respect to the choice of the coordinate system. One uses the spatially fixed Eulerian coordinates. This case has an advantage capable to study equilibria including magnetic islands or stochastic region of magnetic field lines. A pioneer work was given by Chodura and Schlüter[28] who developed the three-dimensional code using the Eulerian cylindrical coordinates with a fixed boundary at a toroidal chamber with rectangular cross section. They introduced a virtual displacement $\boldsymbol{\xi}$ and calculated density and the magnetic field variations due to $\boldsymbol{\xi}$ from both the equation of continuity and Faraday's law under the adiabatic change of the pressure. At each step, the residual force $\mathbf{F}$ is calculated from the force balance equation and the new displacement is given by $d\boldsymbol{\xi}/dt = \alpha\mathbf{F}$. The iteration procedure is continued until the residual force vanishes. This nu-

merical scheme is called a friction model because α corresponds to a role of friction in the relaxation process to an equilibrium state. For a spatial discretization usual finite difference scheme is employed in three directions of the coordinates. Unfortunately, this numerical scheme given by Chodura and Schlüter showed a slow convergence to the equilibrium and it is difficult to use this code for parameter survey to optimize stellarator/heliotron configuration.

As an extension of the Chodura-Schlüter code NEAR code [29] was developed by Oak Ridge MHD group. Its numerical scheme is very similar to that in the Chodura-Schlüter code; however, accuracy is improved significantly by using the magnetic coordinates called Boozer coordinates[30]. In both the poloidal and the toroidal directions of the Boozer coordinates Fourier expansion method was used to describe the displacement $\boldsymbol{\xi}$. They employ the conjugate gradient method to obtain the minimum energy state instead of the friction method. While only the flux conserving equilibria can be obtained by the Chodura-Schlüter code due to the iteration including Faraday's law, the NEAR code can obtain the currentless equilibria as well as the FCT equilibria by adding the outer loop eliminating the net toroidal current on each flux surface. Recently Harafuji et al.[31] are trying to solve the time dependent MHD equations in the three-dimensional geometry to determine the equilibrium without assumption of the existence of nested flux surfaces.

The other choice for the coordinates in the three-dimensional codes is to use Lagrangian coordinates where a radial coordinate is always characterized by the flux surfaces at finite beta equilibrium. In this case, existence of the flux surface is assumed a priori and the equation for the spatial position

of the constant flux surface is solved. This numerical technique is called the inverse solver. The existence of the ideal MHD equilibrium with the nested surfaces in non-symmetric three-dimensional system is a sophisticated problem and the existence theorem seems to be negative. The results given by the three-dimensional codes assuming the nested flux surfaces are acceptable in the three-dimensional system having a helically symmetric system in its geometrical neighborhood.

The first successful implementation of this approach was the BETA code [32] which was developed by the Courant Institute group at New York University. They followed strictly the variational principle of the MHD equilibrium in the development of the code. The BETA code also includes a package to study ideal MHD stability of the equilibrium by adding the assumed perturbation to the equilibrium and trying the second minimization of the potential energy. The details of this code is given in Chapter 2. Based on the idea of the BETA code, Hirshman et al. have developed the VMEC code[33] with the spectral method. The minimization scheme is similar to that of the BETA code. By following the VMEC code Betancourt is developing the BETAS code[34] which is a version of the BETA code based on the spectral method. A similar spectral code was developed by GA group[35]; however, published papers including the numerical results are limited. Other efforts to develop the three-dimensional codes were given by Max-Planck people [36] and Russian group [37].

1.3 Outline of this thesis

The contents of this thesis is organized in the following way.

In Chapter 2, we explain mathematical basis and numerical procedures of the three-dimensional code, BETA code, with which we calculate the MHD equilibrium and stability of heliotron configurations and a spatial axis stellarator in Chapters 3 and 4, respectively. First, the variational principle given by Kruskal and Kulsrud[27] for MHD equilibrium with the fixed boundary condition is reviewed briefly and is extended to the free boundary case. Then the Euler equations to minimize the potential energy are derived in the flux coordinates used in the BETA code. We refer to the steepest descent method for the numerical scheme of the energy minimization. A second minimization of the potential energy to study global ideal MHD instabilities is also discussed.

In Chapter 3, we apply the BETA code to both the Heliotron E and Heliotron H configurations. Because the magnetic surface with the rotational transform of $\iota = 1$ always exists in the plasma column of the Heliotron E, we consider that the $m = 1$ and $n = 1$ mode resonant at the surface is the most dangerous mode, where m and n are the poloidal and the toroidal mode numbers, respectively. We examine the global stability for both types of equilibrium, currentless and FCT equilibria. As a configuration where rotational transform exceeds unity everywhere in the plasma column, we choose the Heliotron H and examine the stability for the non-resonant $m = 1$ and $n = 1$ mode. We also study the effects of the magnetic axis shift due to

the additional vertical field on the $m = 1$ and $n = 1$ mode.

In Chapter 4, we investigate MHD equilibrium of the spatial axis stellarator, Asperator NP-4, at Tohoku University (Japan) by two approaches. We evaluate the equilibrium quantities of the Asperator NP-4 plasma based on the Solov'ev-Shafranov theory[20] analytically, and compare them with those obtained numerically be using the BETA code. We also calculate the Mercier criterion for localized pressure-driven modes with the BETA code, and compare the stability properties of the Asperator NP-4 with those of Heliotron E.

In order to study the linear stability for the resistive global modes we develop a code based on the initial value problem of the reduced MHD equations called the RESORM code. We explain mathematical basis and numerical procedures of this code in Chapter 5. We reduce incompressible resistive MHD equations to the three-field equations for torsatron/heliotron configurations by following the Strauss' approach[24]. In this reduction we include higher order corrections which are usually assumed to be small in the stellarator ordering. The stellarator equilibrium equation is obtained from the reduced equations. In this code we employ the flux coordinates based on both the existence of nested flux surfaces and the condition that magnetic field lines are expressed as straight lines on the flux surface, and write the linearized reduced MHD equations in this coordinate system. We explain briefly the structure of the RESORM code.

In Chapter 6, we study both the ideal and the resistive stability of Heliotron DR plasmas. The equilibrium is obtained numerically from the stellarator equilibrium equation derived in Chapter 5 with the STEP code[15].

We can examine the ideal stability by both the STEP code and the RESORM code with zero resistivity. For the resistive stability we apply the RESORM code by assuming a finite resistivity. The effects of the additional vertical field on the behaviors of both the ideal and resistive modes are also studied.

We compare the numerical results obtained in this thesis with the experimental data in Heliotron E and Heliotron DR devices in Chapter 7. We can explain the observed MHD activities in both devices with our theoretical results.

The concluding remarks of this thesis are given in Chapter 8.

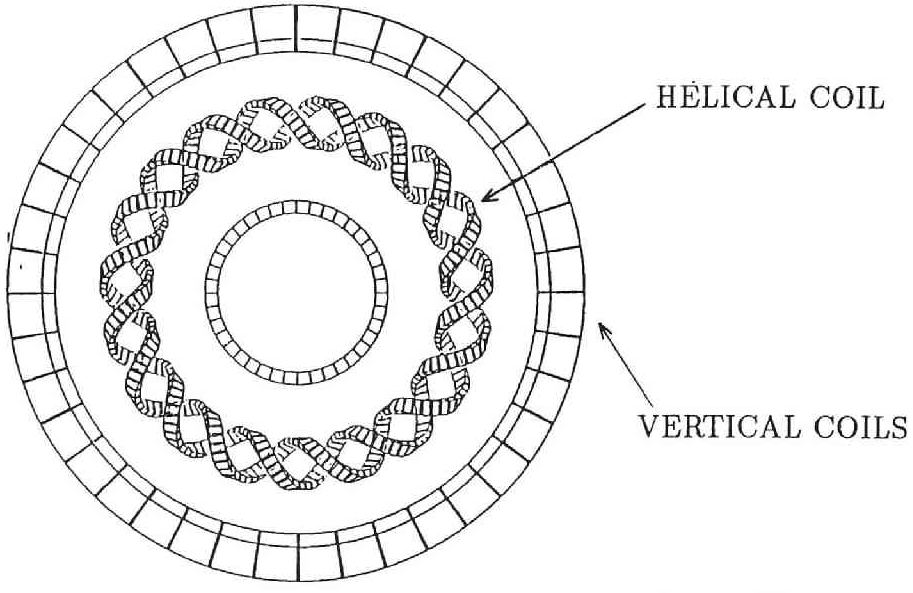

Fig.1.1 Top view of helical and vertical coils in Heliotron E.

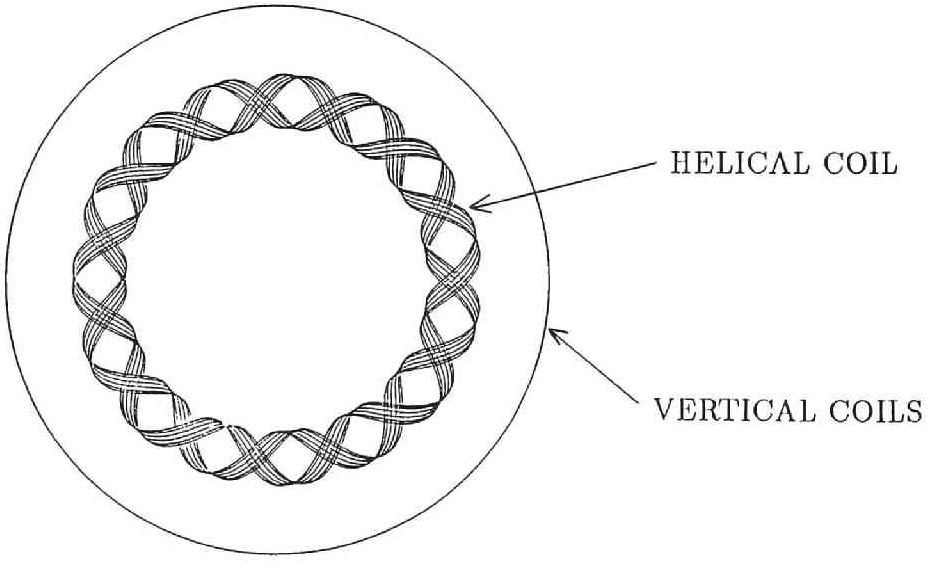

Fig.1.2 Top view of helical and vertical coils shown by filaments in Heliotron DR.

Chapter 2

Variational Approach for Three-Dimensional Ideal MHD Equilibrium and Stability

2.1 Introduction

In the ideal MHD analysis, the plasma is assumed to be governed by the equations,

$$\frac{\partial \rho_m}{\partial t} + \nabla \cdot (\rho_m \mathbf{v}) = 0, \qquad \text{(equation of continuity)} \tag{2.1}$$

$$\rho_m \frac{d\mathbf{v}}{dt} = -\nabla P + \mathbf{J} \times \mathbf{B}, \qquad \text{(momentum equation)} \tag{2.2}$$

$$\frac{dP}{dt} + \Gamma P \nabla \cdot \mathbf{v} = 0, \qquad \text{(adiabatic equation of state)} \tag{2.3}$$

$$\mathbf{E} = -\mathbf{v} \times \mathbf{B}, \qquad \text{(Ohm's law)} \tag{2.4}$$

$$\frac{\partial \mathbf{B}}{\partial t} = -\nabla \times \mathbf{E}, \qquad \text{(Faraday's law)} \tag{2.5}$$

$$\mathbf{J} = \nabla \times \mathbf{B}, \qquad \text{(Ampère's law)} \tag{2.6}$$

$$\nabla \cdot \mathbf{B} = 0, \tag{2.7}$$

where

$$\frac{d}{dt} \equiv \frac{\partial}{\partial t} + \mathbf{v} \cdot \nabla. \tag{2.8}$$

Here $\mathbf{v}$ is the velocity of the fluid element, ρ_m is the mass density, P is the thermal pressure and Γ is the ratio of the specific heats. $\mathbf{B}$, $\mathbf{E}$ and $\mathbf{J}$ are the magnetic field, the electric field and the current density, respectively. The MKS units with μ_0=1 are used, where μ_0 is the magnetic permeability.

The static MHD equilibrium without macroscopic flows is expressed by the following set of equations,

$$\nabla P = \mathbf{J} \times \mathbf{B}, \tag{2.9}$$

$$\mathbf{J} = \nabla \times \mathbf{B}, \tag{2.10}$$

$$\nabla \cdot \mathbf{B} = 0, \tag{2.11}$$

which are obtained from eqs.(2.1) $\sim$ (2.7) by assuming $\partial/\partial t$=0 and $\mathbf{v}$=0. In the three-dimensional geometry with no symmetry, we cannot reduce eqs.(2.9) $\sim$ (2.11) to a generalized differential equation such as the Grad-Shafranov equation obtained under the assumption of axisymmetry or helical symmetry. This equation has solutions with nested flux surfaces and they are obtained by applying a Poisson solver. For the asymmetric case the MHD equilibrium is formulated by noting that it corresponds to the minimum energy state of the potential energy (see eq.(2.18)). Kruskal and Kulsrud[27]

proved that the plasma in the minimum energy state satisfies eqs.(2.9) $\sim$ (2.11) under the fixed boundary condition by considering the variation of the potential energy functional defined by a sum of internal energy and magnetic energy. However, there is the subtle problem for the existence of nested flux surfaces in the three-dimensional geometry and no mathematical proof to confirm it. Practically we believe that it is possible to produce nested flux surfaces if a deviation from a symmetric state with axisymmetry or helical symmetry is sufficiently small. Therefore, if we find the minimum energy state under the assumption of existence of nested flux surfaces, it means that we obtain the three dimensional MHD equilibrium solution of eqs.(2.9) $\sim$ (2.11). This is the variational principle approach to obtain MHD equilibrium. It can be extended to the problem of MHD equilibrium surrounded by a vacuum region or the free boundary equilibrium problem. This approach was implemented in the BETA code to calculate the three-dimensional stellarator equilibrium, where the potential energy for one pitch length of the stellarator is actually minimized by assuming periodicity.

The same potential energy is also used to study the nonlinear global stability in the BETA code. Here it is minimized again by considering the whole toroidal stellarator plasma or the full torus. In the standard linear stability analysis based on the variational principle, the second variation of the potential energy is used to obtain the eigenvalue (or growth rate) and the eigenfuncion. On the analogy of the linear stability analysis using the energy principle, the difference between the potential energy corresponding to the equilibrium and the secondary minimized potential energy is interpreted as the second variation in the nonlinear stability case. The potential energy for

studying the stability includes both perturbed functions with finite amplitude and the background equilibrium contributions, and it is minimized under the linear constraint for the perturbed functions. Then, if the minimum energy of the perturbed state is larger than the minimum energy of the equilibrium state, the equilibrium is stable to the given perturbation, and if the former is smaller than the latter, the equilibrium is unstable. This is a picture of the nonlinear stability analysis in the BETA code.

In Sec.2.2, we review briefly the proof for the variational principle given by Kruskal and Kulsrud under the fixed boundary condition and extend the variational principle to the free boundary case in Sec.2.3. In Sec.2.4, we introduce the flux coordinates and discuss the Euler equations that are used in the BETA code. In Sec.2.5, the numerical method to minimize the potential energy is described. In Sec.2.6, we explain the method of the nonlinear stability based on the variational method.

2.2 Variational principle for MHD equilibrium under the fixed boundary condition

From an analogy of a particle motion in a potential field, the static MHD equilibrium corresponds to the minimum potential energy state under the appropriate constraints. Kruskal and Kulsrud proved that the stationary state of the potential energy W_p is equivalent to equilibrium state without flow given by eqs.(2.9) $\sim$ (2.11) based on the variational method[27]. We review this proof briefly.

A local conservative form for the energy of the ideal MHD can be written by

$$\frac{\partial}{\partial t}\left(\frac{\rho_m v^2}{2}+\frac{B^2}{2}+\frac{P}{\Gamma-1}\right)+\nabla\cdot\left[\left(\frac{\rho_m v^2}{2}+\frac{\Gamma P}{\Gamma-1}\right)\mathbf{v}+\mathbf{E}\times\mathbf{B}\right]=0. \quad (2.12)$$

In this section, the boundary condition is posed by assuming that a magnetically confined plasma extends to a rigid perfect conducting wall. This case is called a fixed boundary. It requires that the tangential electric field, the normal magnetic field and the normal component of velocity on the wall vanish and they are expressed as

$$\mathbf{n}\times\mathbf{E}=0, \quad (2.13)$$

$$\mathbf{n}\cdot\mathbf{B}=0, \quad (2.14)$$

$$\mathbf{n}\cdot\mathbf{v}=0. \quad (2.15)$$

By integrating eq.(2.12) over the whole plasma, it is shown that the second term vanishes because of the above fixed boundary conditions. Then we obtain the global energy conservation relation,

$$\int_p \left(\frac{\rho_m v^2}{2} + \frac{B^2}{2} + \frac{P}{\Gamma - 1} \right) dV = const, \tag{2.16}$$

where $\int_p dV$ denotes the volume integral in the plasma region. Here the first term,

$$T = \int_p \left(\frac{\rho_m v^2}{2} \right) dV, \tag{2.17}$$

represents the kinetic energy and the second and third terms,

$$W_p = \int_p \left(\frac{B^2}{2} + \frac{P}{\Gamma - 1} \right) dV, \tag{2.18}$$

is called the potential energy.

Here it is assumed that the magnetic field generates a set of nested flux surfaces and magnetic field lines are ergodic on almost all flux surfaces. Then the toroidal flux Φ can be introduced in order to express the flux surfaces explicitly, and W_p becomes a functional of P, $\mathbf{B}$, and Φ. The constraints for the functions necessary to obtain a non-trivial solution by the variation of W_p are as follows.

(a) Φ is a single valued function with $\min \Phi = 0$ and $\max \Phi = F$ at the wall,

(b) $\nabla \cdot \mathbf{B} = 0$,

(c) $\mathbf{B} \cdot \nabla \Phi = 0$,

(d) $\int_{\Phi \leq f} \mathbf{B} \cdot \nabla \zeta dV = f$,

(e) $\int_{\Phi \leq f} \mathbf{B} \cdot \nabla \theta dV = \Psi(f)$,

(f) $\int_{\Phi \leq f} P^{1/\Gamma} dV = M(f)$,

where θ and ζ are poloidal and toroidal angles, respectively. For a given constant F, $\Psi(f)$ and $M(f)$ are functions in $0 \leq f \leq F$. These functions correspond to the poloidal flux and the mass of plasma, respectively. Here we prove that under the constraints (a) $\sim$ (f) W_p becomes stationary if and only if P, $\mathbf{B}$, and Φ satisfy the variational conditions

$$P = P(\Phi) \tag{2.19}$$

$$\nabla P = (\nabla \times \mathbf{B}) \times \mathbf{B}. \tag{2.20}$$

Here we give the expression of $\mathbf{B}$ to satisfy the constraints. For a function Φ satisfying (a), the most general form satisfying the constraints (b) and (c) is the Clebsch representation,

$$\mathbf{B} = \nabla \Phi \times \nabla \nu(\Phi, \theta, \zeta). \tag{2.21}$$

Although ν can be a multi-valued function, $\mathbf{B}$ should be single-valued. In order to satisfy (d) and (e), ν must be written by

$$\nu = -\theta + \iota(f)\zeta + \lambda(\Phi, \theta, \zeta), \tag{2.22}$$

where $\iota(f)$ is the rotational transform and defined by

$$\iota \equiv \frac{d\Psi}{d\Phi}, \tag{2.23}$$

and λ is single-valued and periodic in θ and ζ directions. Then we consider the variation of W_p with respect to P, λ and Φ.

First, the variation with respect to only P leads to

$$\delta W_p = \frac{1}{\Gamma - 1} \int_0^F df \int_{\Phi=f} \frac{dS}{|\nabla\Phi|} \delta P. \tag{2.24}$$

Here we use the relation $dV = dSdf/|\nabla\Phi|$ because $|df|/|\nabla\Phi|$ is the distance between the two neighboring magnetic surfaces from (d). From the constraint (f), any perturbation δP must satisfy

$$\frac{1}{\Gamma} \int_{\Phi=f} \frac{dS}{|\nabla\Phi|} P^{\frac{1}{\Gamma}-1} \delta P = 0. \tag{2.25}$$

Therefore we can choose for δP with the delta-function,

$$\delta P = |\nabla\Phi| P^{1-\frac{1}{\Gamma}} (\delta(\mathbf{x}_1) - \delta(\mathbf{x}_2)), \tag{2.26}$$

where $\mathbf{x}_1$ and $\mathbf{x}_2$ denote the different points on the same magnetic surface. Substituting (2.26) into (2.24), we have $P = P(f)$ and the form,

$$P(f) = \left[M'(f) \Big/ \int_{\Phi=f} \frac{dS}{|\nabla\Phi|} \right]^{\Gamma}, \tag{2.27}$$

is given from (f), where the prime denotes the derivative with respect to the argument.

Next, we consider the variation with respect to only λ. The variation δW_p is given by

$$\delta W_p = \int \mathbf{B} \cdot \delta\mathbf{B} dV = -\int \nabla \cdot (\mathbf{B} \times \nabla\Phi) \delta\lambda dV. \tag{2.28}$$

Here we have used (b), and we obtain the condition,

$$\nabla \times \mathbf{B} \cdot \nabla\Phi = 0. \tag{2.29}$$

Finally, in the variation with respect to only Φ, we must consider both kinds of variation for $P(\Phi)$ with the change of Φ and without it. In the former case, the variation with respect to Φ is written by

$$\delta P(\Phi) = P' \delta \Phi. \tag{2.30}$$

In the latter case, we have

$$\begin{aligned} \delta P(\Phi) &= [M'(f)]^{\Gamma} \delta \left[\int_{\Phi=f} \frac{dS}{|\nabla \Phi|} \right]^{-\Gamma} \\ &= \frac{\Gamma P(f)}{\int_{\Phi=f} \frac{dS}{|\nabla \Phi|}} \frac{d}{df} \int_{\Phi=f} dS \frac{\delta \Phi}{|\nabla \Phi|}. \end{aligned} \tag{2.31}$$

Then the variation of W_p with respect to Φ is given by

$$\begin{aligned} \delta W_p &= \int \left[\mathbf{B} \cdot \left\{ \nabla \delta \Phi \times \nabla \nu + \nabla \Phi \times \nabla \left(\frac{\partial \nu}{\partial \Phi} \delta \Phi \right) \right\} \right. \\ &\quad \left. + \frac{P'}{\Gamma - 1} \delta \Phi + \frac{\Gamma P}{\Gamma - 1} \frac{d}{df} \int_{\Phi=f} \frac{\delta \Phi}{|\nabla \Phi|} dS \Big/ \int_{\Phi=f} \frac{dS}{|\nabla \Phi|} \right] dV \\ &= \int \delta \Phi \left[\nabla \cdot (\mathbf{B} \times \nabla \nu) - P' \right] dV. \end{aligned} \tag{2.32}$$

Here we have used the partial integration with respect to f and the fact that $\delta \Phi$ vanishes at the magnetic axis and the wall. Then the condition,

$$\nabla \times \mathbf{B} \cdot \nabla \nu = P', \tag{2.33}$$

is obtained. Making the cross products of eq.(2.21) with $\nabla \times \mathbf{B}$ and using eqs.(2.29) and (2.33), we obtain

$$(\nabla \times \mathbf{B}) \times \mathbf{B} = P' \nabla \Phi = \nabla P. \tag{2.34}$$

By reversing these procedures W_p can be constructed, therefore, the proof has been finished.

It is noted that the constraint (e) means that the poloidal flux is conserved as a function of the toroidal flux in the variation of W_p. The equilibrium under the constraint (e) is called FCT (flux conserving torus) equilibrium. In this case, the profile of the rotational transform is fixed. On the other hand, we can also eliminate this constraint. Then we must consider the variation with respect to $\iota(f)$, and δW_p is given by

$$\begin{aligned} \delta W_p &= \int \mathbf{B} \cdot \delta \mathbf{B} dV \\ &= \int_0^F df \delta\iota(f) \int_{\Phi=f} \mathbf{B} \cdot (\nabla\Phi \times \nabla\zeta) \frac{dS}{|\nabla\Phi|}. \end{aligned} \tag{2.35}$$

We obtain an additional condition,

$$\int_{\Phi=f} \mathbf{B} \cdot (\nabla\Phi \times \nabla\zeta) \frac{dS}{|\nabla\Phi|} = 0, \tag{2.36}$$

which is reduced to

$$I_t \equiv \int \mathbf{J} \cdot \nabla\zeta dV = 0. \tag{2.37}$$

This equation means that the rotational transform $\iota(f)$ or the poloidal flux $\Psi(f)$ is adjusted so that the toroidal net current I_t vanishes. This condition is called the currentless constraint. Therefore we can obtain the two types of equilibrium according to whether the constraint (e) is used or not in this variational method.

The above proof guarantees that we can obtain the static MHD equilibrium by minimizing the potential energy W_p under the several constraints instead of solving eqs.(2.9)$\sim$(2.11) directly. This is called the variational principle for MHD equilibrium.

2.3 Extension of the variational principle for MHD equilibrium to the free boundary problem

In this section we assume that the plasma is isolated from the conducting wall with a vacuum region. The MHD equilibrium in such a situation is called a free boundary MHD equilibrium. In this case, the magnetic field $\mathbf{B}_v$ in the vacuum region satisfies the equations

$$\nabla \cdot \mathbf{B}_v = 0 \tag{2.38}$$

$$\nabla \times \mathbf{B}_v = 0. \tag{2.39}$$

And the pressure balance equation at the plasma-vacuum interface given by

$$P + \frac{B^2}{2} = \frac{B_v^2}{2} \tag{2.40}$$

must be also satisfied. The equilibrium equations (2.9)$\sim$(2.11) for the plasma region are the same as in the fixed boundary case. Even for the free boundary MHD equilibrium we can formulate the variational method based on the potential energy functional for the MHD equilibrium equivalent to that given by equations (2.9)$\sim$(2.11) and (2.38)$\sim$(2.40).

Since the plasma boundary moves freely, it is convenient to use the virtual displacement of plasma, $\boldsymbol{\xi}$, in the variational approach. When an arbitrary functional Z is defined by

$$Z = \int z(\mathbf{x}) dV, \tag{2.41}$$

the variation under the free boundary condition is given by[3]

$$\delta Z = \int \delta z dV + \int_s z\boldsymbol{\xi} \cdot \mathbf{n} dS, \tag{2.42}$$

where $\mathbf{n}$ is the outward normal unit vector on the boundary S and the second term represents the contribution from the movement of the boundary.

In the plasma region the potential energy functional is the same as eq.(2.18) in the fixed boundary case. We reconsider the variation of W_p by expressing all perturbations in terms of $\boldsymbol{\xi}$ and associated equilibrium quantities. The magnetic perturbation $\delta\mathbf{B}$ is expressed by

$$\delta\mathbf{B} = \nabla \times (\boldsymbol{\xi} \times \mathbf{B}). \tag{2.43}$$

which is obtained from Faraday's law (2.5) and Ohm's law (2.4) by using $\mathbf{v} = \partial\boldsymbol{\xi}/\partial t$. The adiabatic equation (2.3) gives the expression of pressure perturbation

$$\delta P = -\boldsymbol{\xi} \cdot \nabla P - \Gamma P \nabla \cdot \boldsymbol{\xi}. \tag{2.44}$$

Then, the variation of the functional W_p under the free boundary condition is written by

$$\begin{aligned} \delta W_p &= \int_p \left[\mathbf{B} \cdot \nabla \times (\boldsymbol{\xi} \times \mathbf{B})) - \frac{1}{\Gamma - 1}(\boldsymbol{\xi} \cdot \nabla P + \Gamma P \nabla \cdot \boldsymbol{\xi})\right] dV \\ &\quad + \int_s \left(\frac{B^2}{2} + \frac{P}{\Gamma - 1}\right) \boldsymbol{\xi} \cdot \mathbf{n} dS \\ &= \int_p (\nabla P - \mathbf{J} \times \mathbf{B}) \cdot \boldsymbol{\xi} dV - \int_s \left(\frac{B^2}{2} + P\right) \boldsymbol{\xi} \cdot \mathbf{n} dS. \end{aligned} \tag{2.45}$$

Here we have used the boundary condition

$$\mathbf{B} \cdot \mathbf{n} = 0 \tag{2.46}$$

on the plasma surface that is given by the assumption that the plasma is a perfect conductor. The first term of the last expression in eq.(2.45) for δW_p gives MHD equilibrium equation (2.9). The second term represents the total force on the free boundary.

In the vacuum region, the potential energy W_v is defined as

$$W_v = \int_v \frac{B_v^2}{2} dV, \tag{2.47}$$

and the variation under the free boundary condition is written by

$$\delta W_v = \int_v \mathbf{B}_v \cdot \delta \mathbf{B}_v dV - \int_s \frac{B_v^2}{2} \boldsymbol{\xi} \cdot \mathbf{n} dS. \tag{2.48}$$

Here the minus sign appears in the second term means that $\mathbf{n}$ is chosen as an inwardly directed normal vector to the vacuum region. We need a constraint in the variation of δW_v. It is noted that eqs.(2.38) and (2.39) are complementary each other. In other words, if we consider one of them as the constraint, the other expression is obtained as a result of the variational calculation.

First, we choose eq.(2.38) as the constraint. The vacuum magnetic field that satisfied this constraint is expressed by

$$\mathbf{B}_v = \nabla \times \mathbf{A}_v, \tag{2.49}$$

where $\mathbf{A}_v$ denotes the vector potential in the vacuum region. Since eq.(2.38) is considered as the differential form of conservation of magnetic flux, and $\mathbf{B}_v$ is the related to the vacuum electric field $\mathbf{E}_v$ as

$$\mathbf{E}_v + \mathbf{v} \times \mathbf{B}_v = 0, \tag{2.50}$$

on the plasma surface[38]. If we choose the Coulomb gauge

$$\phi_E = 0 \text{ and } \nabla \cdot \mathbf{A}_v = 0 \tag{2.51}$$

for the electric potential ϕ_E and the vector potential $\mathbf{A}_v$, we obtain

$$\mathbf{E}_v = -\frac{\partial \mathbf{A}_v}{\partial t}. \tag{2.52}$$

Substituting eq.(2.52) into eq.(2.50), we obtain

$$\delta \mathbf{A}_v = \boldsymbol{\xi} \times \mathbf{B}_v. \tag{2.53}$$

Then, the variation δW_v under the constraint of eq.(2.38) is given by

$$\begin{aligned} \delta W_v &= \int_v \mathbf{B}_v \cdot \nabla \times \delta \mathbf{A}_v dV - \int \frac{B_v^2}{2} \boldsymbol{\xi} \cdot \mathbf{n} dS \\ &= \int \delta \mathbf{A}_v \cdot \nabla^2 \mathbf{A}_v dV + \int \frac{B_v^2}{2} \boldsymbol{\xi} \cdot \mathbf{n} dS, \end{aligned} \tag{2.54}$$

where we have used the boundary condition

$$\mathbf{B}_v \cdot \mathbf{n} = 0, \tag{2.55}$$

on the plasma-vacuum interface. The first term of eq.(2.54) gives the variational equation

$$\nabla^2 \mathbf{A}_v = 0, \tag{2.56}$$

which is equivalent to eq.(2.39) in the vacuum region under the constraint of (2.51). Here if we define the total functional W as

$$W = W_p + W_v, \tag{2.57}$$

we find from eqs.(2.45) and (2.54),

$$\begin{aligned}\delta W &= \int_p (\nabla P - \mathbf{J} \times \mathbf{B}) \cdot \boldsymbol{\xi} dV + \int_v \delta \mathbf{A}_v \cdot \nabla^2 \mathbf{A}_v dV \\ &\quad + \int_s \left[B_v^2 - \left(\frac{B^2}{2} + p \right) \right] \boldsymbol{\xi} \cdot \mathbf{n} dS. \end{aligned} \tag{2.58}$$

Then the pressure balance equation (2.40) at the plasma surface is also obtained as a variational condition in addition to eqs.(2.9) and (2.56).

Next, we consider eq.(2.39) as the constraint. $\mathbf{B}_v$ satisfying this constraint can be written by

$$\mathbf{B}_v = \nabla \phi, \tag{2.59}$$

with a magnetic potential ϕ. It is noted that eq.(2.39) implies that there is no current in the vacuum region and both the plasma current and the external current are expressed in terms of ϕ. The vacuum is not a simply connected region mathematically since it encircles both the plasma region and the external coils. The net toroidal plasma current I_t is given by

$$I_t = \oint_{l_1} \mathbf{B}_v \cdot dl, \tag{2.60}$$

where the path of integral l_1 is an arbitrary circuit that encircles only the plasma column once. From eq.(2.59) we obtain

$$I_t = \oint_{l_1} \nabla \phi \cdot dl = \oint_{l_1} d\phi. \tag{2.61}$$

Similarly, the total external coil currents I_{ext} is given by

$$I_{ext} = \oint_{l_2} d\phi, \tag{2.62}$$

where l_2 is the circuit that encircles only the external coils once. If any current would flow in the plasma or vacuum region, I_t and I_{ext} change automatically.

Then, the constraint (2.39) implies that I_t and I_{ext} are fixed during the variation of W_v. In this case, the variation of eq.(2.48) is written by

$$\begin{aligned}\delta W_v &= \int_v \nabla\phi\cdot\delta\nabla\phi dV - \int_s \frac{B_v^2}{2}\boldsymbol{\xi}\cdot\mathbf{n}dS \\ &= -\int_s \delta\phi\nabla\phi\cdot\mathbf{n}dS - \int_v \delta\phi\nabla^2\phi dV - \int \frac{B_v^2}{2}\boldsymbol{\xi}\cdot\mathbf{n}dS. \qquad (2.63)\end{aligned}$$

In the evaluation of the first term we must remember that the potential ϕ is not single-valued. We introduce two cuts at $\theta = const.$ and $\zeta = const.$ in the plasma region and name the both sides S_1 and S_1' at the $\theta = const.$ cut and S_2 and S_2' at the $\zeta = const.$ cut. Because $\nabla\phi\cdot\mathbf{n} = 0$ at both the plasma boundary and the outer conducting wall, the surface integral is decomposed as

$$\begin{aligned}\int \delta\phi\nabla\phi\cdot\mathbf{n}dS &= \int_{S_1}\delta\phi\nabla\phi\cdot\mathbf{n}dS + \int_{S_1'}\delta\phi\nabla\phi\cdot\mathbf{n}dS \\ &\quad + \int_{S_2}\delta\phi\nabla\phi\cdot\mathbf{n}dS + \int_{S_2'}\delta\phi\nabla\phi\cdot\mathbf{n}dS. \qquad (2.64)\end{aligned}$$

Since $\nabla\phi$ must be single valued and take the same value at the both sides of the cut, we obtain

$$\int \delta\phi\nabla\phi\cdot\mathbf{n}dS = \int_{S_1}\delta(\phi-\phi^\dagger)\nabla\phi\cdot\mathbf{n}dS + \int_{S_2}\delta(\phi-\phi^\dagger)\nabla\phi\cdot\mathbf{n}dS, \qquad (2.65)$$

where $\phi^\dagger$ is the value at S_1' and S_2' of the cuts. From eqs.(2.61) and (2.62), $\delta(\phi-\phi^\dagger)$ corresponds to the perturbation of the current. Therefore, this term must vanish for the constraint that the current is conserved in the plasma column. We can apply the same discussion to the external coil current. Thus, we have

$$\delta W_v = -\int_v \delta\phi\nabla^2\phi dV - \int \frac{B_v^2}{2}\boldsymbol{\xi}\cdot\mathbf{n}dS. \qquad (2.66)$$

Here the first term gives the variational condition

$$\nabla^2\phi = 0, \tag{2.67}$$

which corresponds to eq.(2.38). In this case, if we define the total energy functional W as

$$W = W_p - W_v, \tag{2.68}$$

which is different from (2.57), we have the energy variation δW,

$$\delta W = \int_p (\nabla P - \mathbf{J}\times\mathbf{B})\cdot\boldsymbol{\xi} dV - \int_v \delta\phi\nabla^2\phi dV + \int_s \left[\frac{B_v^2}{2} - \left(\frac{B^2}{2} + P\right)\right] dS. \tag{2.69}$$

Again we obtain the pressure balance equation (2.40) at the plasma-vacuum interface, eq.(2.9) and eq.(2.67) from $\delta W = 0$. Thus the stationary state of the total energy functional corresponds to an MHD equilibrium under the constant current condition.

It is noted that the sign of W_v in the expression of the total energy functional depends on the constraint which is conserved, the flux or the current.

2.4 Derivation of the variational equations

In the three-dimensional analysis, it is crucial to choose the coordinate system that makes the numerical calculation sufficiently accurate. When the existence of the nested magnetic surfaces is assumed, it is the most convenient to employ the flux coordinates.

In the BETA code to study MHD equilibrium, stability and transport of stellarator[8,9], the coordinates (s, u, v) are used where $s = \Phi/F$ is the normalized toroidal flux in the plasma region. u and v are the normalized poloidal and toroidal angles, defined as

$$u \equiv \frac{\theta}{2\pi}, \quad v \equiv \frac{Q\zeta}{2\pi}, \tag{2.70}$$

where Q denotes the number of field period in a stellarator configuration. Then, the MHD equilibrium of toroidal plasma is considered in the cubic domain,

$$0 \leq s \leq 1, \quad 0 \leq u \leq 1, \quad 0 \leq v \leq 1. \tag{2.71}$$

Here $s = 0$ and $s = 1$ correspond to the magnetic axis and the outermost magnetic surface of the plasma, respectively.

We introduce the cylindrical coordinates (r, ζ, z) to explain geometrical properties of the coordinates (s, u, v). There are relations between the Cartesian coordinates (x_1, x_2, x_3) and (r, ζ, z),

$$\begin{cases} x_1 = (A + r)\cos\zeta \\ x_2 = (A + r)\sin\zeta \\ x_3 = z, \end{cases} \tag{2.72}$$

where length is normalized by the minor radius of the conducting wall and A denotes the aspect ratio of the toroidal vacuum chamber. We define the expression for each flux surfaces as follows. For $s = 0$, the position of the magnetic axis is described by

$$\begin{cases} r = r_0(v) \\ z = z_0(v) \end{cases} \tag{2.73}$$

and for $s = 1$, the shape of the plasma surface is represented by

$$\begin{cases} r = r_1(u, v) \\ z = z_1(u, v). \end{cases} \tag{2.74}$$

Here we introduce the radial function $\hat{R}(s, u, v)$ for the range of $0 \leq \hat{R} \leq 1$. The flux surface defined by $s = const.$ in $0 < s < 1$ is expressed in the (r, z) plane by

$$\begin{cases} r = r_0(v) + \hat{R}(s, u, v)[r_1(u, v) - r_0(v)] \\ z = z_0(v) + \hat{R}(s, u, v)[z_1(u, v) - z_0(v)], \end{cases} \tag{2.75}$$

with the condition

$$\hat{R}(0, u, v) = 0, \quad \hat{R}(1, u, v) = 1. \tag{2.76}$$

Then the Jacobian of the flux coordinates in the plasma region is given by

$$D_p = L H_p K \hat{R} \hat{R}_s, \tag{2.77}$$

where the subscripts s, u and v mean the partial derivative with respect to the assigned coordinate and

$$L = 2\pi A \tag{2.78}$$

$$K = 1 + r/A \tag{2.79}$$

$$H_p = (z_1 - z_0)\frac{\partial r_1}{\partial u} - (r_1 - r_0)\frac{\partial z_1}{\partial u}. \tag{2.80}$$

When we treat free boundary MHD equilibria, we use the similar coordinates (s, u, v) in the vacuum region and $s = const.$ surface is given in (r, z) plane of the cylindrical coordinates as

$$\begin{cases} r = r_1(u,v) + s[r_2(u,v) - r_1(u,v)] \\ z = z_1(u,v) + s[z_2(u,v) - z_1(u,v)] \end{cases} \tag{2.81}$$

with $0 \leq s \leq 1$. Here

$$\begin{cases} r = r_2(u,v) \\ z = z_2(u,v) \end{cases} \tag{2.82}$$

represents the shape of the outer conducting wall. In (2.81) case $r = r_1$ and $z = z_1$ represent the free boundary which is expressed as

$$\begin{cases} r_1 = r_3(v) + g(u,v)[r_2(u,v) - r_3(v)] \\ z_1 = z_3(v) + g(u,v)[z_2(u,v) - z_3(v)], \end{cases} \tag{2.83}$$

with the shaping function $g(u, v)$. Here $r_3(v)$ and $z_3(v)$ describe a curve corresponding to the center of the free boundary. The Jacobian D_v in the vacuum region is also given by

$$D_v = LH_vK, \tag{2.84}$$

where

$$H_v = (z_2 - z_1)\left\{ s\frac{\partial r_2}{\partial u} + (1-s)\frac{\partial r_1}{\partial u} \right\} - (r_2 - r_1)\left\{ s\frac{\partial z_2}{\partial u} + (1-s)\frac{\partial z_1}{\partial u} \right\}. \tag{2.85}$$

Now we consider the variation of the potential energy in this flux coordinates by applying the results in Sec.2.2 and 2.3. We can write the magnetic field $\mathbf{B}$ as

$$\mathbf{B} = \nabla s \times \nabla \nu \tag{2.86}$$

$$\nu = -u + \frac{\iota}{Q}v + \lambda(s,u,v). \tag{2.87}$$

Then, the Cartesian component B_j can be written in the form

$$B_j = \frac{\partial(s, \nu, x_j)}{\partial(x_1, x_2, x_3)} = \frac{D_j}{D_p}, \tag{2.88}$$

where

$$D_j = \frac{\partial(s, \nu, x_j)}{\partial(s, u, v)}. \tag{2.89}$$

Here we use the variational result $P = P(s)$ for the potential energy functional because this does not affect other variations. In the flux coordinates eq.(2.27) can be written by

$$P(s) = [M'(s) \Big/ \int\int D_p du dv]^\Gamma \tag{2.90}$$

with the mass function $M(s)$. Thus, the expression for the potential energy functional W_p in the plasma region is written as

$$\begin{aligned} W_p &= \int\int\int \left[\frac{D_1^2 + D_2^2 + D_3^2}{2D_p} + \frac{P(s)D_p}{\Gamma - 1}\right] ds du dv \\ &= \int\int\int \frac{(\nu_u r_v - \nu_v r_u)^2 + L^2 K^2 \nu_u^2 + (\nu_u z_v - \nu_v z_u)^2}{2D_P} ds du dv \\ &\quad + \frac{1}{\Gamma - 1} \int \frac{[M'(s)]^\Gamma}{[\int\int D_p du dv]^{\Gamma - 1}} ds. \end{aligned} \tag{2.91}$$

We impose the fixed boundary condition on (2.91). Then W_p becomes a functional of the unknown functions $\hat{R}, \nu, r_0$ and z_0, since r_1 and z_1 are determined by the shape of the conducting wall. The variation with respect to $\hat{R}$ corresponds to that with respect to Φ in Sec.2.2. The perturbation $\delta\nu$ is considered to be equivalent to $\delta\lambda$. Though the magnetic axis belongs to singularity, the position of the magnetic axis is determined as a result of the variational principle. Therefore, we also need the variation with respect to

r_0 and z_0. Then the variation of W_p is expressed by

$$\begin{aligned}\delta W_p &= -\int\int\int \left[L_1(\nu)\delta\nu + L_2(\hat{R})\delta\hat{R}\right] dsdudv \\ &\quad -\int [L_3(r_0)\delta r_0 + L_4(z_0)\delta z_0]dv. \end{aligned} \tag{2.92}$$

The operators $L_1(\nu)$, $L_2(\hat{R})$, $L_3(r_0)$ and $L_4(z_0)$ are obtained with the following expressions

$$\begin{aligned} L_1(\nu) &= \frac{\partial}{\partial u}\frac{[r_v^2 + L^2K^2 + z_v^2]\nu_u - [r_u r_v + z_u z_v]\nu_v}{D_p} \\ &\quad + \frac{\partial}{\partial v}\frac{[r_u^2 + z_u^2]\nu_v - [r_u r_v + z_u z_v]\nu_u}{D_p} \end{aligned} \tag{2.93}$$

$$\begin{aligned} L_2(\hat{R}) &= (r_1 - r_0)\left\{\frac{\partial}{\partial u}\frac{\nu_v(\nu_v r_u - \nu_u r_v)}{D_p}\right. \\ &\quad \left. + \frac{\partial}{\partial v}\frac{\nu_u(\nu_u r_v - \nu_v r_u)}{D_p} + 2\pi\left(\frac{D_p P^*}{LK} - \frac{LK\nu_u^2}{D_p}\right)\right\} \\ &\quad + (z_1 - z_0)\left\{\frac{\partial}{\partial u}\frac{\nu_v(\nu_v z_u - \nu_u z_v)}{D_p}\right. \\ &\quad \left. + \frac{\partial}{\partial v}\frac{\nu_u(\nu_u z_v - \nu_v z_u)}{D_p}\right\} - LH_p\hat{R}\frac{\partial}{\partial s}(P^*K) \end{aligned} \tag{2.94}$$

$$\begin{aligned} L_3(r_0) &= \int\int\left[(1-\hat{R})\left\{\frac{\partial}{\partial u}\frac{\nu_v(\nu_v r_u - \nu_u r_v)}{D_p} + \frac{\partial}{\partial v}\frac{\nu_u(\nu_u r_v - \nu_v r_u)}{D_p}\right.\right. \\ &\quad \left.\left. + 2\pi\left(\frac{D_p P^*}{LK} - \frac{LK\nu_u^2}{D_p}\right)\right\} - P^* LK\hat{R}\hat{R}_s\frac{\partial z_1}{\partial u}\right] dsdu \end{aligned} \tag{2.95}$$

$$\begin{aligned} L_4(z_0) &= \int\int\left[(1-\hat{R})\left\{\frac{\partial}{\partial u}\frac{\nu_v(\nu_v z_u - \nu_u z_v)}{D_p} + \frac{\partial}{\partial v}\frac{\nu_u(\nu_u z_v - \nu_v z_u)}{D_p}\right\}\right. \\ &\quad \left. + P^* LK\hat{R}\hat{R}_s\frac{\partial z_1}{\partial u}\right] dsdu, \end{aligned} \tag{2.96}$$

where

$$P^* = \frac{B^2}{2} + P. \tag{2.97}$$

The Euler equations $L_1(\nu) = 0$ and $L_2(\hat{R}) = 0$ can be written as

$$\mathbf{J} \cdot \nabla s = 0 \tag{2.98}$$

$$\mathbf{J} \cdot \nabla \nu = P'(s), \tag{2.99}$$

respectively. They are equivalent to eqs.(2.29) and (2.33). Under the FCT equilibrium, where the rotational transform profile $\iota(s)$ is fixed at the zero pressure condition, above four Euler equations are sufficient to obtain an MHD equilibrium solution. On the other hand, for the currentless equilibrium of stellarator, we need an additional equation to determine the rotational transform. From the discussion in Sec.2.2, the variation with respect to ι is given by

$$\delta W_p = \int I_t \ \delta\iota \ dV, \tag{2.100}$$

and the corresponding Euler equation is $I_t = 0$.

In the free boundary MHD equilibrium case, the constraint that conserves the current in the external coils is implemented in the BETA code. As discussed in Sec.2.3, the total potential energy functional W is given by eq.(2.68) with

$$W_v = \frac{1}{2} \int_v |\nabla \phi|^2 dV. \tag{2.101}$$

When we use the coordinates (s, u, v) in the vacuum region, this Dirichlet integral is rewritten as

$$W_v = \frac{1}{2} \int \int \int (a\phi_s^2 + b\phi_u^2 + c\phi_v^2 + 2d\phi_s\phi_u + 2e\phi_s\phi_v + 2f\phi_u\phi_v) ds du dv, \tag{2.102}$$

where

$$a = \frac{LK(r_u^2 + z_u^2 + e^2)}{H_v} \tag{2.103}$$

$$b = \frac{LK(r_s^2 + z_s^2 + f^2)}{H_v} \tag{2.104}$$

$$c = \frac{H_v}{LK} \tag{2.105}$$

$$d = \frac{LK(ef - r_u r_s - z_u z_s)}{H_v} \tag{2.106}$$

$$e = \frac{r_u z_v - r_v z_u}{LK} \tag{2.107}$$

$$f = \frac{r_v z_s - r_s z_v}{LK}. \tag{2.108}$$

Thus we need the variations of ϕ and g in eq.(2.83) in addition to ν, $\hat{R}$, r_0 and z_0 in the plasma region. The Euler equation to minimize W_v with respect to ϕ is Laplace's equation with the expression

$$\frac{\partial}{\partial s}(a\phi_s + d\phi_u + e\phi_v) + \frac{\partial}{\partial u}(b\phi_u + d\phi_s + f\phi_v) + \frac{\partial}{\partial v}(c\phi_v + e\phi_s + f\phi_u) = 0. \tag{2.109}$$

In general, the solution of Laplace's equation makes the Dirichlet integral (2.102) minimum. In the free boundary case, therefore, the variational problem of eq.(2.68) becomes the minimax problem. In the BETA code eq.(2.109) is solved by using the successive over relaxation method (SOR) with relaxation parameter independently of the energy minimization. The boundary conditions at $s = 0$ and $s = 1$ to solve eq.(2.109) are given by

$$a\phi_s + d\phi_u + e\phi_v = 0, \tag{2.110}$$

which means $\mathbf{B}_v \cdot \mathbf{n} = 0$. The periodicity condition imposed in the u and v directions are expressed by

$$\phi(s, u+1, v) = \phi(s, u, v) + C_1 \tag{2.111}$$

$$\phi(s, u, v+1) = \phi(s, u, v) + C_2. \tag{2.112}$$

Here C_1 and C_2 correspond to the net toroidal current and the total external current in the coils as discussed in Sec.2.3, respectively. In the case that the currents are conserved, C_1 and C_2 are assigned as the external conditions.

When $g(u,v)$ is varied, the variation of the total functional W is given by

$$\delta W = -\int\int M(g)\delta g du dv, \tag{2.113}$$

where the operator $M(g)$ is written in the form

$$M(g) = LK[(r_2 - r_3)z_u - (z_2 - z_3)r_u]\left[\frac{B^2}{2} + P - \frac{B_v^2}{2}\right]. \tag{2.114}$$

The Euler equation $M(g) = 0$ corresponds to the pressure balance equation at the plasma-vacuum interface and determines the free boundary.

2.5 Steepest descent method for energy minimization

As discussed in Sec.2.2, the minimum energy state obtained under several constraints corresponds to an MHD equilibrium. In the numerical code the minimum energy state can be found by using an iteration method.

We introduce an artificial time parameter, t, and describe the variations at each iteration in terms of the time derivative. Since the vacuum potential ϕ is solved by applying the successive over relaxation method to Laplace's equation, the variational equation for W is written by

$$\begin{aligned}\frac{dW}{dt} &= -\int \left(L_1(\nu)\frac{\partial \nu}{\partial t} + L_2(\hat{R})\frac{\partial \hat{R}}{\partial t} \right) dV \\ &\quad -\int \left(L_3(r_0)\frac{\partial r_0}{\partial t} + L_4(z_0)\frac{\partial z_0}{\partial t} \right) dv - \int M\frac{\partial g}{\partial t} du dv.\end{aligned} \tag{2.115}$$

For simplicity we use the vector $\mathbf{U}$ of which components are the functions $(\nu, \hat{R}, r_0, z_0)$. Here we choose the descent path in the space $(\mathbf{U}, g)$ for efficient energy minimization that is described by

$$e_j \frac{\partial \mathbf{U}_j}{\partial t} = L_j \quad \text{for} \quad j = 1 \sim 4 \tag{2.116}$$

$$e_5 \frac{\partial g}{\partial t} = M \tag{2.117}$$

with positive coefficients e_j. By using (2.116) and (2.117) dW/dt is shown as

$$\frac{dW}{dt} = -\int \left[e_1 \left(\frac{\partial \nu}{\partial t} \right)^2 + e_2 \left(\frac{\partial \hat{R}}{\partial t} \right)^2 \right] dV$$

$$-\int \left[e_3 \left(\frac{\partial r_0}{\partial t} \right)^2 + e_4 \left(\frac{\partial z_0}{\partial t} \right)^2 \right] dv - \int e_5 \left(\frac{\partial g}{\partial t} \right)^2 dudv. \tag{2.118}$$

It is seen that RHS is always negative or zero. Therefore, the solutions for the differential equations (2.116) and (2.117) can decrease the energy W monotonically toward the minimum energy state.

In the BETA code the finite difference method is employed for the spatial derivatives in the three directions. It should be noted that operators L_j include the second order derivatives with respect to u and v. This brings about the stability problem in the numerical scheme. An estimation for the numerical stability condition gives a limit for the maximum time step Δt which scales like h_u^2 or h_v^2, where h_u and h_v are the mesh size in the u and v directions, respectively. In order to take a larger time step than the above one, we add the terms of the second order time derivative to the path equations (2.116) in the following way,

$$a_j \frac{\partial^2 \mathbf{U}_j}{\partial t^2} + e_j \frac{\partial \mathbf{U}_j}{\partial t} = L_j, \quad (j = 1 \sim 4) \tag{2.119}$$

This is one of the steepest descent method and called the second order Richardson method. If we choose a_j such that the time-dependent differential equations become hyperbolic and the Courant-Friedrichs-Lewy stability condition is satisfied, we can take Δt that scales like h_u or h_v for the maximum value.

In the equation of (2.119), the coefficient e_j must be selected to guarantee that the path is the steepest descent. For simplicity, we assume that the functional W is varied by only one function U with the corresponding oper-

ator L. We also assume that L has a negative eigenvalue $-\omega^2$ corresponding to an eigenfunction Λ, and U approaches Λ as $e^{\lambda t}\Lambda$ in the iteration scheme. Then, eq.(2.119) gives the relation

$$a\lambda^2 + e\lambda = -\omega^2, \tag{2.120}$$

and the time derivative of the energy W is written as

$$\frac{\partial W}{\partial t} = -\int (a\lambda + e)\left(\frac{\partial U}{\partial t}\right)^2 dV. \tag{2.121}$$

In order to maintain the monotonic decrease of W, the coefficient must satisfy the condition

$$\frac{e}{a} > |\lambda|. \tag{2.122}$$

This equation (2.122) implies that e/a must be larger than the largest eigenvalue of λ. However, if we choose a large fixed number for e/a, λ is scaled by

$$\lambda \approx -\frac{\omega^2}{e} \tag{2.123}$$

from eq.(2.120). This means that the convergence becomes very slow when ω is small. Equation (2.123) indicates that we can accelerate this scheme if we choose e to be proportional to the lowest eigenvalue λ and to be time-dependent. Here, we choose $e = \alpha|\lambda|$, where α must be larger than a so as to satisfy eq.(2.122). Then λ scales in proportion to ω as

$$\lambda \approx \omega \cdot \alpha^{-\frac{1}{2}}. \tag{2.124}$$

This procedure requires the quantitative evaluation of λ. In the BETA code the eigenvalue ω is used instead of λ to adjust the coefficient e, because λ is

proportional to ω on the steepest descent path as shown in eq.(2.124). The eigenvalue $-\omega_j^2$ at the time $t = t_j$ is approximately given by

$$-\omega_j^2 = \left(\frac{F_t}{2F} + \frac{e}{a}\right)_t + \left(\frac{F_t}{2F}\right)\left(\frac{F_t}{2F} + \frac{e}{a}\right), \tag{2.125}$$

where

$$F \equiv \int \left(\frac{\partial \mathbf{U}}{\partial t}\right)^2 dV, \tag{2.126}$$

and subscript t denotes the time derivative. In the code, $e(t)/a$ is chosen as an average of $|\omega_j|^2$ over the previous N time steps as

$$\frac{e(t)}{a} = 2\left(\frac{1}{N}\sum_k |\omega_{j-k}|^2\right)^{\frac{1}{2}}. \tag{2.127}$$

The operator M in eq.(2.117) includes only the first order derivatives with respect to the spatial variables. This first order equation (2.117) for the free boundary function g is solved by using the Lax-Wendroff method in the BETA code.

Under the currentless constraint, another numerical scheme to obtain a stationary solution of

$$\frac{\partial \iota}{\partial t} = -I_t \tag{2.128}$$

must be added.

2.6 Nonlinear stability of ideal MHD mode based on the variational principle

The concept of the nonlinear stability in the BETA code is explained here. When the plasma is perturbed from the equilibrium state, there are two possible cases ; increase or decrease of the total potential energy including a contribution due to the perturbation. The former corresponds to the stable equilibrium and the latter to the unstable one for the given perturbation.

In the linear stability theory[12], if we assume the time-dependence of the infinitesimal displacement $\boldsymbol{\xi}$ as $\boldsymbol{\xi} \propto e^{i\omega t}$, the growth rate $-\omega^2$ is given by

$$-\omega^2 = \frac{\delta W}{\frac{1}{2}\int \rho_m |\boldsymbol{\xi}|^2 dV}, \tag{2.129}$$

where δW denotes the linear potential energy and $-\omega^2 > 0$ corresponds to stable state. In this section, we consider an extension of this linear stability formulation to the case of the finite amplitude perturbation. Here we limit the discussion to the fixed boundary case for simplicity.

The nonlinear potential difference is defined as the difference of the potential energy W^0 at the equilibrium state and the potential energy W^1 including both contributions from the equilibrium and the perturbation. It is considered that δW in eq.(2.129) may be replace with $W^1 - W^0$[39].

The vectors $\mathbf{U}^0 = (\nu^0, \hat{R}^0, r_0^0, z_0^0)$ and $\mathbf{U}^1 = (\nu^1, \hat{R}^1, r_0^1, z_0^1)$ are introduced to denote the variational variables that correspond to the equilibrium and perturbed states, respectively. Then the growth rate can be defined as the

Rayleigh quotient

$$-\omega^2 = \frac{W^1 - W^0}{||\delta' \mathbf{U}||^2}. \tag{2.130}$$

Here δ' denotes the difference of the components between $\mathbf{U}^1$ and $\mathbf{U}^0$ and the norm $||\delta' \mathbf{U}||^2$ is given by

$$\begin{aligned} ||\delta' \mathbf{U}||^2 &= \int\int\int [w_1(\delta'\nu)^2 + w_2(\delta'\hat{R})^2] ds du dv \\ &\quad + \int [w_3(\delta' r_0)^2 + w_4(\delta' z_0)^2] dv, \end{aligned} \tag{2.131}$$

where the weight factors w_j are determined so that, in the straight cylindrical plasma limit, the norm is assumed to be expressed by

$$||\delta' \mathbf{U}||^2 = \frac{1}{2} \int \rho_m |\boldsymbol{\xi}_\perp|^2 dV. \tag{2.132}$$

The relation (2.130) gives the growth rate $-\omega^2$ after W^1 and $||\delta' \mathbf{U}||^2$ are obtained numerically. In order to find the perturbed energy W^1 and the associated vector $\mathbf{U}^1$, we try the second minimization based on the same variational method as that to obtain W^0 by imposing an additional constraint. In the BETA code, the first minimization to determine the equilibrium state is restricted to one field period of the torus because stellarator configurations usually have a periodicity condition in the toroidal direction. Since we have interest in the perturbation with a larger wave-length than the length of single field period, W^1 is calculated for the full torus and can be lower than W^0 corresponding to the full torus. The constraint imposed to obtain W^1 is expressed by

$$(\delta' \mathbf{U}, \mathbf{U}^d) = \varepsilon_0, \tag{2.133}$$

where $(\mathbf{a}, \mathbf{b})$ means the scalar product that is related to the norm by $(\mathbf{U}, \mathbf{U}) = ||\mathbf{U}||^2$. Here $\mathbf{U}^d$ is composed of the test functions describing the linear eigen-

functions and ε_0 is a parameter that controls the amplitude of the perturbation. Thus, the second minimization corresponds to find the minimum of the potential energy within the hyperplane defined by (2.133) and W^1 is the minimum energy for the perturbation $\mathbf{U}^d$ with an amplitude of ε_0.

It is convenient to use the Lagrange multiplier method to solve the extremum problem with the constraint. When μ is the multiplier, $\mathbf{U}^1$ and W^1 satisfy the relation

$$\frac{\partial W^1}{\partial \mathbf{U}^1} - \mu \frac{\partial \varphi}{\partial \mathbf{U}^1} = 0, \tag{2.134}$$

where φ represents the constraint (2.133) in the following way

$$\varphi = (\delta' \mathbf{U}, \mathbf{U}^d) - \varepsilon_0. \tag{2.135}$$

Derivatives in the first term of (2.134) are described by using the same operators L_j as in the energy minimization to find the equilibrium. From the definition of the scalar product in φ,

$$\frac{\partial \varphi}{\partial U_j^1} = w_j U_j^d \tag{2.136}$$

are given. Therefore, the minimization problem with the constraint (2.133) reduces to solving the equations

$$L_j(U_j^1) - \mu w_j U_j^d = 0. \tag{2.137}$$

These equations can be solved to obtain $\mathbf{U}^1$ with the same steepest descent method as that applied to the equilibrium problem for obtaining $\mathbf{U}^0$. Then the path of the steepest descent is expressed by the equations

$$a_j \frac{\partial^2 U_j}{\partial t^2} + e_j \frac{\partial U_j}{\partial t} = L_j(U_j) - \mu w_j U_j^d. \tag{2.138}$$

Here the Lagrange multiplier is given by

$$\mu = \frac{(\mathbf{L}(\mathbf{U^1}), \mathbf{U}^d)}{||\mathbf{U}_d||^2}, \tag{2.139}$$

where

$$\mathbf{L}(\mathbf{U}_j) = (L_1(\nu), L_2(\hat{R}), L_3(r_0), L_4(z_0)). \tag{2.140}$$

Chapter 3

Ideal MHD Equilibrium and Stability of Heliotron E and Heliotron H

3.1 Introduction

We apply the BETA code explained in Chapter 2 to investigate the ideal MHD equilibrium and stability of Heliotron E and Heliotron H [40,42]. The BETA code has an advantage that the realistic three dimensional configuration of Heliotron E or Heliotron H is included in the stability analysis of global modes.

Heliotron E is one of the largest experimental device of ℓ=2 heliotron/ torsatron configuration [1]. The number of the field period is 19, the major

radius is 2.2 m and the average minor radius is 0.2 m. In experiments it is expected that plasmas heated gradually by RF waves relax to currentless equilibria. On the other hand, when plasmas are heated abruptly by the neutral beam injection (NBI), for example, FCT equilibria may be achieved. Therefore, to know the difference between the both type equilibria, the stability of both the currentless and FCT equilibria is examined in the Heliotron E configuration.

The Heliotron E device was designed to have a large rotational transform and a strong shear to stabilize instabilities in the vacuum magnetic configuration. However, in the high shear heliotron/torsatron, usually ι=1 surface exists in the plasma column. Soft X ray and density fluctuations with $(m, n) = (1, 1)$ resonant at $\iota = 1$ have been observed in Heliotron E high beta experiments [2]. Thus in this chapter we concentrate in the ideal MHD stability of the Heliotron E plasma against the $m = 1$ and $n = 1$ mode.

Since the $m = 1$ and $n = 1$ instability is considered to be related to the ι=1 surface, it is interesting to examine the stability in a heliotron configuration with ι larger than unity everywhere inside the plasma column. We pick up Heliotron H as one of such configurations. Heliotron H is originally designed as a reactor of the heliotron type with 15 periods [41]. Its major and minor radii are 21 m and 1.7 m. We also try to calculate the $m = 1$ and $n = 1$ instability under the free boundary condition, since the BETA code has capability to study the free boundary problem.

It is known that the stability is controlled by changing the magnetic axis position by the vertical magnetic field. The magnetic axis position is related to magnetic well or hill in the vacuum magnetic configuration. We expect

that, because of the increase of the magnetic hill, the stability deteriorates when the magnetic axis is shifted inward by the vertical magnetic field. On the contrary, when the magnetic axis is shifted outward, the stability is improved by deepening the magnetic well.

In Sec.3.2, we calculate the currentless and FCT equilibria of the Heliotron E plasma under the fixed boundary condition. For these equilibria the ideal nonlinear stability against the $m = 1$ and $n = 1$ mode is investigated. Bauer, Betancourt and Garabedian presented the stability analysis of the $m = 1$ and $n = 1$ internal mode for the Heliotron E by the BETA code, which shows an average stability beta limit of 2 % for the currentless plasma in the Heliotron E configuration[9]. First we tried to reproduce the results with finer meshes than those they used to obtain the beta limit of 2 %. In the next step we compare the stability between the currentless and FCT equilibria in Heliotron E. In Sec.3.3, we examine the finite beta currentless equilibria and the stability of the $m = 1$ and $n = 1$ mode in the Heliotron H configuration under both the fixed and free boundary conditions. In both Heliotron E and Heliotron H configurations we also study the effect of the axis shift due to the additional vertical field on the stability of the $m = 1$ and $n = 1$ mode in Sec.3.4. Conclusion is given in Sec.3.5.

3.2 Ideal MHD stability of the currentless and FCT equilibria against m=1 and n=1 mode in Heliotron E

In Heliotron E, there always exists the resonant surface at $\iota = 1$ in the vacuum magnetic configuration [41]. In this case, the most unstable mode might be the internal mode with $(m, n) = (1, 1)$ localized near the ι=1 surface. Since the perturbation amplitude of the $m = 1$ internal mode is negligibly small in the region outside the ι=1 surface at $\bar{\beta} \gtrsim \bar{\beta}_c$, we may restrict our consideration to the interior region just including the resonance surface which is called an inner flux tube model of Heliotron E, where $\bar{\beta}_c$ is a stability beta limit. Bauer, Betancourt and Garabedian used this assumption to study the stability against the $m = 1$ and $n = 1$ mode in Heliotron E currentless equilibrium under the condition that the fixed boundary is put on the surface of the inner flux tube model[9]. Here we follow the same assumption and investigate the stability by using finer mesh calculations than theirs to obtain the precise result, because there are appreciable truncation errors in the numerical method implemented in the BETA code. The largest mesh number we used is $17 \times 32 \times (32 \times 18)$, where 17 refers to the radial, 32 to the poloidal and (32×18) to the toroidal directions, which became possible by using the super computer FACOM VP-100. (It is noted that we use 18 for the number of the field period to simulate the Heliotron E.) They used the maximum mesh number $9 \times 16 \times (16 \times 18)$ in CRAY-1.

Our concerns are also in the second stability region and in the comparison between the currentless and FCT equilibria about the beta limit. Thus we used an aspect ratio 13 and the coefficient $\Delta_2 = 0.27$ which describes the elliptic deformation of the outermost surface with the following expression

$$\begin{cases} r_1(u,v) &= \cos u - \Delta_2 \cos(u-v) \\ z_1(u,v) &= \sin u + \Delta_2 \sin(u-v) \end{cases} \tag{3.1}$$

(see Sec.2.4). The pressure profile is assumed to be given by

$$P = P_0(1 - 0.6\bar{r}^2)^2 \tag{3.2}$$

in the limit of a straight approximation, where $\bar{r}$ denotes an average radius. In this model pressure is finite at the surface of the inner flux tube, $\bar{r} = 1$.

First, we describe MHD equilibrium properties of the Heliotron E model. Figure 3.1 shows the magnetic surfaces for each quarter of toroidal period at $\bar{\beta}$=5.2 %, of the currentless equilibrium under the fixed boundary condition where $\bar{\beta}$ denotes the average beta value with considering the whole plasma column. At the left-hand side of each figure the axis of torus exists. It is clearly seen that the Shafranov shift of the magnetic axis due to the finite beta effect. Figure 3.2(a) shows variations of the rotational transform, $\iota(\bar{r})$, due to finite beta effects at a fixed mesh size under the condition of currentless equilibrium. There is a tendency that $\iota(0)$ increases and $\iota(1)$ decreases. At $\bar{\beta}$=5.2 %, $\iota(0) \approx 1$ and $\iota(1) \approx 1.1$ are obtained in the Heliotron E inner flux tube model. For FCT equilibria $\iota(\bar{r})$ was fixed as in Fig.3.2(b). In the equilibrium calculations of Fig.3.2(a) we used $17 \times 32 \times 32$ meshes. Figure 3.3 shows the shift of the magnetic axis for the Heliotron E inner flux tube

model obtained by using the linear extrapolations as $h \to 0$ with the mesh size h. The shift of the magnetic axis under the FCT assumption is smaller than that for the currentless equilibria.

In the stability analysis for the above heliotron configuration, ε_0=0.2 was used for the $m = 1$ and $n = 1$ mode, which denotes the amplitude of the perturbation. The test function $\mathbf{U}^d$ in Sec.2.6 for the $m = 1$ mode is specified by the following expressions

$$\begin{cases} \delta\hat{R} &= 2s^{1/2}(1-s)\cos 2\pi(u-v) \\ \delta\psi &= -(1-3s)\sin 2\pi(u-v) \\ \delta r_0 &= \cos 2\pi v \\ \delta z_0 &= \sin 2\pi v. \end{cases} \tag{3.3}$$

These forms were given to describe a strongly unstable $m = 1$ mode from various stability analyses using the BETA code. The sidebands with other poloidal and toroidal mode numbers due to geometrical coupling are produced during the process of the energy minimization.

In the BETA code the truncation errors comprise an artificial viscosity that tends to stabilize the equilibrium numerically. Therefore, it becomes necessary to perform careful convergence studies before conclusions are drawn on stability. Usually we check the dependence of the growth rate $-\omega^2$ on the mesh size h. The finite difference scheme employed in the BETA code is supposed to have an accuracy of second order $O(h^2)$ except perhaps at the magnetic axis $s = 0$ and the plasma surface $s = 1$. Therefore, we extrapolate the growth rate $-\omega^2$ to zero mesh size by choosing a representation of the

form

$$-\omega^2 = A_0 + A_2 h^2 + A_3 h^3. \tag{3.4}$$

The coefficients A_0, A_2 and A_3 are determined numerically by a least squares fit to the data for $-\omega^2$ computed at four or five different mesh sizes. The value of $-\omega^2$ usually turns out to be positive for the practical mesh sizes; however, as $h \to 0$, it decreases and may become negative in this limit. Such a case corresponds to instability. A typical example of the extrapolation curve is given in Fig.3.4. Here we used five meshes: $(7 \times 12 \times 12)$, $(8 \times 14 \times 14)$, $(9 \times 16 \times 16)$, $(13 \times 24 \times 24)$ and $(17 \times 32 \times 32)$ for one pitch length. In Fig.3.4 $h = 1$ corresponds to $(7 \times 12 \times 12)$ and the extrapolated growth rate, $-\omega^2$, becomes negative.

We discuss results of nonlinear stability against the $m = 1$ and $n = 1$ mode in the Heliotron E plasma. Figure 3.5(a) shows the eigenvalues or growth rates extrapolated by (3.4) for the $m = 1$ and $n = 1$ internal mode in Heliotron E currentless equilibria. Negative eigenvalues correspond to an unstable region against the pressure-driven internal mode, and the average beta limit 2 % is obtained which coincides with the result by Bauer et al. obtained by using crude meshes. It is also found that the second stability region appears for $\bar{\beta} \gtrsim$ 4.7 %. Figure 3.5 (b) shows the eigenvalues of the $m = 1$ and $n = 1$ mode in Heliotron E FCT equilibria. By comparing Fig.3.5 (a) with Fig.3.5 (b), the FCT equilibria are seen to be a little more unstable than the currentless equilibria. Even under the FCT assumption for the equilibrium, the second stability region of the $m = 1$ and $n = 1$ internal mode appears for $\bar{\beta} \gtrsim$ 5 %. The result that the FCT equilibria are more

unstable than the currentless equilibria agrees with the stellarator expansion analyses[17].

To understand the physical mechanism for entering the second stability region in both Figs.3.5 (a) and (b), we have examined the magnetic well term, V''/V'. Here V denotes a specific volume surrounded by a flux surface and the prime means the derivative with respect to s. Here V' is calculated by

$$V' = \int D_p du dv \tag{3.5}$$

at each flux surface and D_p is given by (2.77). The values of V''/V' obtained by the extrapolation (3.4) are plotted as a function of $\bar{\beta}$ in Fig.3.6. By noting that the $\iota=1$ surface is at $s \simeq 0.46$ for $\beta \simeq 0$ of the FCT equilibria, the second stability region appears when V''/V' at $s = 0.5$ shown in Fig.3.6(b) becomes sufficiently negative. The same situation is seen in the case of currentless equilibria shown in Fig.3.6(a). This demonstrates that the magnetic well stabilization is the main reason for entering the second stability region.

3.3 Stability of m=1 and n=1 mode in Heliotron H currentless equilibria

Heliotron E was designed and built to have a large shear to suppress the MHD instabilities. However, the average beta limit is about 2% as shown in Sec.3.2, since the $\iota = 1$ surface exists in the half radius region of the plasma column. Therefore we have interest in the heliotron/torsatron configuration without the $\iota = 1$ surface to increase the beta limit compared to Heliotron E. When the $\iota = 1$ surface is removed into the outer region and $\iota \leq 1$ in the plasma column, we obtain an example of an $\ell = 2$ torsatron such as the ATF[17]. On the other hand, an example of a heliotron with rotational transform larger than unity in the whole plasma column is Heliotron H[41]. The Heliotron H was designed to have an aspect ratio of $A = 14$ and a pitch number of 15. Here we again assume the pressure profile

$$P = P_0(1 - \bar{r}^2)^2 \tag{3.6}$$

in the limit of a straight approximation to study the stability against the $m = 1$ and $n = 1$ mode and $\Delta_2 = 0.33$ is taken in eqs.(3.1).

Our interest is in currentless equilibria for the Heliotron H configuration because the currentless constraint is more appropriate for a steady operation reactor. As shown in Fig.3.7(a) obtained under the fixed boundary condition, there is no $\iota = 1$ surface and the behaviors of the change of $\iota(\bar{r})$ due to finite beta effects are similar to the case of Heliotron E.

The eigenvalues of the $m = 1$ and $n = 1$ internal mode in the Heliotron

H equilibria are shown in Fig.3.8. The beta limit in the first stability region is $\bar{\beta} = 3.2\%$, and this configuration is more stable against the $m = 1$ and $n = 1$ internal mode than Heliotron E. This may be due to the removal of the $\iota = 1$ surface.

Next we study the stability of the external $m = 1$ and $n = 1$ mode in the currentless equilibria of the Heliotron H plasma. In this case we calculate free boundary equilibrium under the currentless constraint. The adjustable parameters are given so that the profile of the rotational transform inside the plasma column at $\beta \simeq 0$ is almost the same as that in the fixed boundary calculation. The aspect ratio of the vacuum chamber is assumed $A = 6.3$ and its shape is expressed as

$$\begin{cases} r_2(u,v) &= \cos u - \Delta_2 \cos(u-v) \\ z_2(u,v) &= \sin u + \Delta_2 \sin(u-v) \end{cases} \tag{3.7}$$

with $\Delta_2 = 0.22$ (see Sec.2.4). The pressure profile which we employ for the free boundary equilibria is given by

$$P(\bar{r}) = \begin{cases} P_0 \left[1 - \left(\dfrac{\bar{r}}{0.45}\right)^2\right]^2 & \text{for} \quad 0 \le \bar{r} \le 0.45 \\ 0 & \text{for} \quad 0.45 \le \bar{r} \le 1 \end{cases} \tag{3.8}$$

in the limit of the straight approximation. Since we consider the currentless equilibrium, the parameter C_1 corresponding to the toroidal current, which appears in the periodicity condition eq.(2.111) for the vacuum potential ϕ is taken to the zero. The coefficient C_2 in eq.(2.112) which determines the external coil current is chosen to adjust the rotational transform, and $C_2 = 2.638$ is used.

The rotational transform of the free boundary currentless equilibrium is shown for three cases, $\bar{\beta} = 0.4\%, \bar{\beta} = 1.8\%$ and $\bar{\beta} = 3.9\%$ in Fig.3.7(b). The tendency that $\iota(0)$ increases and $\iota(1)$ decreases is seen and the profile becomes almost flat at $\bar{\beta} = 3.9\%$. It is noted that $\iota(1)$ corresponds to the rotational transform at the plasma surface of the free boundary equilibria. Figure 3.9 shows the magnetic surfaces at each quarter period in the one pitch length. The magnetic axis shift by the finite beta effect in Fig.3.9 is plotted as a function of the average beta in Fig.3.10. The magnetic axis shift in the fixed boundary equilibria is also plotted for comparison. The shift in the free boundary case is estimated by

$$\delta = \frac{r_0^0 - g^{10}}{g^{00}} \tag{3.9}$$

where r_0^0, g^{00} and g^{10} are the Fourier coefficients given by

$$r_0^0 = \int_0^1 r_0(v)dv \tag{3.10}$$

$$g^{00} = \int_0^1 dv \int_0^1 du g(u,v) \tag{3.11}$$

$$g^{10} = \int_0^1 dv \int_0^1 du(\cos 2\pi u)g(u,v). \tag{3.12}$$

The coefficients g^{00} and g^{10} correspond to the average minor radius and the average shift of the toroidal plasma column, respectively (see Sec.2.4). It is seen that the larger shift occurs in the free boundary case than in the fixed boundary case. The result may be explained by the difference of the condition for the vertical magnetic field. The fixed boundary case assumes a fixed position of the plasma column, which corresponds to a situation that the plasma column position is adjusted by the vertical field to compensate

the average shift of the plasma column in the free boundary case. On the contrary the plasma column can move in the major radius direction in the free boundary equilibria.

Figure 11 shows the extrapolate curve to obtain the growth rate for the free boundary or external $m = 1$ and $n = 1$ mode in Heliotron H at $\bar{\beta} = 1.8\%$. This is the first demonstration of an unstable free boundary mode using the BETA code. Therefore, it is expected that a heliotron with large rotational transform, $1 < \iota < 2$, gives a higher beta limit than Heliotron E on the assumption of a fixed boundary; however, the free boundary mode may become crucial for such a configuration.

For these results, since the boundary condition at the free boundary is subtle from the mathematical point of view, the convergence of the iterative calculation of the minimum energy is limited to 6 digits. On the other hand, in the fixed boundary case, a convergence up to 9 to 10 digits is possible with reasonable iterations. The results under the fixed boundary condition shown in this chapter were obtained with 9 digits accuracy for the potential energy.

3.4 Effects of magnetic axis shift by additional vertical magnetic field on MHD stability

Vacuum magnetic surfaces can be controlled by adding an additional vertical magnetic field with which the magnetic axis shifts inward or outward and the shape of flux surfaces changes to have triangular component[41]. In order to study the effect of the additional vertical magnetic field by the BETA code, we employ the boundary equations expressed by

$$\begin{cases} r_1(u,v) &= [1-\Delta_3\cos(3u-v)]\cdot\cos u - \Delta_2\cos(u-v) \\ z_1(u,v) &= [1-\Delta_3\cos(3u-v)]\cdot\sin u + \Delta_2\sin(u-v) \end{cases} \tag{3.13}$$

instead of eqs.(3.1), where Δ_3 corresponds to a triangular deformation of the surface. We adjust Δ_2 and Δ_3 to describe the vacuum magnetic surface at the boundary obtained from a line tracing calculation. Figure 3.12(a) shows the flux surfaces at $\bar{\beta} \simeq 0$ when the magnetic axis is shifted outward by the additional vertical field. For this case, $\Delta_2 = 0.26$ and $\Delta_3 = 0.03$ were used as the input data of the BETA code. Figure 3.12(b) shows the flux surfaces at $\bar{\beta} \simeq 0$ for $\Delta_2 = 0.26$ and $\Delta_3 = -0.03$ with the inward axis shift. For both cases, the shift of the magnetic axis is about 8 % of the average minor radius. Dependence of the magnetic axis shift on the average beta are shown in Fig.3.13. Here we assume the same pressure profile as eq.(3.2) and the currentless constraint on the MHD equilibria. In the outward shift case by the additional vertical field, the increase of the Shafranov shift with the beta

value is relatively small compared to the opposite inward shift case.

Stability against the internal $m = 1$ and $n = 1$ mode was examined for these Heliotron E currentless equilibria with the additional vertical magnetic field and the results are shown in Fig.3.14. In the outward shift case, the $m = 1$ and $n = 1$ internal mode is stabilized completely. On the other hand, in the inward shift case the first beta limit reduces to $\bar{\beta} \simeq 1.3\%$ and growth rates become large compared to those for the standard Heliotron E configuration. In order to study the stabilizing mechanism associated with the outward axis shift we examine the depth of magnetic well since the outward magnetic shift generally enhances a good curvature region. Figure 3.15(a) and (b) show the magnetic well V''/V' in both the outward and the inward shift cases, respectively. It is seen that the magnetic well region covers almost all plasma column for $\bar{\beta} \gtrsim 3\%$ in the outward shift case. On the contrary, in the inward shift case, as shown in Fig.3.15(b), the $s = 0.5$ surface belongs to the magnetic well region for $\bar{\beta} \gtrsim 4.2\%$ which is larger than $\bar{\beta} \gtrsim 1.8\%$ in Fig.3.15(a).

We also examined the effect of the shift by an additional vertical field on the stability against the $m = 1$ and $n = 1$ internal mode in Heliotron H with the same procedure as we have used for Heliotron E. We assumed the boundary parameters $\Delta_2 = 0.33$ and $\Delta_3 = 0.03$ in eq.(3.13) and the pressure profile given by eq.(3.6). This positive Δ_3 leads about 7 % outward shift with respect to average radius. We obtained that the $m = 1$ and $n = 1$ internal mode is completely stabilized by the outward shift of the magnetic axis in the currentless MHD equilibria as shown in Fig.3.8. It is confirmed that the larger region of the plasma column belongs to the magnetic well than the

standard case at the same average beta value. The instability is considered to be stabilized by the effects of the magnetic well.

3.5 Conclusion

We have investigated the equilibrium and the stability against the $m = 1$ and $n = 1$ mode in the heliotron configurations with the three-dimensional MHD code, BETA code.

First we examined both the currentless and the FCT equilibria for the Heliotron E inner flux tube model under the fixed boundary condition. We found the tendency that the central rotational transform $\iota(0)$ increases and the edge rotational transform $\iota(1)$ decreases as the beta value increases under the currentless constraint. The Shafranov shift due to the finite beta effect in the currentless equilibrium is usually larger than that in the FCT equilibrium. Since the $\iota = 1$ surface exists in the plasma column of Heliotron E, the most dangerous instability is expected the $m = 1$ and $n = 1$ internal mode. The average beta limit of 2 % in the currentless equilibrium of Heliotron E inner flux tube model obtained by Bauer, Betancourt and Garabedian was reproduced with finer meshes. These calculation became possible by running the BETA code in the super computer FACOM VP-100. It is worth while to obtain the same beta limit, because the growth rates depend on the mesh size strongly and the value extrapolated correctly to zero mesh size has the physical meaning. We also found that a second stability region appears $\bar{\beta} \gtrsim 4.7\%$ in the Heliotron E configuration. The FCT equilibrium shows a little more unstable result to the $m = 1$ and $n = 1$ internal mode. The first stability limit is about 1.8 % and the second stability region is also found at $\bar{\beta} \gtrsim 5\%$. It is obtained that the physical mechanism for entering the second

stability region is the deepening and widening the magnetic well.

As the example of the heliotron configuration which has a rotational transform larger than unity for all flux surfaces, we studied the Heliotron H configuration under the currentless constraint. The first stability beta limit for the $m = 1$ and $n = 1$ mode is 3.2 % under the fixed boundary condition. This limit is larger than that of Heliotron E because the resonant surface, $\iota = 1$, does not exist in Heliotron H configuration. However, since ι is still close to unity, the non-resonant $m = 1$ and $n = 1$ mode is destabilized for $\bar{\beta} \gtrsim 3.2\%$. We also examined the stability of the external $m = 1$ and $n = 1$ mode in the currentless equilibrium of Heliotron H under the free boundary condition. The change of the profile of the rotational transform and the shift of the magnetic axis due to the finite beta effects is larger than these in the fixed boundary case. This may be understood by considering the difference for the vertical magnetic field constraint. In the fixed boundary case, the position of the plasma column is fixed by the vertical field. For the free boundary equilibrium the unstable external mode with $m = 1$ and $n = 1$ is found. It is remarked that the level of convergence in the free boundary calculations is degraded compared to that in the fixed boundary case.

The effects of the shift of the magnetic axis due to an additional vertical field on the global mode stability, particularly on the $m = 1$ and $n = 1$ were studied in both Heliotron E and Heliotron H. The vertical field effect on the vacuum equilibrium is included in the BETA code by deforming the boundary surface triangularly according to the results given by line tracing calculations. We obtain that when the magnetic axis is shifted inward the stability against the $m = 1$ and $n = 1$ mode degrades, whereas, when it is

shifted outward the instability completely disappears for both Heliotron E and Heliotron H currentless equilibria. It is found that the improvement of the stability is attributed to the stabilizing effect of the magnetic well on the pressure-driven instabilities. The outward shift of the magnetic axis is associated with enhancement of the good curvature region.

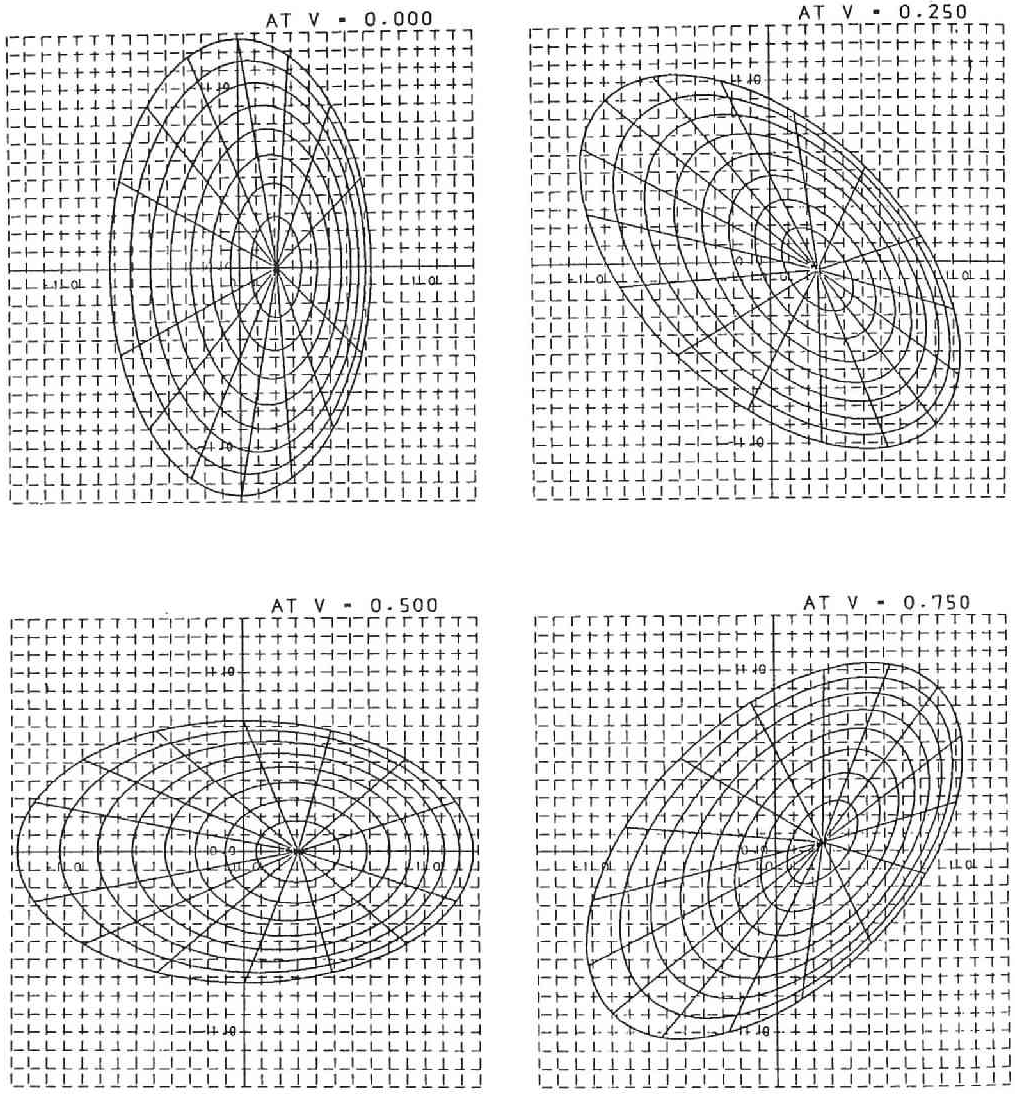

Fig.3.1 Flux surfaces of Heliotron E currentless equilibrium for $\Delta_2 = 0.27$, $A = 13$, and $\bar{\beta} = 5.2\%$ at four different cross-sections.

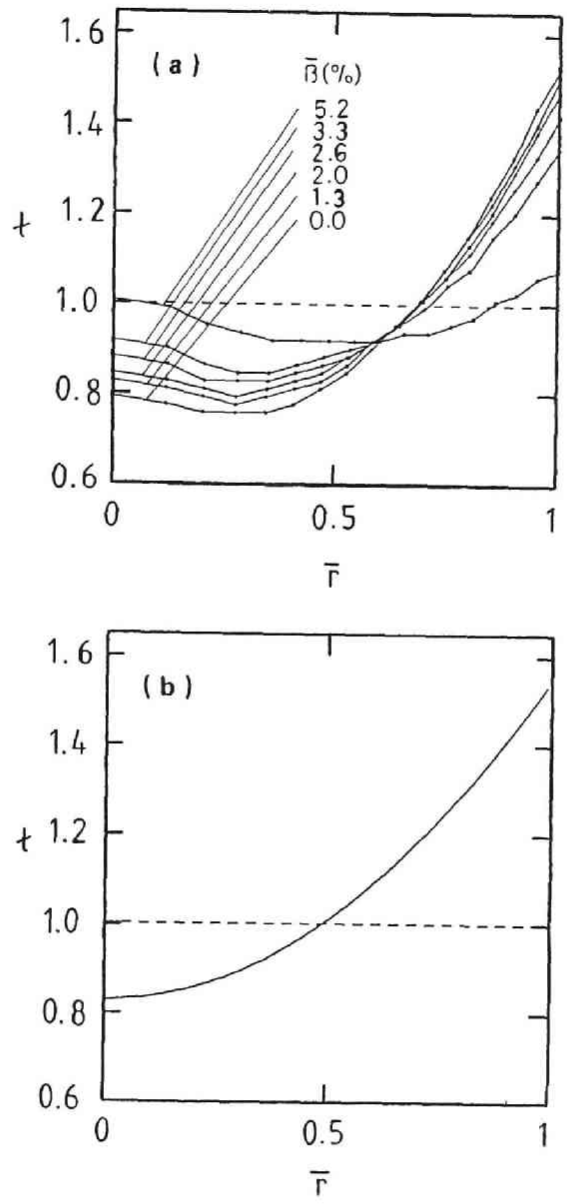

Fig.3.2 (a) Variation of rotational transform due to finite beta effects in currentless equilibria for Heliotron E by using a ($17 \times 32 \times 32$); (b) rotational transform in FCT equilibrium for Heliotron E.

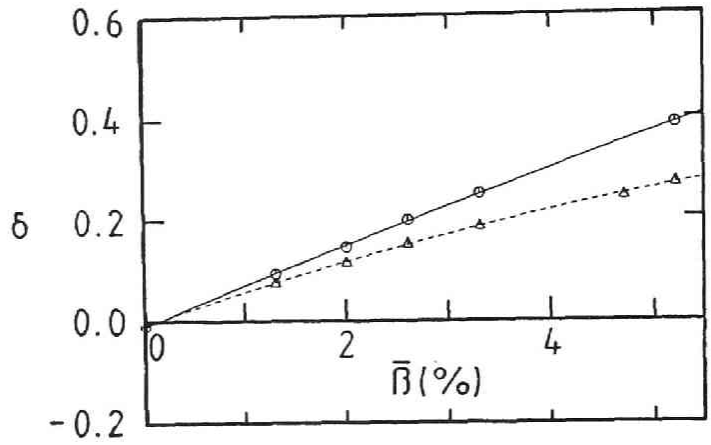

Fig.3.3 Shafranov shifts of the magnetic axis in Heliotron E. Continuous line shows currentless equilibria and dotted line shows FCT equilibria.

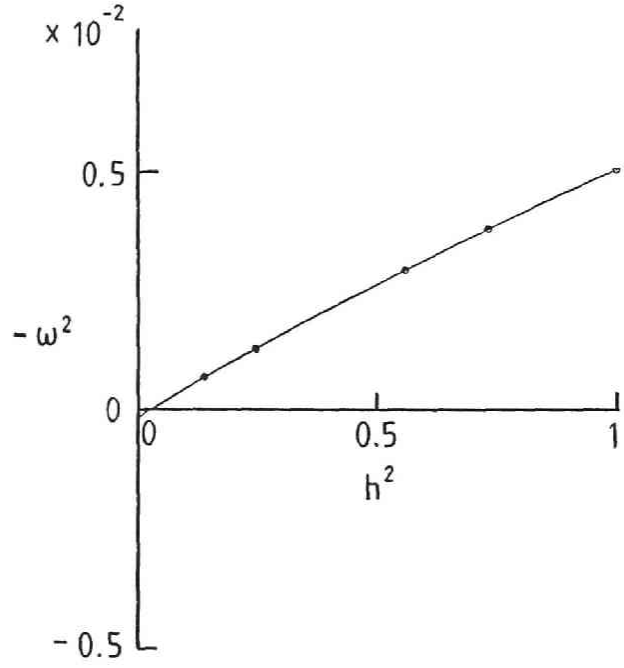

Fig.3.4 Extrapolation curve for growth rates of $m = 1$ and $n = 1$ mode in a currentless equilibrium with $\bar{\beta} = 2.6\%$. $A_0 = -0.0001593$, $A_2 = 0.0063985$, $A_3 = -0.0012352$.

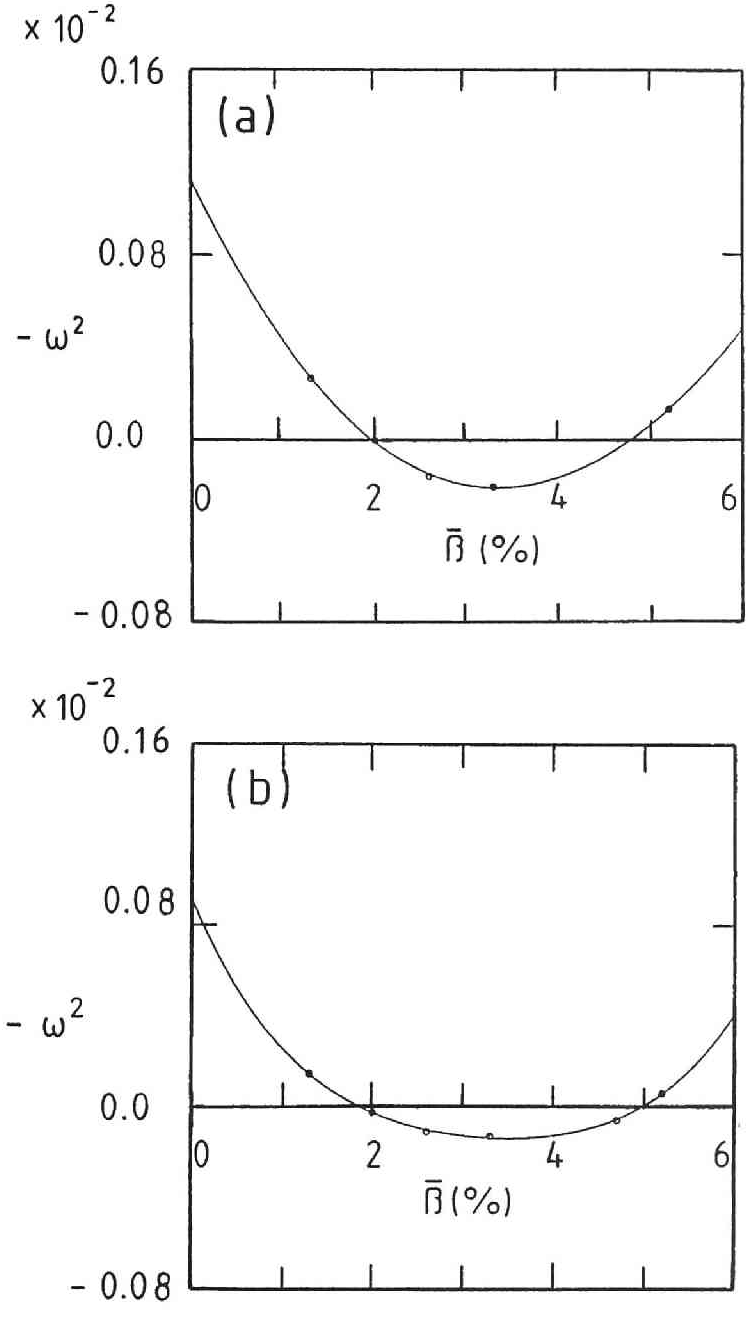

Fig.3.5 Eigenvalues of $m = 1$ and $n = 1$ internal mode versus average beta. (a) Heliotron E currentless equilibria and (b) Heliotron E FCT equilibria.

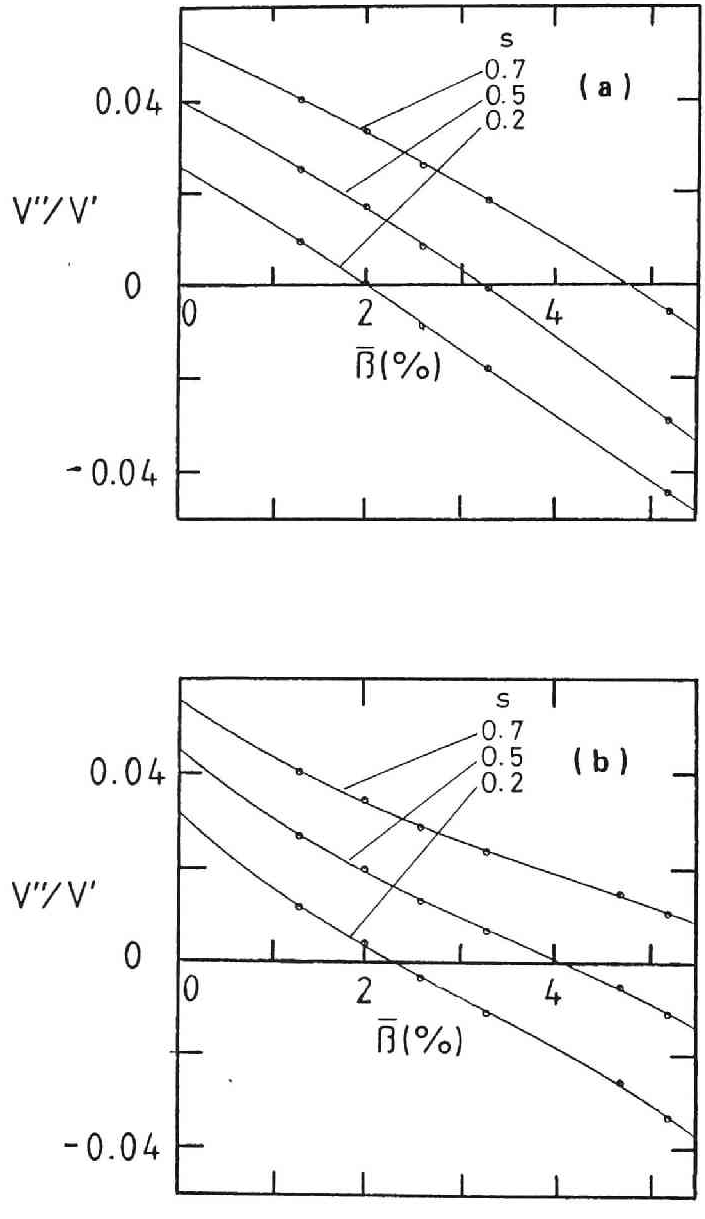

Fig.3.6 V''/V' versus $\bar{\beta}$ for three flux surfaces, $s = 0.2$, $s = 0.5$, $s = 0.7$. (a) Heliotron E currentless equilibria and (b) Heliotron E FCT equilibria.

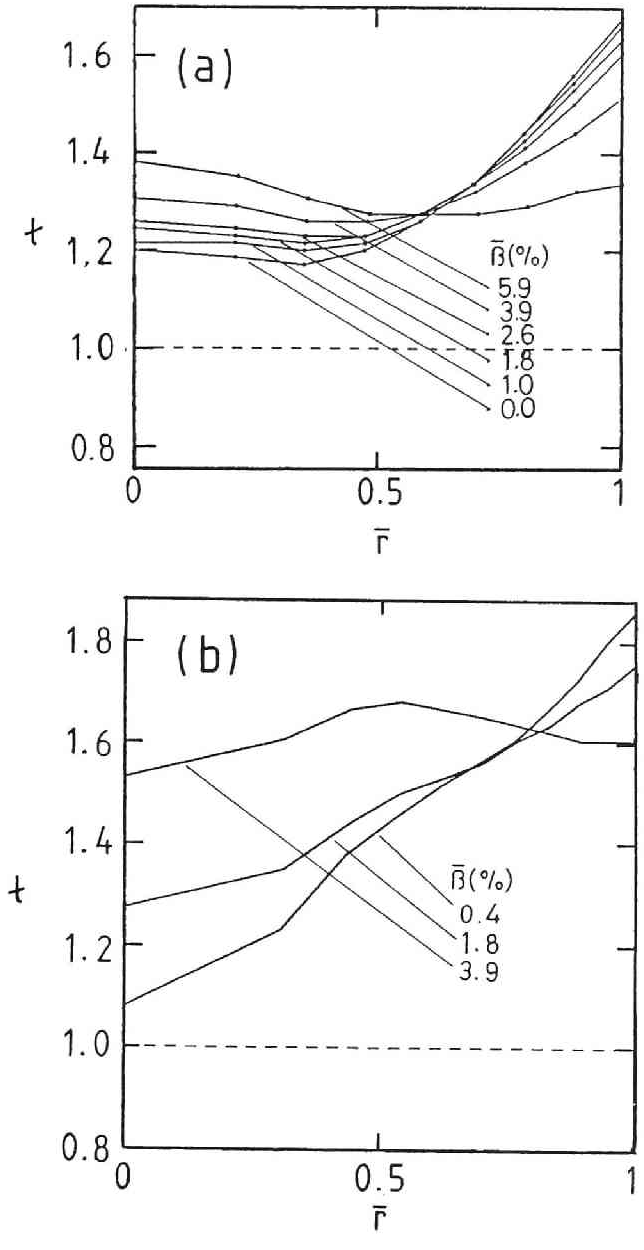

Fig.3.7 Variations of rotational transform due to finite beta effects in the currentless equilibria for Heliotron H (a) in the fixed boundary condition by using a ($9 \times 16 \times 16$) mesh; (b) in the free boundary condition by using a ($11 \times 20 \times 20$) mesh.

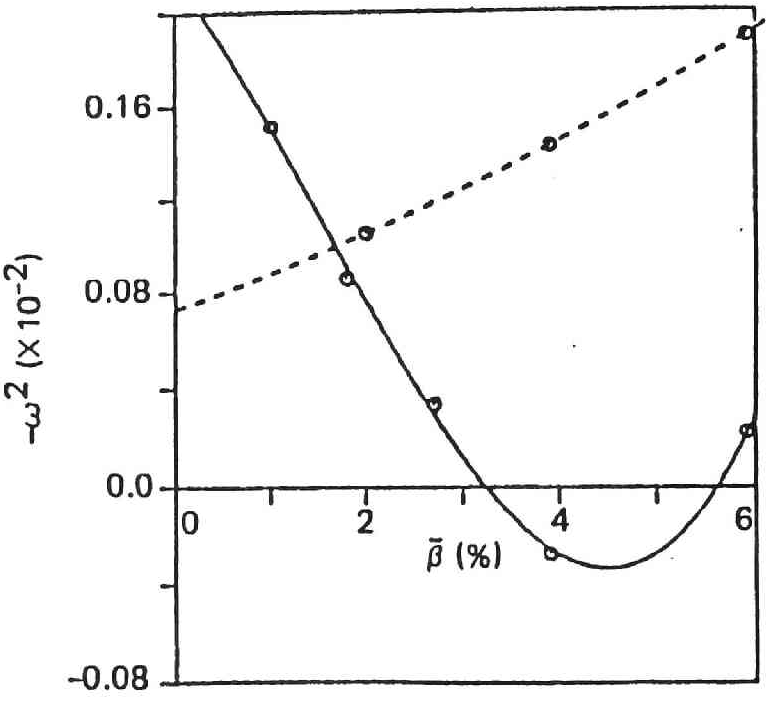

Fig.3.8 Eigenvalues of $m = 1$ and $n = 1$ internal mode versus average beta in Heliotron H currentless equilibria. Solid line shows case of standard configuration; dashed line shows case of outward magnetic axis shift.

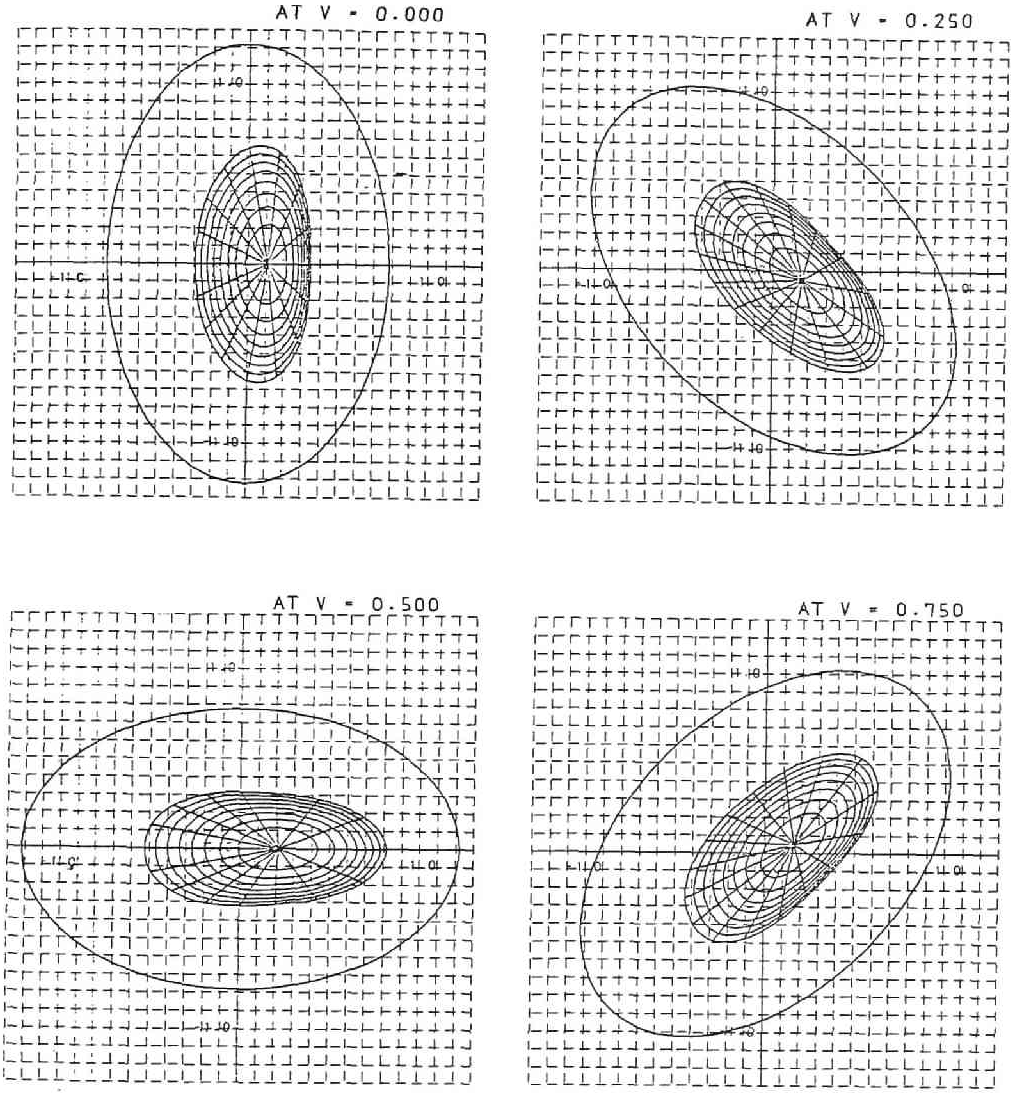

Fig.3.9 Flux surfaces of Heliotron H currentless equilibrium under the free boundary condition for $\bar{\beta} = 3.8\%$ at four different cross-sections.

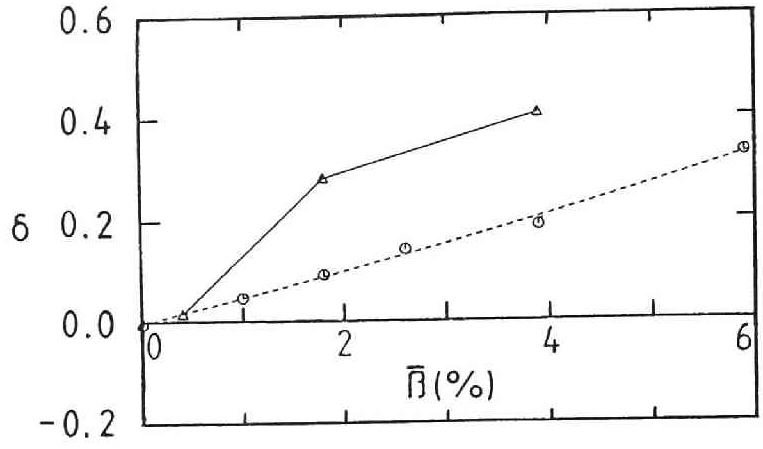

Fig.3.10 Shifts of the magnetic axis in currentless equilibria of Heliotron H plasma. Dotted line shows the shift in the fixed boundary condition and the solid line shows the one in the free boundary condition.

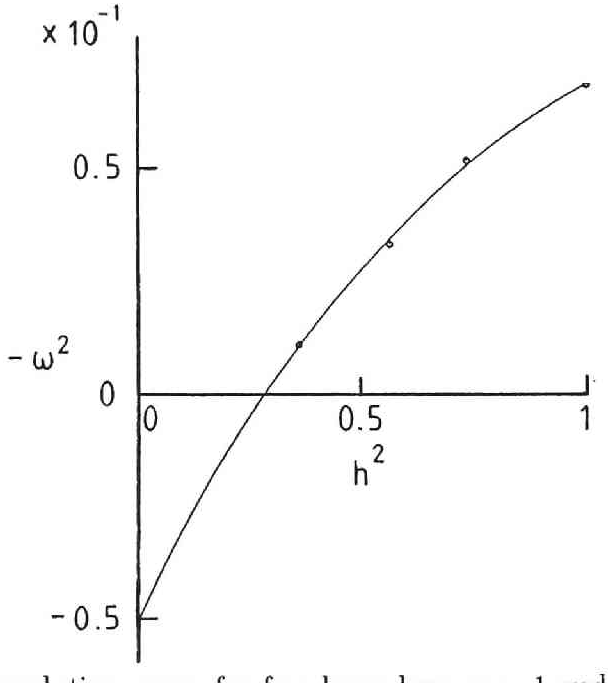

Fig.3.11 Extrapolation curve for free boundary $m = 1$ and $n = 1$ mode in Heliotron H with $\bar{\beta} = 1.8\%$. Mesh numbers $7 \times 12 \times (12 \times 15)$, $8 \times 14 \times (14 \times 15)$, $9 \times 16 \times (16 \times 15)$, and $11 \times 20 \times (20 \times 15)$ are used.

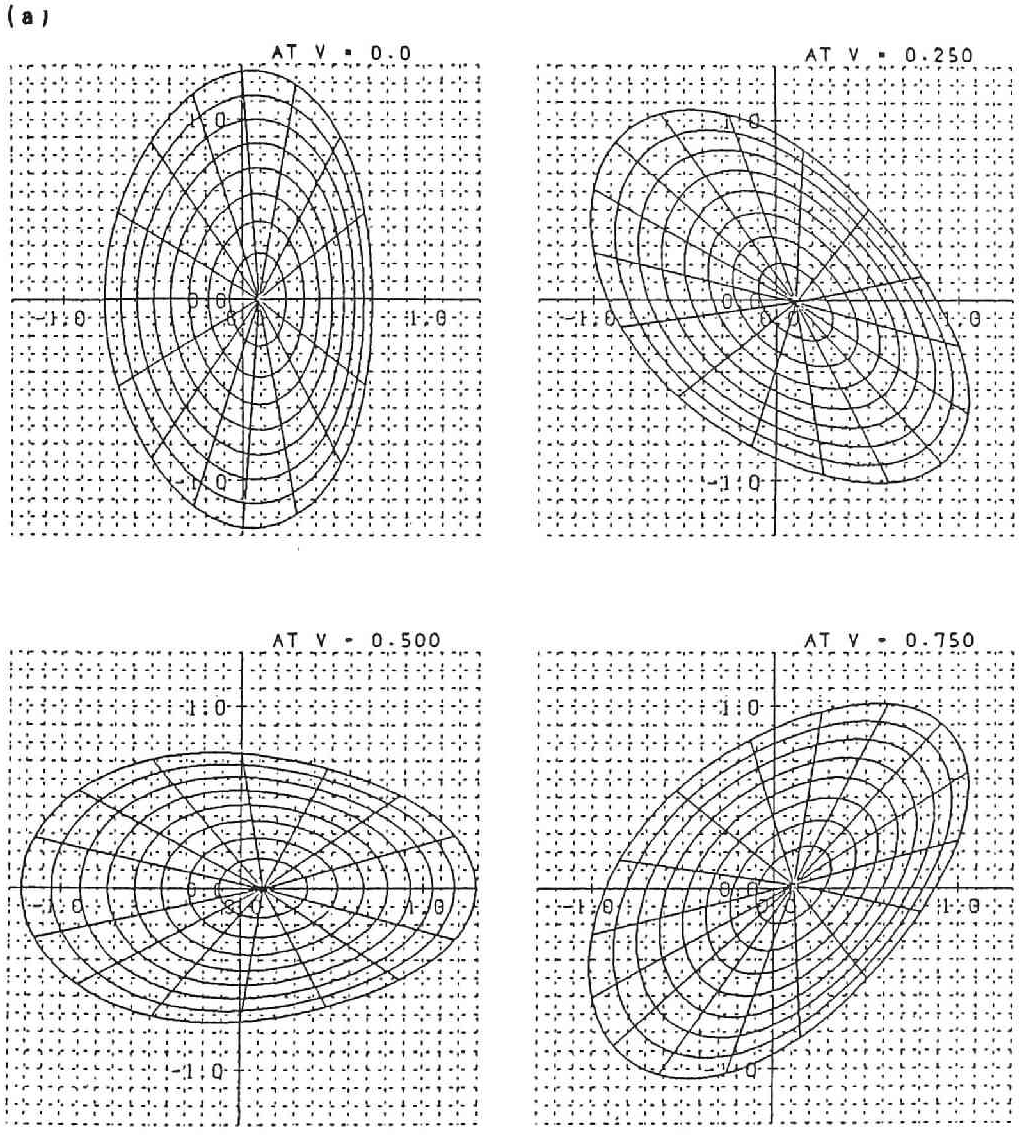

Fig.3.12 Flux surfaces for (a) $\Delta_2 = 0.26$ and $\Delta_3 = 0.03$ and (b) $\Delta_2 = 0.26$ and $\Delta_3 = -0.03$. $A = 13$ and$\bar{\beta} = 0.01\%$ for both cases.

(b)

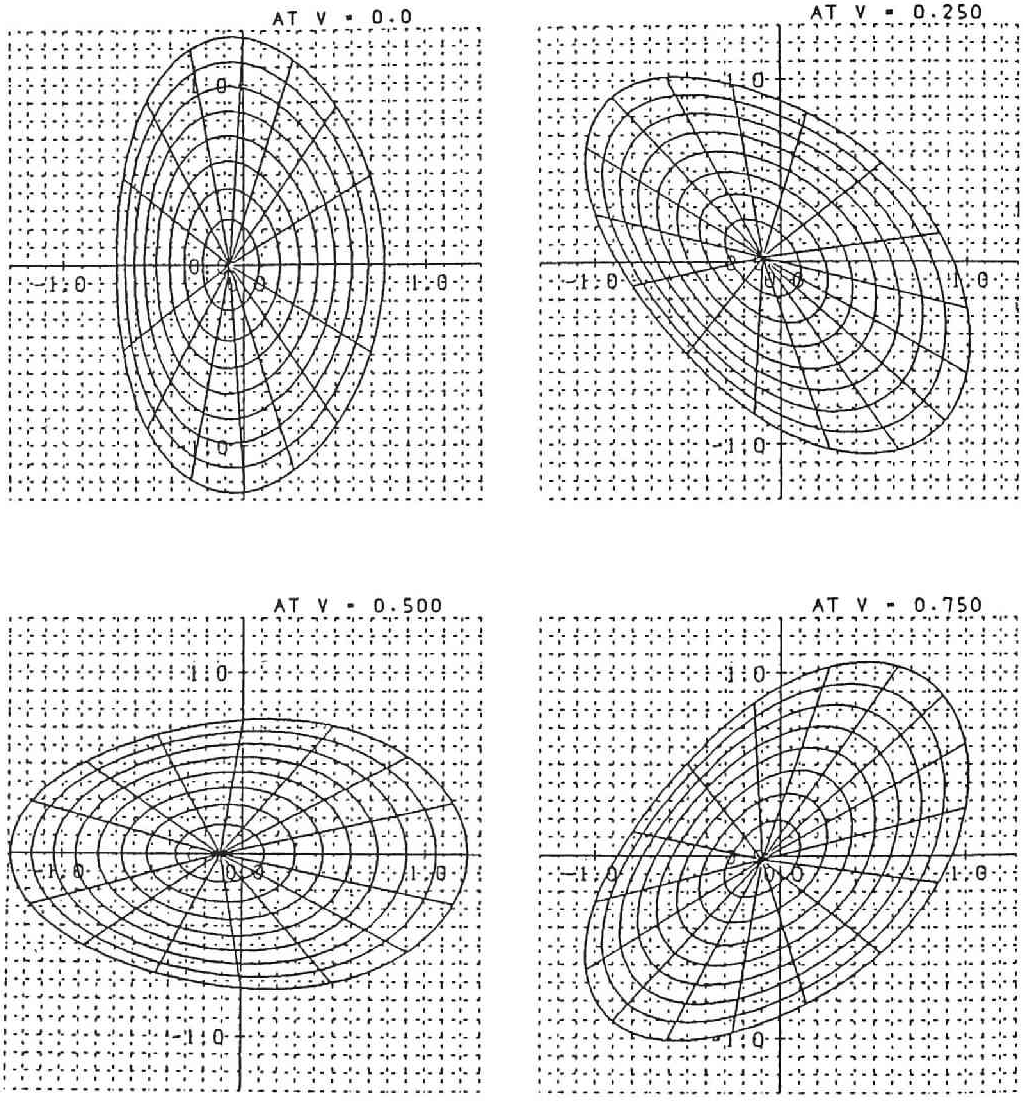

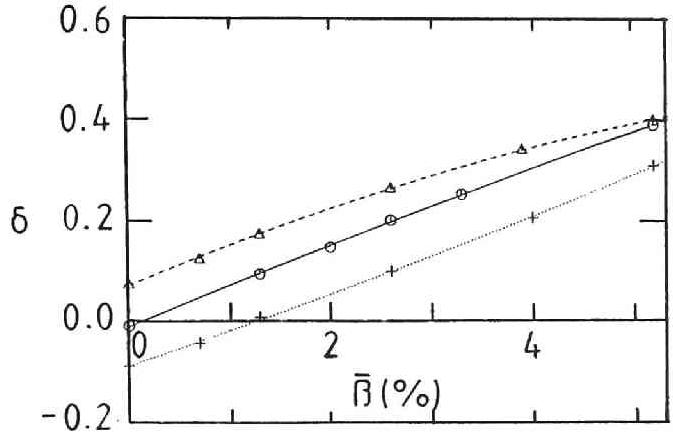

Fig.3.13 Shifts of the magnetic axis in Heliotron E currentless equilibria with the additional vertical field. Solid line shows the standard case, dashed line shows the outward shift case with $\Delta_3 = 0.03$, and dotted line shows the inward shift case with $\Delta_3 = -0.03$.

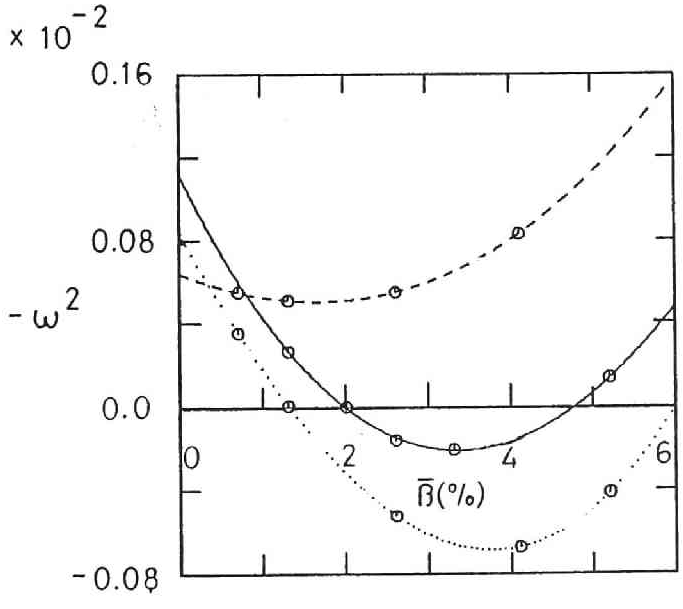

Fig.3.14 Eigenvalues of $m = 1$ and $n = 1$ internal mode in Heliotron E currentless equilibria. Solid line shows the standard case, dashed line shows the outward shift case with $\Delta_3 = 0.03$, and dotted line shows the inward shift case with $\Delta_3 = -0.03$.

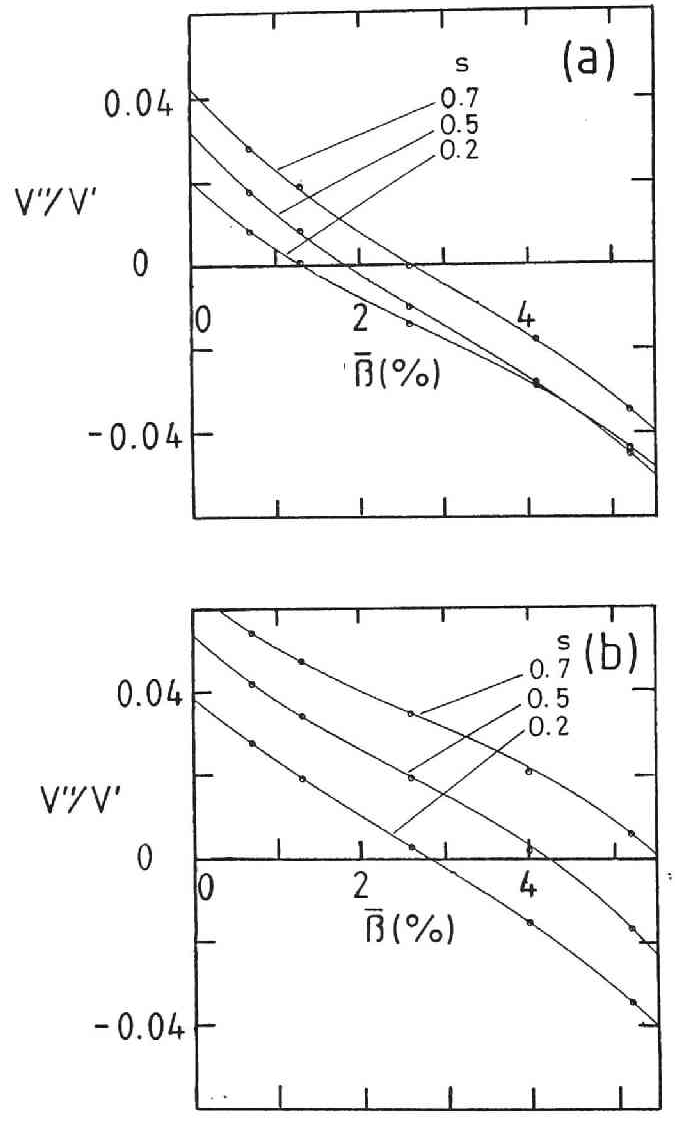

Fig.3.15 V''/V' versus $\bar{\beta}$ for three flux surfaces, $s = 0.2$, $s = 0.5$, $s = 0.7$; (a) when the magnetic axis is shifted outward and (b) when the magnetic axis is shifted inward.

Chapter 4

Ideal MHD Equilibrium and Mercier Criterion of a Spatial Axis Stellarator (Asperator NP-4)

4.1 Introduction

Since a spatial axis stellarator can have a large rotational transform as well as a magnetic well, much effort has been made to achieve a stable high beta equilibrium with this approach.

Three different methods have been used for studying the ideal MHD equilibria of spatial axis stellarators. One is the analytic method given by Solov'ev

and Shafranov[20]. In this theory the linearized MHD equilibrium equations are used, where the zeroth order corresponds to a cylindrical equilibrium and the perturbation includes both the helical and toroidal deformations. The equations are expanded in the neighborhood of the helical magnetic axis with respect to the distance from the axis. This method has been used widely to study the characteristics of equilibria analytically. A second method uses the reduced equations for the MHD equilibria, which is discussed in Chapter 1. The third approach is to make use of a three-dimensional MHD code, recognizing that there is no symmetry. Bauer, Betancourt, and Garabedian applied the BETA code to several Heliac-type configurations[9]. Hender et.al used the NEAR code[29] to study the Heliac configuration[43].

In this chapter we carry out the comparison between the analytic expressions of Solov'ev and Shafranov and numerical results of the BETA code explained in Chapter 2 for a model configuration with a circular cross-section which is similar to the Asperator NP-4[44][45]. It is interesting to compare the equilibrium quantities such as the rotational transform, the shift of magnetic axis, and the depth of magnetic well given by the Solov'ev and Shafranov theory with the numerical results to examine applicability of the theory.

In Sec.4.2, the equilibria obtained by the BETA code for the model configuration are described. In Sec.4.3, numerical results of the local stability by the Mercier criterion are discussed. Analytic results given by Solov'ev and Shafranov are reviewed in Sec.4.4. In Sec.4.5, the comparison between the numerical results and the analytic results, especially about the shift of magnetic axis and the formation of magnetic well, is carried out. The conclusion

is given in Sec.4.6. In Appendix 4.A, we discuss the coordinate transformation from the coordinates on the plane perpendicular to the axis of the chamber to the coordinates on the $v = const.$, which is needed to give the input data of the BETA code. In Appendix 4.B, the expression for the curvature and the torsion of the helical magnetic axis are given. The Mercier criterion is derived in Appendix 4.C.

4.2 Equilibrium calculation with the BETA code

The model configuration used here is a spatial axis stellarator similar to Asperator NP-4[44]. The parameters of this device are shown in Table 4-1, where the plasma radius a is introduced into the definition of the major and helical radii; hence R_0 and r_h can be normalized so that the average plasma radius is unity. In this calculation we use a fixed boundary condition at the plasma surface to obtain maximum numerical accuracy. Therefore the code requires data for the shape of the boundary on the plane of constant v as input parameters. The Asperator NP-4 was designed such that the cross-section perpendicular to the spatially helical axis of the chamber is circular, while that on the $v = const.$ plane has a non-circular shape. Thus we use the following expression for the fixed boundary described by (2.74);

$$\begin{cases} r_1(u,v) &= R_0 + r_h \cos(Nv) \\ &+ [1 + \Delta_{22}\cos 2(u - Nv) + \Delta_{33}\cos 3(u - Nv)] \cdot \cos u \\ z_1(u,v) &= r_h \sin(Nv) \\ &+ [1 + \Delta_{22}\cos 2(u - Nv) + \Delta_{33}\cos 3(u - Nv)] \cdot \sin u, \end{cases} \tag{4.1}$$

where v denotes the usual toroidal angle so that it varies $0 \leq v \leq 2\pi$ for a full torus. Δ_{22} and Δ_{33} correspond to the elliptic and the triangular deformations of the cross section, respectively. Here $\Delta_{22} = -0.15$ and $\Delta_{33} = 0.025$ are used for this model which are decided by using the transformation of coordinates

discussed in Appendix 4.A. We assume the pressure profile

$$P = P_0(1 - \rho^2)^2, \tag{4.2}$$

where ρ is the mean radius of the flux surface, and calculate MHD equilibria under the zero net current constraint as is usual for stellarators.

Figure 4.1 shows the equilibrium flux surfaces with $\bar{\beta} = 4.4$ % at every quarter period. Both the toroidal and helical shifts of the magnetic axis can be seen. Here the helical shift points to the principal normal direction of the axis. We will discuss this problem quantitatively in Sec.4.5. Figure 4.2 shows the profiles of rotational transform ι per one period for the equilibria with several values of beta. The profile at nearly zero beta value is almost flat and the shear is fairly weak. As the beta value increases, the transform increases at the center and decreases at the edge under the currentless constraint for the equilibria. This tendency is similar to that in the currentless finite beta equilibrium of Heliotron E in Chapter 3. Although a weak negative shear appears in the finite beta plasmas, the currentless equilibrium of the Asperator NP-4 seems to keep a property of FCT equilibrium up to a few percent of $\bar{\beta}$ because of the large rotational transform.

We evaluate the shifts of the magnetic axis on the plane perpendicular to the axis of the chamber in order to compare them with the analytic results that will be discussed in Sec.4.5. The position of this axis that is seen in Fig.4.1 is expressed as Fourier series,

$$\begin{cases} r_0(v) &= r_{00} + r_{01}\cos(Nv) \\ &+ r_{02}\cos(2Nv) + r_{03}\cos(3Nv) \\ z_0(v) &= z_{01}\sin(Nv) \\ &+ z_{02}\sin(2Nv) + z_{03}\sin(3Nv). \end{cases} \tag{4.3}$$

Figure 4.3 shows the projection of the helical axis onto the plane perpendicular to the magnetic axis over one period for several values of beta, which is obtained by transforming the position of eq.(4.3) to the plane perpendicular to the magnetic axis with the matrix in Appendix 4.A. The origin denotes the axis of the chamber. The X and Y axes indicate the principal normal and binormal directions of the helical magnetic axis, respectively. For each value of $\bar{\beta}$, the helical shift corresponds to the mean value $(X_0, 0)$ of the X coordinates over this closed line and the toroidal shift to the mean value of the distance from this $(X_0, 0)$ point to a point on this closed line. In Fig.4.4 we plot these shifts versus the beta value.

The magnetic well or hill $V''(s)/V'(s)$ associated with the normal curvature is frequently used as a stability criterion, and is shown in Fig.4.5. At $\bar{\beta} \sim 0.0\%$ the whole plasma region is in the magnetic hill. Magnetic well region appears near the magnetic axis at $\bar{\beta} \sim 1\%$.

In order to investigate equilibrium properties of the spatial axis stellarator, we deform the boundary shape to include triangularity. The model configurations used in this study have the same parameters as in Table 4.1 except the minor radius which is 0.85 times as small as that of Asperator NP-4. We fixed the elliptic deformation parameter in the BETA code at $\Delta_{22} = -0.15$ and varied only the triangularity parameter Δ_{33} on the $v = const.$ plane

from 0.0 to 0.1. The effect of the triangular deformation for the boundary flux surface is also seen on the plane perpendicular to the helical axis of the chamber. It is confirmed that $\Delta_{33} = 0.025$ corresponds to the circular boundary shape like the Asperator NP-4.

First we evaluate effects of triangularity on the equilibrium properties at $\bar{\beta} = 0.0\%$. Figure 4.6 shows the profile of rotational transform for various Δ_{33} at $\bar{\beta} = 0.0\%$. It is seen that the shear near the magnetic axis becomes strong according to the increase of Δ_{33}. In Fig.4.7 we plot the magnetic well V''/V' at $\bar{\beta} = 0.0\%$. For $\Delta_{33} \geq 0.5$, the magnetic well region appears near the magnetic axis. Thus, it is expected that spatial axis stellarators with cross-sections including triangularity have the more favorable stability than that with a circular cross-section.

Next we study the finite beta effect on the $\Delta_{22} = -0.15$ and $\Delta_{33} = 0.1$ configuration which has the deepest magnetic well and the largest shear as shown in Figs.4.6 and 4.7 at $\bar{\beta} = 0.0\%$. Figure 4.8 shows the profiles of rotational transform at various beta values under the currentless constraint. While $\iota(1)$ decreases with beta value as in the Asperator NP-4 case, $\iota(0)$ also decreases in this configuration. Therefore the shear still exists near the magnetic axis at $\bar{\beta} = 5.4\%$. This tendency is not seen in the circular cross-section case (see Fig.4.2). As shown in Fig.4.9, both the helical and the toroidal shifts of magnetic axis are smaller than those of the Asperator NP-4 model in Fig.4.4. It is found that the triangular deformation reduces the magnetic axis shift in the spatial axis stellarator. This indicates the favorable property of the spatial axis stellarator with the triangular boundary concerning of the high beta equilibria. Figure 4.10 shows that V''/V' becomes

negative in the almost all region of the plasma column at $\bar{\beta} = 1.0\%$, because the present model spatial axis stellarator already has the fairly wide well region at $\bar{\beta} = 0.0\%$.

4.3 Mercier stability of Asperator NP-4

By using the BETA code the local stability is examined for the calculated three-dimensional MHD equilibrium. The sufficient and necessary condition for the local mode is given by the Mercier criterion[46,47]. It is obtained from minimization of the potential energy in the limit that the mode is localized at the rational surface. The derivation of this criterion is given in Appendix 4.C. When we employ the (s, u, v) coordinates used in BETA code, this criterion is also expressed by

$$\Omega = \Omega_S + \Omega_{J\cdot B} + \Omega_W + \Omega_{P.S.} > 0, \tag{4.4}$$

where

$$\Omega_S = \frac{(\iota')^2}{4} \tag{4.5}$$

is the shear term,

$$\Omega_{J\cdot B} = -\iota' \int\int \frac{(\mathbf{J} - I'\mathbf{B})\cdot\mathbf{B}}{|\nabla s|^2} D_p du dv \tag{4.6}$$

is the $\mathbf{J}\cdot\mathbf{B}$ term,

$$\Omega_W = P'\left[V'' - P'\int\int \frac{D_p du dv}{B^2}\right]\int\int \frac{B^2}{|\nabla s|^2} D_p du dv \tag{4.7}$$

is the magnetic well term, and

$$\Omega_{P.S.} = \left[\int\int \frac{\mathbf{J}\cdot\mathbf{B}}{|\nabla s|^2} D_p du dv\right]^2 - \int\int \frac{B^2}{|\nabla s|^2} D_p du dv \int\int \frac{(\mathbf{J}\cdot\mathbf{B})^2}{B^2|\nabla s|^2} D_p du dv \tag{4.8}$$

is Pfirsch-Schlüter current term which is destabilizing by the geodesic curvature or the component in the $\mathbf{B}\times\nabla s$ plane of the curvature vector of the magnetic field line.

In Fig.4.11 we plot the quantity Ω and the the terms of eqs.(4.5) $\sim$ (4.8) separately as a function of s obtained by the BETA code for the Asperator NP-4 currentless equilibrium. For comparison we also show the same quantities in Fig.4.12 in the case of Heliotron E which has 19 field periods, the aspect ratio of 11, and the the ellipticity $\Delta_2 = 0.26$ in eq.(3.1) with the parabolic pressure profile. All data are extrapolated values to the zero mesh size from three sets of grids $(9 \times 16 \times 16), (17 \times 32 \times 32)$, and $(25 \times 48 \times 48)$.

In the Asperator NP-4 case, Ω is negative in the whole region of the plasma column for all beta values, and the higher is the β, the larger is the absolute values of Ω. Because the shear is weak as shown in Fig.4.2, and Ω_S and $\Omega_{J\cdot B}$ proportional to the shear do not contribute to the stability, shear stabilization is not expected. For $\bar{\beta} \gtrsim 2\%, \Omega_W$ becomes positive and the stabilizing effects appear; however, the destabilizing contribution of the geodesic curvature $\Omega_{P.S.}$ is larger than the stabilizing contribution from the magnetic well due to the normal curvature. Therefore total value of Ω becomes negative. On the other hand, because the Heliotron E model has a strong shear as shown in Fig.4.12(b), Ω in the edge region keeps positive even for $\bar{\beta} \gtrsim 1.0\%$ as shown in Fig.4.12(a). We see a tendency that Ω has a large negative value at the inner region of the plasma column when $\bar{\beta}$ is increased. The result that the main contribution at large $\bar{\beta}$ values comes from the Pfirsch-Schlüter current term are the same as that in the Asperator NP-4 case. However, the stabilizing effect of the magnetic well in Asperator NP-4 model is relatively larger than that in the Heliotron E model. From the comparison of the Mercier criterion for the Heliotron E model between the BETA code and the VMEC code [33], it is pointed out that the BETA

code may underestimate the stabilizing contribution of the magnetic well term[48]. If this is general, the Asperator NP-4 configuration may have the more optimistic stability property than that in Fig.4.11.

4.4 Equilibrium of spatial axis stellarator by the Solov'ev-Shafranov theory

The finite beta equilibrium of the spatial axis stellarator has been analytically studied by Solov'ev and Shafranov [20], and the result relevant to the subject of this chapter is summarized here.

Since the spatial axis stellarator is characterized by the helical magnetic axis, it is convenient to use a generalized curvilinear coordinates for the description of MHD equilibrium. The (ρ, ω, η) coordinates are used by Solov'ev and Shafranov, which are also called Mercier coordinates. The magnetic axis is regarded as a coordinate and η is the length along this axis. On the $\eta = const.$ plane ρ is the distance from the axis, and the azimuthal angle θ is measured from the principal normal direction. However, since the (ρ, θ, η) coordinates are not orthogonal system, the new angle ω is introduced by

$$\omega = \theta + \int_0^\eta \kappa(\eta) d\eta, \tag{4.9}$$

where $\kappa(\eta)$ is the torsion of the magnetic axis. With Frenet's formula the line element of the (ρ, ω, η) coordinates is given by

$$dl^2 = d\rho^2 + \rho^2 d\omega^2 + (1 - k\rho\cos\theta)^2 d\eta^2, \tag{4.10}$$

where $k(\eta)$ is the curvature of the magnetic axis. We normalize k, κ, ρ and η to the plasma radius a.

The quantity $k\cos\theta$ in the metric of (4.10) is expanded by using Fourier

series such that

$$k(\eta)\cos\theta = \sum_{n=-\infty}^{\infty} k_n \cos[\omega - \kappa_n \eta], \tag{4.11}$$

where

$$\kappa_0 = \frac{1}{L}\int_0^L \kappa(\eta)d\eta, \qquad \kappa_n = \kappa_0 - \frac{2\pi n}{L}, \tag{4.12}$$

$$k_n = \frac{1}{L}\int_0^L k(\eta)\cos\left(\kappa_n\eta - \int_0^\eta \kappa(\eta)d\eta\right)d\eta, \tag{4.13}$$

and L denotes the length of the magnetic axis for one period,

$$L = 2\pi r_h\left[1+\left(\frac{R_0}{Nr_h}\right)^2\right]^{1/2}. \tag{4.14}$$

Here we have assumed $N \gg 1$. Note that the relation (4.12) corresponds to the case where the winding of the magnetic axis is clockwise, while in the anticlockwise winding case

$$\kappa_n = \kappa_0 + \frac{2\pi n}{L}. \tag{4.15}$$

In the spatial axis stellarator, the rotational transform, ι, is produced by the torsion. This point is quite different from the method to produce the rotational transform in the heliotron/torsatron. The value near the magnetic axis per one period is given by the expression

$$\iota = 1 - \left|\int_0^L \kappa(\eta)d\eta\right|. \tag{4.16}$$

In the approximation of the straight helical geometry the curvature and the torsion are described by

$$\bar{k} = \frac{1}{r_h\left[1+\left(\frac{R_0}{Nr_h}\right)^2\right]}, \qquad \bar{\kappa} = \frac{\frac{R_0}{Nr_h}}{r_h\left[1+\left(\frac{R_0}{Nr_h}\right)^2\right]}. \tag{4.17}$$

Hence the rotational transform is expressed as

$$\iota = 1 - \frac{\bar{\kappa} L}{2\pi}. \tag{4.18}$$

The dashed line in Fig.4.2 shows the value given by (4.18) for the case of Asperator NP-4. Good agreement with the numerical results is obtained.

In the Mercier coordinates, we can show the equation to determine the shift of the flux surface in the finite beta equilibrium. We use the static equilibrium equations (2.9)$\sim$(2.11). By considering that a cylindrical plasma is deformed to have a helical magnetic axis, the equilibrium quantities are linearized such as

$$\begin{aligned} P &= P_0(\rho) + P_1(\rho, \omega, \eta) \\ \mathbf{B} &= \mathbf{B}_0(\rho) + \mathbf{B}_1(\rho, \omega, \eta) \\ \mathbf{J} &= \mathbf{J}_0(\rho) + \mathbf{J}_1(\rho, \omega, \eta) \end{aligned} \tag{4.19}$$

where the zeroth order corresponds to cylindrical symmetric equilibrium. The perturbed quantities due to the deformation are expanded by employing the torsion,

$$\begin{aligned} P_1(\rho, \omega, \eta) &= \sum_n P_n(\rho) \cos(\omega - \kappa_n \eta) \\ \mathbf{B}_1(\rho, \omega, \eta) &= \sum_n \mathbf{B}_n(\rho) \cos(\omega - \kappa_n \eta) \\ \mathbf{J}_1(\rho, \omega, \eta) &= \sum_n \mathbf{J}_n(\rho) \cos(\omega - \kappa_n \eta). \end{aligned} \tag{4.20}$$

The position of the center of a shifted magnetic surface with radius ρ_0 can be obtained by expanding

$$\begin{aligned} \rho &= \rho_0 + \xi(\rho_0, \omega, \eta) \\ &= \rho_0 + \sum_n \xi_n(\rho_0) \cos(\omega - \kappa_n \eta) \end{aligned} \tag{4.21}$$

and substituting (4.20) into the linearized MHD equations. Here perturbation of the pressure is given by

$$P_1(\rho_0, \omega, \eta) = -\xi(\rho_0, \omega, \eta)\frac{dP_0}{d\rho_0}. \tag{4.22}$$

Then, the equilibrium equations (2.9)$\sim$(2.11) with the expansions (4.20) give an ordinary differential equation for $\xi_n(\rho)$,

$$\begin{aligned} &\frac{1}{\rho_0}\frac{d}{d\rho_0}\left[\rho_0\frac{(B_{\omega 0}-\kappa_n\rho_0 B_{\eta 0})^2}{1+\kappa_n^2\rho_0^2}\frac{d\xi_n}{d\rho_0}\right] \\ &+\frac{\kappa_n^2\xi_n - k_n}{1+\kappa_n^2\rho_0^2}\left[2\frac{B_{\omega_0}^2-\kappa_n^2\rho_n^2 B_{\eta 0}^2}{1+\kappa_n^2\rho_0^2} - (B_{\omega 0}-\kappa_n\rho_0 B_{\eta 0})^2 - 2\rho_0\frac{dP_0}{d\rho_0}\right] \\ &= 0, \end{aligned} \tag{4.23}$$

where $B_{\omega 0}$ and $B_{\eta 0}$ denote the ω and η components of the confining magnetic field, respectively.

If we assume

$$|\kappa_n^2\xi_n| \ll 1, \quad |\kappa_n\rho| \ll 1, \tag{4.24}$$

we can integrate eq.(4.23) and we obtain

$$\xi_n = k_n\int_{\rho_1}^{\rho_2}\rho_0\frac{G}{D}d\rho_0, \tag{4.25}$$

which implies the Fourier coefficient of the relative displacement between the surface with radius ρ_1 and that with ρ_2. Here,

$$\begin{aligned} G &= 2[\langle P_0\rangle_\rho - P_0(\rho)] + \frac{1}{2}[\langle B_{\omega 0}^2\rangle_\rho \\ &\quad +2\langle\kappa_n\rho B_{\omega 0}B_{s0}\rangle_\rho - 3\langle\kappa_n^2\rho^2 B_{s0}^2\rangle_\rho] \end{aligned} \tag{4.26}$$

$$D = [B_{\omega 0}(\rho) - \kappa_n\rho B_{s0}(\rho)]^2, \tag{4.27}$$

and the bracket $\langle f \rangle_\rho$ denotes the surface average defined by

$$\langle f \rangle_\rho = \frac{1}{\pi\rho^2} \int_0^{2\pi} d\omega \int_0^\rho f(\rho, \omega, \eta) \rho d\rho. \tag{4.28}$$

When we take $\rho_1 = 0$ and $\rho_2 = a$ in eq.(4.25), ξ_n means the shift of the magnetic axis in the fixed boundary condition. This estimation for the Asperator NP-4 configuration will be discussed in the following section. On the other hand, we can also estimate the shift of the center of the plasma column by taking $\rho_1 = b$ and $\rho_2 = a$, where b is the radius of the circular wall. Here we assume

$$\begin{cases} P_0 &= 0 \\ B_{\omega 0} &= I/\rho_0 \qquad \text{for} \quad a \le \rho_0 \le b \\ B_{s0} &= B_{s0}(a) = \text{const.} \end{cases} \tag{4.29}$$

Then we have the expression,

$$\begin{aligned} \xi_n \;=\; & -\frac{3}{8} k_n b^2 \left(1 - \frac{a^2}{b^2}\right) \\ & + \frac{k_n a b}{2[B_{\omega 0}(a) - \kappa_n a B_{s0}][B_{\omega 0}(b) - \kappa_n b B_{s0}]} \\ & \cdot \left\{ \left(2\langle P \rangle_a + \frac{\langle B_\omega^2 \rangle_a}{2} + \langle \kappa \rho B_\omega B_{s0} \rangle_a \right) \left(1 - \frac{a^2}{b^2}\right) \right. \\ & + B_{\omega 0}^2(a) \left[\ln \frac{b}{a} + \frac{1}{4} \left(1 - \frac{a^2}{b^2}\right) \right] \\ & \left. - \kappa_n a B_{s0} B_{\omega 0}(a) \left[\ln \frac{b}{a} + 1 - \frac{b^2}{a^2} \right] \right\}, \end{aligned} \tag{4.30}$$

where $\langle f \rangle_\rho$ in G is replaced by $\langle f \rangle_a$. In the currentless case of stellarator, which corresponds to $B_{\omega 0} = 0$, we obtain

$$\xi_n = -\frac{3}{8} k_n b^2 \left(1 - \frac{a^2}{b^2}\right) + \frac{k_n \bar{\beta}}{2\kappa_n^2} \left(1 - \frac{a^2}{b^2}\right). \tag{4.31}$$

Equation (4.30) is also applicable to the shift of tokamak. Putting $k_n = 0$ for $n \neq 0$ and $k_0 = R$, we obtain a familiar expression for the Shafranov shift in a circular tokamak with a large aspect ratio,

$$\xi = \frac{b^2}{2R}\left\{\ln\frac{b}{a} + \left(1 - \frac{a^2}{b^2}\right)\left(\frac{2\langle p\rangle_a}{B_{w0}^2(a)} + \frac{\ell_i - 1}{2}\right)\right\}, \tag{4.32}$$

where

$$\ell_i = \frac{\langle B_w^2\rangle}{B_w^2(a)}, \tag{4.33}$$

which is called an internal inductance.

The local MHD stability depends on the magnetic well which has a stabilizing effect. It can be estimated from the equilibrium solution given by eq.(4.23). In the Mercier coordinates the specific volume $V'(\Phi)$ is expressed as

$$V'(\Phi) = \frac{dV}{d\Phi} = \oint \frac{1 - \langle k\rho\cos\theta\rangle}{\langle B_\eta\rangle} d\eta, \tag{4.34}$$

where line integral is carried out over the one period of the spatial axis stellarator. Since B_η is approximated as

$$B_\eta = \frac{B_0(\eta)}{1 - k\rho\cos\theta}, \tag{4.35}$$

we have the expression

$$V'(\Phi) = \oint \frac{1 - 2\langle k\rho\cos\theta\rangle - \langle k^2\rho^2\cos^2\theta\rangle - \langle k\rho\cos\theta\rangle^2}{B_0(\eta)} d\eta. \tag{4.36}$$

The well depth can be obtained by substituting (4.21) into (4.36).

4.5 Comparison between numerical results and the Solov'ev-Shafranov theory

In this section, we derive the equations for the shift of the magnetic axis and the magnetic well due to the finite beta effect based on the Solov'ev and Shafranov theory discussed in Sec.4.4, and compare the results of the BETA code with this expressions for the Asperator NP-4 equilibrium.

We estimate the shift of the magnetic axis in the following way. In the eq.(4.25), by using the pressure profile (4.2) and the currentless constraint or $B_{\omega 0} = 0$, we find the relative shift $\xi_n(\rho_0)$ between the magnetic axis and the surface with radius ρ_0 given by

$$\xi_n(\rho_0) = -\frac{3}{8}k_n\rho_0^2 + \frac{k_n\bar{\beta}}{2\kappa_n^2}\frac{\rho_0^2}{a^2}\left(3 - \frac{\rho_0^2}{a^2}\right). \tag{4.37}$$

We need the explicit expressions for k_n and κ_n in order to evaluate ξ_n. In the Asperator NP-4 case, we assume the expressions for the curvature and the torsion of the helical magnetic axis as(see Appendix 4.B),

$$k = \bar{k} + \tilde{k}\cos\frac{2\pi\eta}{L} \tag{4.38}$$

$$\kappa = -\bar{\kappa} + \tilde{\kappa}\cos\frac{2\pi\eta}{L}, \tag{4.39}$$

where $\tilde{k}$ and $\tilde{\kappa}$ mean toroidal corrections of the curvature and the torsion, respectively. These equations are consistent with the anticlockwise winding of the magnetic axis in the BETA code. Equations (4.15) and (4.39) give

$$\kappa_n = -\bar{\kappa} + \frac{2\pi n}{L}. \tag{4.40}$$

Substituting eqs.(4.38), (4.39) and (4.40) into eq.(4.13), we have the expression,

$$k_n = \bar{k} J_n \left(\frac{\tilde{\kappa} L}{2\pi} \right) + \frac{1}{2} \tilde{k} \left[J_{n+1} \left(\frac{\tilde{\kappa} L}{2\pi} \right) + J_{n-1} \left(\frac{\tilde{\kappa} L}{2\pi} \right) \right], \tag{4.41}$$

where J_n is the Bessel function of the n-th order. For the parameters of the model configuration shown in Table 4-1, $\tilde{k} \ll \bar{k}$ and the first term is dominant in (4.41) as discussed in Appendix 4.B. Equations (4.41) shows that k_n becomes smaller as $\mid n \mid$ increases, and $k_{-1} \sim k_1$ and $\kappa_{-1} > \kappa_1$. Then we have

$$\left| \frac{k_{-1}}{2\kappa_{-1}^2} \right| \ll \left| \frac{k_0}{2\kappa_0^2} \right| \sim \left| \frac{k_1}{2\kappa_1^2} \right|. \tag{4.42}$$

Therefore, (4.21) is assumed by

$$\begin{aligned} \rho &\sim \rho_0 + \xi_0 \cos(\omega - \kappa_0 \eta) + \xi_1 \cos(\omega - \kappa_1 \eta) \\ &\sim \rho_0 + \xi_0 \cos\theta + \xi_1 \cos(\theta - \frac{2\pi\eta}{L}). \end{aligned} \tag{4.43}$$

It is shown that ξ_0 and ξ_1 in(4.43) correspond to the helical shift and the toroidal shift of the magnetic axis, respectively, when $\rho_0 = a$ is substituted into eq.(4.37). After normalizing all values by a, they are written by

$$\xi_0 = -\frac{3}{8} k_0 + \frac{k_0 \bar{\beta}}{\kappa_0^2} \tag{4.44}$$

with

$$k_0 = \bar{k} J_0 \left(\frac{\tilde{\kappa} L}{2\pi} \right), \qquad \kappa_0 = -\bar{\kappa}, \tag{4.45}$$

and

$$\xi_1 = -\frac{3}{8} k_1 + \frac{k_1 \bar{\beta}}{\kappa_1^2} \tag{4.46}$$

with

$$k_1 = \bar{k} J_1 \left(\frac{\tilde{\kappa} L}{2\pi} \right), \qquad \kappa_1 = \frac{2\pi\epsilon}{L}. \tag{4.47}$$

When the toroidal correction vanishes, i.e., $\tilde{\kappa} = 0$, eq.(4.44) is reduced to the shift in the straight helical configuration with $k_0 = \bar{k}$, and eq.(4.46) disappears because $k_1 = 0$. This means that the toroidal shift proportional to β is caused by both the toroidal effect on the torsion, $\tilde{\kappa}$, and the averaged curvature $\bar{k}$.

In Fig.4.4 we plot the results given by the expressions (4.44) and (4.46) versus the beta value with the shifts obtained numerically. It is considered that the agreement is reasonable. It is noticed that the toroidal shift is roughly comparable to the helical shift.

Since we have obtained the expression for the shift of the plasma column, we can also estimate the magnetic well by following the Solov'ev-Shafranov theory. Substituting (4.43) into the (4.36), the specific volume is expressed by,

$$V'(\Phi) = \frac{1}{B_{\eta 0}} \int_0^L \left[1 - k\rho_0 \left\{ \left(2\frac{\xi_0}{\rho_0} + \frac{d\xi_0}{d\rho_0} \right) + \left(2\frac{\xi_1}{\rho_0} + \frac{d\xi_1}{d\rho_0} \right) \cos\frac{2\pi\eta}{L} \right\} - \frac{1}{2}k^2\rho_0^2 \right] d\eta. \tag{4.48}$$

Using (4.44), (4.46) and (4.38), eq.(4.48) becomes

$$V'(\Phi) = \frac{L}{B_{\eta 0}} \left[1 + \frac{\Phi}{\pi B_{\eta 0}} \left(k_0^2 - 6\frac{k_0^2}{\kappa_0^2}\bar{\beta} \right) \right], \tag{4.49}$$

where $\Phi = \pi\rho_0^2 B_{\eta 0}$ has been used. The specific volume (4.49) shows that, when $\bar{\beta} > \kappa_0^2/6$, the magnetic hill at $\bar{\beta} = 0$ changes into the well, $V'' < 0$. We compare the relative well $V''(s)/V'(s)$ obtained by the BETA code with that given by using (4.49) in Fig.4.5. Good agreement is seen at $s = 0.3 \sim 0.4$, and for $\bar{\beta} \sim 1\%$, the region near the magnetic axis already has the well,

where $s = \Phi/\pi B_{\eta 0}$. Since we have neglected the higher order terms with respect to ρ_0 in (4.48), $V''(\Phi)$ obtained from (4.49) does not have a radial dependence.

4.6 Conclusion

We studied the three-dimensional, finite beta, MHD equilibria of the spatial axis stellarator similar to the Asperator NP-4 configuration by using the BETA code. We used the numerical results to check the applicability of the analytic expressions given by Solov'ev and Shafranov to the Asperator type device.

The numerical equilibria were obtained under the currentless constraint and the fixed boundary condition, and assumed a pressure distribution such that the pressure falls roughly as the square of the toroidal flux.

First we adjusted input parameters carefully so that the shape of the plasma boundary on the perpendicular plane to the helical magnetic axis becomes circular, which is characterized by the vacuum chamber of the Asperator NP-4. The obtained equilibria showed that a little worse Mercier criterion than that of Heliotron E. In the present spatial axis stellarator the profiles of the rotational transform for low beta equilibria are almost flat. The rotational transform is made by the torsion of the helical magnetic axis, which can be evaluated under the straight helical approximation with sufficient accuracy. The results disagree with those in Ref.[22] which showed $\iota \simeq 0.5$. The difference between our value and that of Ref.[22] can be explained by their use of an asymptotic approximation $\iota = N^2 r_h^2 / 2R_0^2$, rather than $\iota = 1 - [1 + (N r_h / R_0)^2]^{-1/2}$ as in Eqs.(4.14) and (4.18). With this correction, they would have found $\iota = 0.29$, in agreement with our result. Although their expansion techniques can provide an understanding of the

physical behavior of stellarators with nonplanar axes, this difference provides a good warning of the care that must be taken when we apply such formalisms to specific devices. We note that their calculation of the effect of plasma pressure on the transform is qualitatively similar to what we found.

The shift of the magnetic axis can be separated into the helical shift and the toroidal shift. Although the helical shift is usually expected to be much larger than the toroidal one in nonplanar axis stellarators, we find that they are of the same order in Asperator NP-4. A similar result was obtained for a Heliac configuration by Hender and his collaborators[43]. This correction to the toroidal shift, which is larger than expected, results from the toroidal correction of the torsion (see eq.(4B.8)). Both the toroidal shift and the helical shift in the numerical equilibria increase almost linearly according to the increase of beta and they agree fairly well with the analytic expressions, (4.44) and (4.46).

We estimated the depth of the magnetic well based on the shifts of the magnetic axis analytically. As the beta increases, the magnetic hill changes into the magnetic well. In the half radius region the transition also agrees quantitatively with the numerical results by the BETA code. Koniges and Johnson [22] also studied the MHD equilibrium of the Asperator NP-4; however, their interest is in the higher beta values than 10% .

We also studied the effect of the triangularity of the boundary cross section on the MHD equilibrium properties. As the triangularity becomes larger, the shear becomes stronger and the magnetic well region at $\bar{\beta} = 0.0\%$ becomes wider in the Asperator NP-4 like configuration. These properties contribute favorably to the MHD stability.

The comparison between the BETA code and the Solov'ev-Shafranov theory have elucidated usefulness of the analytic expressions, which gives a basis to extend the present study to other spatial axis stellarator such as heliac-type configurations.

4.A Matrix of coordinate transformation

In order to determine the shape of the boundary on the $v = const.$ plane, it is convenient to transform the coordinates on the plane perpendicular to the axis of the chamber to the coordinates on the $v = const.$ plane. In this Appendix, we derive the matrix which represents the coordinate transformation.

In the Asperator NP-4 model the axis of the chamber is given by

$$\begin{cases} r_a(v) &= R_0 + r_h \cos(Nv) \\ z_a(v) &= r_h \sin(Nv). \end{cases} \tag{4A.1}$$

By using the Cartesian coordinates of which z-coordinate is the major axis of the torus, the position of this spatial axis, $\mathbf{r}_a(v) = (x(v), y(v), z(v))$, is expressed by

$$\begin{cases} x(v) &= r_a(v) \cos v \\ y(v) &= r_a(v) \sin v \\ z(v) &= z_a(v). \end{cases} \tag{4A.2}$$

Now, we introduce the local orthogonal coordinates (x_M, y_M, z_M) which have the origin at $v = v_0$ on the axis. And we assume that (x_M, y_M) plane is perpendicular to the axis and z_M-coordinate is along the tangential direction of the axis. Then, the unit vector in the z_M-direction, $\mathbf{e}_{zM}$, is given by

$$\mathbf{e}_{zM} = \left.\frac{d\mathbf{r}}{d\eta}\right|_{v=v_0}, \tag{4A.3}$$

where η is the same as the one in the Mercier coordinates discussed in Sec.4.4. Here we introduce another local Cartesian coordinates (x_B, y_B, z_B) with the

same axis direction as (4A.2) and with the origin on the same point of the (x_M, y_M, z_M) coordinates. Then we consider the transformation from the (x_M, y_M, z_M) coordinates to the (x_B, y_B, z_B) coordinates. Substituting (4A.2) into (4A.3), we obtain the components of $\mathbf{e}_{zM}$ in the (x_B, y_B, z_B) coordinate system, $((\mathbf{e}_{zM})_{xB}, (\mathbf{e}_{zM})_{yB}, (\mathbf{e}_{zM})_{zB})$ as

$$\begin{aligned}
(\mathbf{e}_{zM})_{xB} &= -[r_h N \sin(N v_0) \cos v_0 + r_a(v_0) \sin v_0]/L_{zM}, \\
(\mathbf{e}_{zM})_{yB} &= [-r_h N \sin(N v_0) \sin v_0 + r_a(v_0) \cos v_0]/L_{zM}, \\
(\mathbf{e}_{zM})_{zB} &= r_h N \cos(N v_0)/L_{zM},
\end{aligned} \tag{4A.4}$$

where

$$L_{zM} = [r_h^2 N^2 + r_a(v)^2]^{1/2}. \tag{4A.5}$$

If we adjust the x_M coordinate to the principal normal direction, the unit vector along the x_M-coordinate, $\mathbf{e}_{xM}$, is given by

$$\mathbf{e}_{xM} = \frac{1}{k} \frac{d\mathbf{e}_{zM}}{d\eta}\bigg|_{v=v_0} \tag{4A.6}$$

where k is the curvature of the axis. By substituting (4A.4) into (4A.6), the components $((\mathbf{e}_{xM})_{xB}, (\mathbf{e}_{xM})_{yB}, (\mathbf{e}_{xM})_{zB})$ are given by

$$\begin{aligned}
(\mathbf{e}_{xM})_{xB} &= \frac{1}{kL_{zM}^2} \Bigg[(\mathbf{e}_{zM})_{xB} \frac{dL_{zM}}{dv_0} - r_a \cos v_0 \\
&\quad - r_h N^2 \cos(N v_0) \cos v_0 + 2 r_h N \sin(N v_0) \sin v_0 \Bigg] \\
(\mathbf{e}_{xM})_{yB} &= \frac{1}{kL_{zM}^2} \Bigg[(\mathbf{e}_{zM})_{yB} \frac{dL_{zM}}{dv_0} - r_a \sin v_0 \\
&\quad - r_h N^2 \cos(N v_0) \sin v_0 - 2 r_h N \sin(N v_0) \cos v_0 \Bigg] \\
(\mathbf{e}_{xM})_{zB} &= \frac{1}{kL_{zM}^2} \left[(\mathbf{e}_{zM})_{zB} \frac{dL_{zM}}{dv_0} - r_h N^2 \sin(N v_0) \right],
\end{aligned} \tag{4A.7}$$

where

$$\frac{dL_{zM}}{dv_0} = -r_a N r_h \sin(N v_0)/L_{zM}, \tag{4A.8}$$

$$k(v) = \frac{1}{L_{zM}^2}\left[r_h^2 N^4 + 2r_h^2 N^2 + 2r_h^2 N^2 \sin^2(Nv) + 2r_h R_0 N^2 \cos(Nv) + r_a^2\left(1 - \frac{r_h^2 N^2 \sin^2(Nv)}{L_{zM}^2}\right)\right]^{1/2}. \tag{4A.9}$$

The unit vector in the y_M-direction $\mathbf{e}_{yM}$ is given by

$$\mathbf{e}_{yM} = \mathbf{e}_{zM} \times \mathbf{e}_{xM}. \tag{4A.10}$$

Using (4A.4) and (4A.7), we obtain the final expression for three components of $\mathbf{e}_{yM}$

$$\begin{aligned}
(\mathbf{e}_{yM})_{xB} &= \frac{1}{kL_{zM}^3}\left[r_h^2 N^3 \sin v_0 + r_h^2 N^2 \sin(Nv_0)\cos v_0 \right. \\
&\quad \left. + r_a(v_0) r_h \left\{\cos(Nv_0)\sin v_0 - N^2 \sin(Nv_0)\cos v_0\right\}\right] \\
(\mathbf{e}_{yM})_{yB} &= \frac{1}{kL_{zM}^3}\left[-r_h^2 N^3 \cos v_0 + r_h^2 N^2 \sin(2Nv_0)\sin v_0 \right. \\
&\quad \left. - r_a(v_0) r_h \left\{\cos(Nv_0)\cos v_0 + N^2 \sin(Nv_0)\sin v_0\right\}\right] \\
(\mathbf{e}_{yM})_{zB} &= \frac{1}{kL_{zM}^3}\left[2r_h^2 N^2 \sin^2(Nv_0) + r_a(v_0)^2 + r_a(v_0) r_h N^2 \cos(Nv_0)\right].
\end{aligned} \tag{4A.11}$$

Therefore, by using the matrix T,

$$\mathsf{T} = \begin{pmatrix} \mathbf{e}_{xM} \\ \mathbf{e}_{yM} \\ \mathbf{e}_{zM} \end{pmatrix}, \tag{4A.12}$$

where each unit vector means a row vector, we can transform the coordinates (x_M, y_M, z_M) to the coordinates (x_B, y_B, z_B). It should be noted that, in order

to determine the position on the $v = v_0$ plane, the rotation of the coordinates (x_B, y_B, z_B) by the angle v_0 around the major axis is needed in addition after the transform by the matrix T. Then, we obtain the geometrical curve on the (x_B, y_B) plane transformed from the shape in the (x_M, y_M, z_M) coordinates.

Since T is an orthogonal matrix, T^{-1} can be obtained by transposing it. We used T^{-1} in transforming the shift of the magnetic axis obtained by using the BETA code to the quantities on the plane perpendicular to the spatial axis in Fig.4.4.

4.B Expression for curvature and torsion of the spatial magnetic axis

When the magnetic axis of the spatial axis stellarator is given by (4A.1), Frenet's formula give the expressions of the curvature and the torsion as

$$
\begin{aligned}
k(v) &= \frac{1}{L_{zM}^2}\Bigg\{ r_h^2N^4 + 2r_h^2N^2 + 2r_h^2N^2\sin^2(Nv) + 2r_hR_0N^2\cos(Nv) \\
&\quad + r_a^2\left(1 - \frac{r_h^2N^2\sin^2(Nv)}{L_{zM}^2}\right)\Bigg\}^{1/2} \qquad \text{(4B.1)} \\
\kappa(v) &= \Bigg\{ -\frac{r_h^2}{N}(R_0 - 2r_h\cos(Nv)) + \frac{1}{N^3}\Big[\Big(3r_h^3 \\
&\quad + \frac{r_hL_{zM}^2}{N^2} - R_0r_h\Big)\cos(Nv) + 2R_0r_h^2\cos 2(Nv) - r_h^3\cos^3(Nv)\Big]\Bigg\} \\
&\quad \cdot\Bigg\{ r_h^4 + \frac{1}{N^2}\Bigg[r_h^2R_0^2 + \left(r_h^2 + \frac{L_{zM}^2}{N^2}\right)^2 \\
&\quad + 2r_h\left(R_0r_h^2 - r_h^3 + \frac{R_0L_{zM}^2}{N^2}\right)\cos(Nv) \\
&\quad - r_h^2\left(2r_h^2 + \frac{L_{zM}^2}{N^2}\right)\cos^2(Nv)\Bigg]\Bigg\}^{-1}. \qquad \text{(4B.2)}
\end{aligned}
$$

To obtain more simple expressions we use the small parameter expansion with the ordering,

$$
\begin{aligned}
\varepsilon_R &= \frac{r_h}{R_0} \sim \varepsilon_N = \frac{1}{N} \ll 1 \qquad \text{(4B.3)} \\
I_R &= \frac{R_0}{r_hN} \sim 1. \qquad \text{(4B.4)}
\end{aligned}
$$

These are consistent with parameters of the Asperator NP-4 device as shown in Table 4-1, $\varepsilon_R \simeq \varepsilon_N \simeq 1/8, I_R \simeq 1$. We expand eqs.(4B.1) and (4B.2) and

keep terms up to the first order of ε_N or ε_R. Then, we get

$$k(v) \simeq \bar{k}\left[1+\frac{I_R^3-I_R}{1+I_R^2}\varepsilon_N\cos(Nv)\right] \tag{4B.5}$$

$$\kappa(v) \simeq -\bar{\kappa}\left\{1-\frac{1}{1+I_R^2}\left[2(1+I_R^2)\varepsilon_R+I_R(3+I_R^2)\varepsilon_N\right]\cos(Nv)\right\} \tag{4B.6}$$

with $\bar{k}$ and $\bar{\kappa}$ give by eq.(4.17). Noting that $Nv = 2\pi\eta/L$ and $I_R \simeq 1$, we obtain the following approximate expressions as

$$k(\eta) = \bar{k} \tag{4B.7}$$

$$\kappa(\eta) = -\bar{\kappa}+2\bar{\kappa}(\varepsilon_R+\varepsilon_N)\cos\frac{2\pi\eta}{L} \tag{4B.8}$$

4.C Derivation of Mercier criterion

We derive the Mercier criterion by following Johnson and Greene[47] which is different from the method given by Mercier and Luc[46].

We can write the potential energy in the plasma region in the following way[47]

$$\begin{aligned}\delta W &= \frac{1}{2}\int[\left|\nabla\times(\boldsymbol{\xi}\times\mathbf{B})-\mathbf{B}\frac{\boldsymbol{\xi}\cdot\nabla P}{B^2}\right|^2-\sigma\boldsymbol{\xi}\times\mathbf{B}\cdot\nabla\times(\boldsymbol{\xi}\times\mathbf{B})\\ &\quad -2\boldsymbol{\xi}\cdot\nabla P\boldsymbol{\xi}\cdot\boldsymbol{\kappa}+\Gamma P|\nabla\cdot\boldsymbol{\xi}|^2\,]\,dV, \qquad (4C.1)\end{aligned}$$

where

$$\sigma = \frac{\mathbf{J}\cdot\mathbf{B}}{B^2}, \qquad (4C.2)$$

$$\boldsymbol{\kappa} = \frac{[\mathbf{B}\times\nabla(2P+B^2)]\times\mathbf{B}}{2B^4}. \qquad (4C.3)$$

To describe toroidal plasmas generally, we use the Hamada coordinates (V,θ,ζ) with the Jacobian being unity. Here V denotes flux volume corresponding to the radial coordinate, and θ and ζ are poloidal and toroidal angles, respectively. In this coordinate system the magnetic field $\mathbf{B}$ can be expressed by

$$\mathbf{B}=\nabla V\times\nabla\left[\Phi'(V)\theta-\Psi'(V)\zeta\right], \qquad (4C.4)$$

where Φ and Ψ denote the toroidal and the poloidal flux, respectively, and prime denotes the derivative with respect to V. We assume that the perturbation is localized near the flux surface labeled V_0. When the infinitesimal displacement vector $\boldsymbol{\xi}$ is decomposed with the three local orthogonal vectors

as

$$\boldsymbol{\xi} = \xi \frac{\nabla V}{|\nabla V|} + \mu \frac{\mathbf{B} \times \nabla V}{B^2} + \nu \frac{\mathbf{B}}{B^2}. \tag{4C.5}$$

We introduce a new variable

$$u = \Phi'(V_0)\theta - \Psi'(V_0)\zeta. \tag{4C.6}$$

By using (4C.5) and (4C.6) in (4C.1) we obtain the expression

$$\begin{aligned} \delta W \;=\; & \frac{1}{2}\int \left[\left| \frac{\nabla V}{|\nabla V|^2}\mathbf{B}\cdot\nabla\xi + \frac{\mathbf{B}\times\nabla V}{B^2}\left\{\mathbf{B}\cdot\nabla\mu + (\mathbf{B}\cdot\nabla\Theta - \Lambda)\xi\right\} \right.\right. \\ & \left. + \mathbf{B}\left\{ \mathbf{B}\cdot\nabla\left(\frac{\nu}{B^2}\right) - \xi\frac{\nabla V\cdot\nabla(2P+B^2)}{B^2|\nabla V|^2} - \frac{\mu}{P'}\mathbf{B}\cdot\nabla\sigma - \nabla\cdot\boldsymbol{\xi}\right\}\right|^2 \\ & -\sigma\mu\mathbf{B}\cdot\nabla\xi + \sigma\xi\left\{(\mathbf{B}\cdot\nabla\mu) - \xi(\Lambda - \mathbf{B}\cdot\nabla\Theta)\right\} \\ & \left. - \xi^2\frac{\nabla P\cdot\nabla(2P+B^2)}{B^2|\nabla V|^2} - \mu\xi\mathbf{B}\cdot\nabla\sigma + \Gamma P(\nabla\cdot\boldsymbol{\xi})^2 \right] dV, \end{aligned} \tag{4C.7}$$

where

$$\Theta \;=\; \frac{\nabla V\cdot\nabla u}{|\nabla V|^2}, \tag{4C.8}$$

$$\Lambda \;=\; \Phi'(V_0)\Psi''(V_0) - \Psi'(V_0)\Phi''(V_0). \tag{4C.9}$$

Here we use x instead of V,

$$x \equiv (V - V_0)/\varepsilon, \tag{4C.10}$$

where ε is a small quantity to measure the localization of the radial displacement. We impose the following condition

$$|\boldsymbol{\xi}| \to 0 \quad \text{as} \quad |x| \to 1. \tag{4C.11}$$

We expand the components of the displacement vector in the neighborhood of the rational surface in the power series with respect to ε,

$$\begin{cases} \xi &= \xi^{(0)} + \varepsilon\xi^{(1)} + \varepsilon^2\xi^{(2)} + \cdots \\ \mu &= \mu^{(0)} + \varepsilon\mu^{(1)} + \cdots \\ \nu &= \nu^{(0)} + \varepsilon\nu^{(1)} + \cdots . \end{cases} \tag{4C.12}$$

The operator $\mathbf{B}\cdot\nabla$ is also expanded as

$$\mathbf{B}\cdot\nabla\alpha = \Phi'^{(0)}\frac{\partial\alpha}{\partial\zeta} + \varepsilon x\left(\Phi'^{(0)}\frac{\partial\alpha}{\partial\zeta} + \Lambda\frac{\partial\alpha}{\partial u}\right) + \cdots \tag{4C.13}$$

for an arbitrary scalar function α. Hereafter it is convenient to use the coordinates (V, u, ζ) instead of the Hamada coordinates.

With these expansions we can write eq.(4C.7) in power of ε by noting that $\partial/\partial V = \varepsilon^{-1}\partial/\partial x$ and $dV = \varepsilon dx du d\zeta$. The lowest order of δW is the ε^{-1} order

$$\delta W^{(-1)} = \frac{1}{2}\int_{-1}^{1}\left[\left|\mathbf{B}^{(0)}\frac{\partial\xi^{(0)}}{\partial x}\right|^2 + \Gamma P^{(0)}\left(\frac{\partial\xi^{(0)}}{\partial x}\right)^2\right]dx \tag{4C.14}$$

where $\mathbf{B}^{(0)}$ and $P^{(0)}$ denote quantities of order ε^0. This gives a positive contribution and vanishes only if

$$\frac{\partial\xi^{(0)}}{\partial x} = 0. \tag{4C.15}$$

By using the condition (4C.11), (4C.15) means $\xi^{(0)} = 0$.

The next significant contribution comes from the order ε^1 which is expressed by

$$\delta W^{(1)} = \frac{1}{2}\int[\left|\frac{\mathbf{B}^{(0)}\times\nabla V}{|\mathbf{B}^{(0)}|^2}\Phi'^{(0)}\frac{\partial\mu^{(0)}}{\partial\zeta}\right.$$
$$\left.+\mathbf{B}^{(0)}\left\{\Phi'^{(0)}\frac{\partial}{\partial\zeta}\left(\frac{\nu}{B^2}\right)^{(0)}-\frac{\mu^{(0)}}{P'^{(0)}}\Phi'^{(0)}\frac{\partial\sigma^{(0)}}{\partial\zeta}-(\nabla\cdot\boldsymbol{\xi})^{(0)}\right\}\right|^2$$
$$+\Gamma P^{(0)}\left((\nabla\cdot\boldsymbol{\xi})^{(0)}\right)^2]\,dxd\theta d\zeta, \tag{4C.16}$$

where $\sigma^{(0)}, \Phi^{(0)}, \nu^{(0)}, \mu^{(0)}$, and $(\nabla\cdot\xi)^{(0)}$ denote the quantity of order ε^0. This order is also positive definite. If we choose the perturbations as

$$\mu^{(0)} = \mu^{(0)}(x,u) \tag{4C.17}$$

$$(\nabla\cdot\boldsymbol{\xi})^{(0)} = 0, \tag{4C.18}$$

$$\frac{\partial}{\partial\zeta}\left(\frac{\nu}{\mathbf{B}^2}\right)^{(0)}-\frac{\mu^{(0)}}{P'^{(0)}}\frac{\partial\sigma^{(0)}}{\partial\zeta}=0, \tag{4C.19}$$

$\delta W^{(1)}$ vanishes again. It is noted that eqs.(4C.18) and (4C.19) leads the condition

$$\frac{\partial\xi^{(1)}}{\partial x}+\frac{\partial\mu^{(0)}}{\partial u}=0. \tag{4C.20}$$

Differentiating (4C.20) by ζ and using the conditions (4C.11) and (4C.17) we obtain

$$\frac{\partial\xi^{(1)}}{\partial\zeta}=0. \tag{4C.21}$$

The lowest order of δW with nonzero contribution is the order ε^3 and is given by

$$
\begin{aligned}
\delta W^{(3)} &= \frac{1}{2}\int[\left|\frac{\mathbf{B}^{(0)}\times\nabla V}{|B^{(0)}|^2}\{\mathbf{B}\cdot\nabla\mu+(\mathbf{B}\cdot\nabla\Theta-\Lambda)\xi\}^{(1)}\right.\\
&+ \left.\mathbf{B}^{(0)}\left\{\mathbf{B}\cdot\nabla\left(\frac{\nu}{B^2}\right)-\nabla\cdot\boldsymbol{\xi}-\xi\frac{\nabla V\cdot\nabla(2P+B^2)}{B^2|\nabla V|^2}-\frac{\mu}{P'}\mathbf{B}\cdot\nabla\sigma\right\}^{(1)}\right|^2\\
&- \mu^{(0)}\sigma^{(0)}(\mathbf{B}\cdot\nabla\xi)^{(2)}+\xi^{(1)}\sigma^{(0)}\{\mathbf{B}\cdot\nabla\mu-\xi(\Lambda-\mathbf{B}\cdot\nabla\Theta)\}^{(1)}\\
&- \xi^{(1)2}\left(\frac{\nabla P\cdot\nabla(2P+B^2)}{B^2|\nabla V|^2}\right)^{(0)}-\mu^{(0)}(\xi\mathbf{B}\cdot\nabla\sigma)^{(2)}-\mu^{(1)}(\xi\mathbf{B}\cdot\nabla\sigma)^{(1)}\\
&+ \Gamma P^{(0)}\left((\nabla\cdot\boldsymbol{\xi})^{(1)}\right)^2]\,dxd\theta d\zeta. \qquad (4C.22)
\end{aligned}
$$

Since ν is included only in the second term which contributes to positive, we choose ν so that this term should vanish. In order to eliminate the positive last term, we can set

$$(\nabla\cdot\boldsymbol{\xi})^{(1)}=0. \qquad (4C.23)$$

By performing integration of the terms including the ζ-derivative and using and (4C.20) and (4C.21) , we find

$$
\begin{aligned}
\delta W^{(3)} &= \frac{1}{2}\int\left[\frac{|\nabla V|^2}{B^2}\left\{G-\Lambda\frac{\partial}{\partial x}(x\xi^{(1)})+\frac{B^2}{|\nabla V|^2}\sigma\xi^{(1)}\right\}^2\right.\\
&\left.+\xi^{(1)2}\left\{-\frac{\sigma^2B^2}{|\nabla V|^2}+\sigma(-\Phi_0'\frac{\partial\Theta}{\partial\zeta}+\Lambda)-\frac{\nabla V\cdot\nabla(2P+B^2)}{B^2|\nabla V|^2}\right\}\right]dx, \qquad (4C.24)
\end{aligned}
$$

where

$$
\begin{aligned}
G &= \Phi'^{(0)}\frac{\partial}{\partial\zeta}(\mu^{(1)}+\Theta\xi^{(1)})\\
&= (\mathbf{B}\cdot\nabla)^{(0)}(\mu^{(1)}+\Theta\xi^{(1)}). \qquad (4C.25)
\end{aligned}
$$

Hereafter the superscript (0) have been dropped for simplicity. In the magnetic differential equation (4C.25) with single-valued $\mu^{(1)}$ and $\xi^{(1)}$, Newcomb's theorem requires that G must satisfy the condition,

$$\oint \frac{G}{B} d\ell = 0. \tag{4C.26}$$

Then we minimize eq.(4C.24) under the constraint (4C.26). By the Lagrange multiplier method we obtain the relation

$$G_0 = \Lambda \left(1 - \frac{B^2 \oint \frac{d\ell}{B}}{|\nabla V|^2 \oint \frac{B^2}{|\nabla V|^2} \frac{d\ell}{B}} \right) \frac{\partial}{\partial x}(x\xi^{(1)}) - \frac{B^2}{|\nabla V|^2} \left(\sigma - \frac{\oint \frac{\sigma B^2}{|\nabla V|^2} \frac{d\ell}{B}}{\oint \frac{B^2}{|\nabla V|^2} \frac{d\ell}{B}} \right) \xi^{(1)} \tag{4C.27}$$

to minimize $\delta W^{(3)}$. After substituting eq.(4C.27) to (4C.24), we integrate the first term in eq.(4C.24) by parts and apply Schwartz's inequality

$$\int_{-1}^{1} \left\{ \frac{\partial}{\partial x}(x\xi^{(1)}) \right\}^2 dx \geq \frac{1}{4} \int_{-1}^{1} (\xi^{(1)})^2 dx, \tag{4C.28}$$

to the integral. Here we have imposed the condition (4C.11) on the upper and lower limit of the integral. By noting that the equilibrium quantities in eq.(4C.24) are the values at the surface labeled with V_0, $\delta W^{(3)}$ is expressed by

$$2\delta W^{(3)} = \frac{F \int_{-1}^{1} (\xi^{(1)})^2 dx}{\oint \frac{B^2}{|\nabla V|^2} \frac{d\ell}{B}}, \tag{4C.29}$$

where

$$\begin{aligned} F &= \frac{\Lambda^2}{4} \left(\oint \frac{d\ell}{B} \right)^2 - \Lambda \oint \frac{d\ell}{B} \oint \frac{\sigma B^2}{|\nabla V|^2} \frac{d\ell}{B} + \left(\oint \frac{\sigma B^2}{|\nabla V|^2} \frac{d\ell}{B} \right)^2 \\ &- \oint \frac{\sigma^2 B^2}{|\nabla V|^2} \frac{d\ell}{B} \oint \frac{B^2}{|\nabla V|^2} \frac{d\ell}{B} + \oint K \frac{d\ell}{B} \oint \frac{B^2}{|\nabla V|^2} \frac{d\ell}{B} \end{aligned} \tag{4C.30}$$

$$
\begin{aligned}
K &\equiv -\frac{\nabla P\cdot\nabla(2P+B^2)}{B^2}+\frac{\sigma(\mathbf{B}\times\nabla V)\cdot\nabla\times(\mathbf{B}\times\nabla V)}{|\nabla V|^2} \\
&= -\frac{(P')^2|\nabla V|^2}{B^2}-|\nabla V|^2(J'\Phi''-I'\Psi'') \\
&\quad -|\nabla V|^2\mathbf{B}\cdot\nabla\left(\frac{I'\nabla V\cdot\nabla\theta-J'\nabla V\cdot\nabla\theta}{|\nabla V|^2}\right). \qquad \text{(4C.31)}
\end{aligned}
$$

In eq.(4C.31) we have introduced current fluxes I and J as

$$
\mathbf{J} = \nabla V\times[I'\nabla\theta-J'\nabla\zeta] \qquad \text{(4C.32)}
$$

$$
P' = J'\Phi'-I'\Psi'. \qquad \text{(4C.33)}
$$

If we change the label on the flux surface from the flux volume V to the toroidal flux Φ and use the prime to mean the derivative with respect to Φ in eqs.(4C.30) and (4C.31), we obtain

$$
\begin{aligned}
F &= \frac{1}{4}\left(\frac{\Lambda}{V'^3}\oint\frac{d\ell}{B^2}\right)^2+\left(\frac{1}{V'^2}\oint\frac{\sigma B^2}{|\nabla\Phi|^2}\frac{d\ell}{B}\right)^2-\frac{1}{V'^4}\oint\frac{\sigma^2B^2}{|\nabla\Phi|^2}\frac{d\ell}{B}\oint\frac{B^2}{|\nabla\Phi|^2}\frac{d\ell}{B} \\
&\quad -\oint\frac{\sigma^2B^2}{V'^2|\nabla\Phi|^2}\frac{d\ell}{B}\oint\frac{B^2}{V'^2|\nabla\Phi|^2}\frac{d\ell}{B}-\oint\frac{P'^2}{B^2V'^2}\frac{d\ell}{B}\oint\frac{B^2}{V'^2|\nabla\Phi|^2}\frac{d\ell}{B}+\frac{L}{V'^6}
\end{aligned}
\qquad \text{(4C.34)}
$$

where

$$
\begin{aligned}
L &= -\Lambda V'\oint\frac{d\ell}{B}\frac{\sigma B^2}{|\nabla\Phi|^2}\frac{d\ell}{B}+V'\oint(I'\Psi''+P'V'')\frac{d\ell}{B}\oint\frac{B^2}{|\nabla\Phi|^2}\frac{d\ell}{B} \\
&= V'\oint\frac{d\ell}{B}\oint\{P'V''+(I'-\sigma\Phi')\Psi''\}\frac{B^2}{|\nabla\Phi|^2}\frac{d\ell^2}{B}. \qquad \text{(4C.35)}
\end{aligned}
$$

Since positive $\delta W^{(3)}$ by eq.(4C.29) corresponds to stability against the localized mode in the neighborhood of $V=V_0$, the stability criterion is given

from (4C.29),

$$\begin{aligned}
\Omega &\equiv V'^6 F \\
&= \frac{\Lambda^2}{4}\left(\oint \frac{d\ell}{B}\right)^2 + V' \oint \frac{d\ell}{B} \oint \frac{(I' - \sigma\Phi')\Psi'' B^2}{|\nabla\Phi|^2} \frac{d\ell}{B} \\
&+ V' \oint \frac{d\ell}{B} \oint P'V'' \frac{B^2}{|\nabla\Phi|^2} \frac{d\ell}{B} - (P'V')^2 \oint \frac{1}{B^2} \frac{d\ell}{B} \oint \frac{B^2}{|\nabla\Phi|^2} \frac{d\ell}{B} \\
&+ V'^2 \left[\left(\oint \frac{\sigma B^2}{|\nabla\Phi|^2} \frac{d\ell}{B} \right)^2 - \oint \frac{\sigma^2 B^2}{|\nabla\Phi|^2} \frac{d\ell}{B} \oint \frac{B^2}{|\nabla\Phi|^2} \frac{d\ell}{B} \right] > 0.
\end{aligned} \tag{4C.36}$$

By employing the (s, u, v) coordinates used in the BETA code and noting that

$$\Lambda = \iota', \quad \oint \frac{d\ell}{B} = \int D_p du dv, \tag{4C.37}$$

we obtain the expressions in (4.4) $\sim$ (4.8).

Table 4-1 Asperator NP-4 Parameters

Average major radius, aR_0 (cm)	152.4
Limiter radius, a (cm)	9.5
Number of periods, N	8
Helical radius, ar_h (cm)	19.05

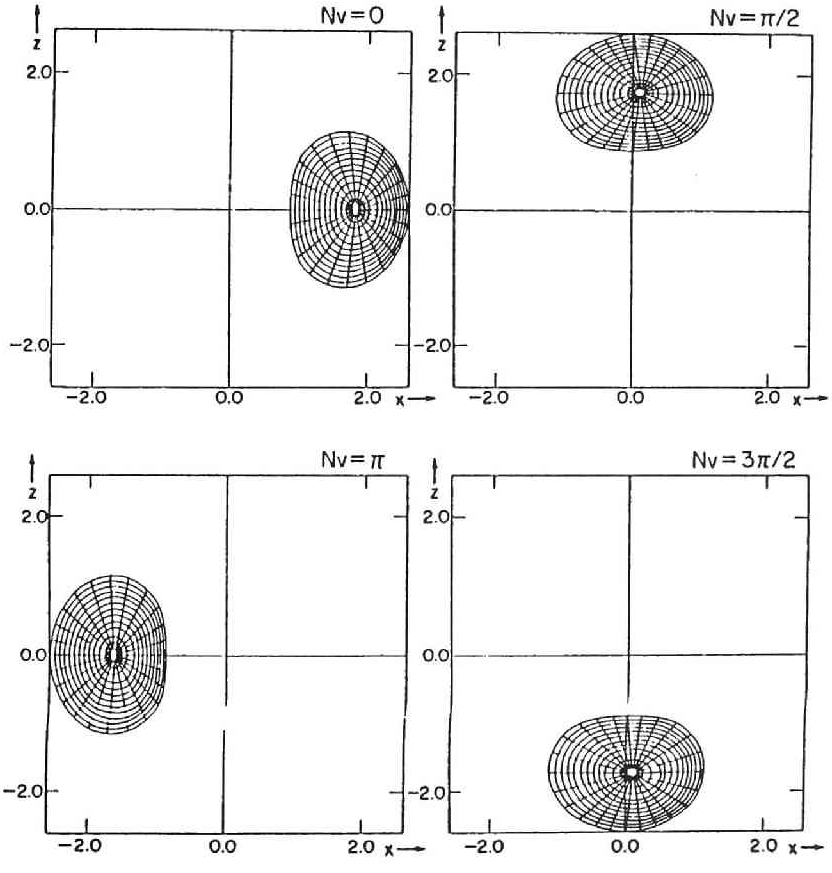

Fig.4.1 Flux surfaces of Asperator NP-4 equilibrium with $\bar{\beta} = 4.4\%$, obtained by the BETA code at four cross-sections.

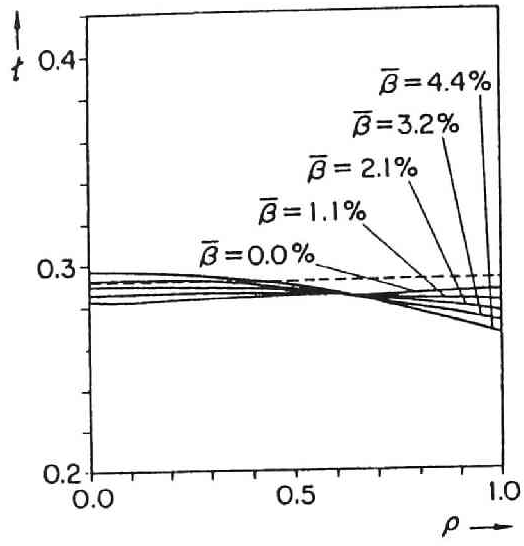

Fig.4.2 Profiles of rotational transform of Asperator NP-4 equilibrium for several beta values obtained numerically (solid line) and analytic values at magnetic axis (dashed line).

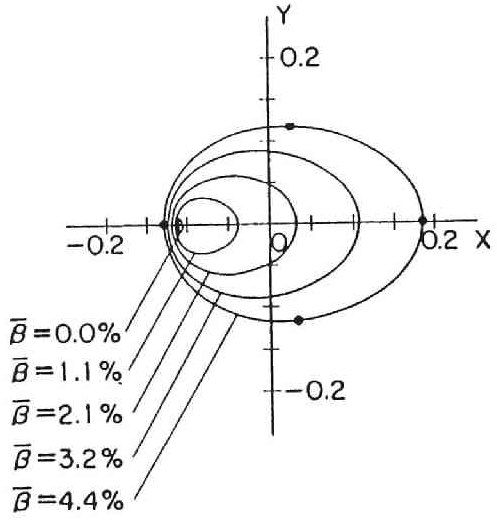

Fig.4.3 Motion of magnetic axis on $\eta = const.$ plane (see (4.10)) over one period for several beta values. The four black circles correspond to the four cross sections in Fig.4.1. X and Y axes indicate the principal normal and binormal directions of the helical magnetic axis, respectively.

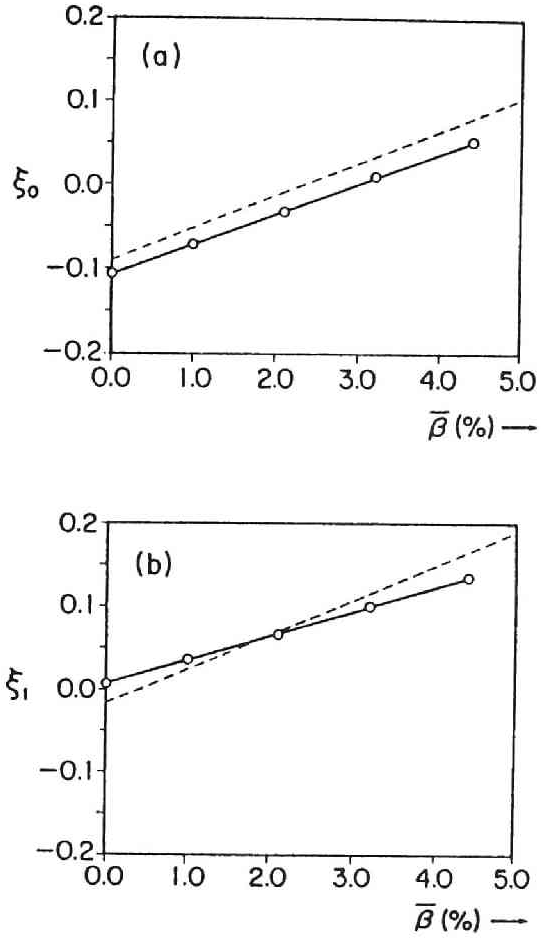

Fig.4.4 (a)Helical and (b) toroidal shift of magnetic axis. Solid lines correspond to numerical calculation; dashed lines correspond to analytic expressions.

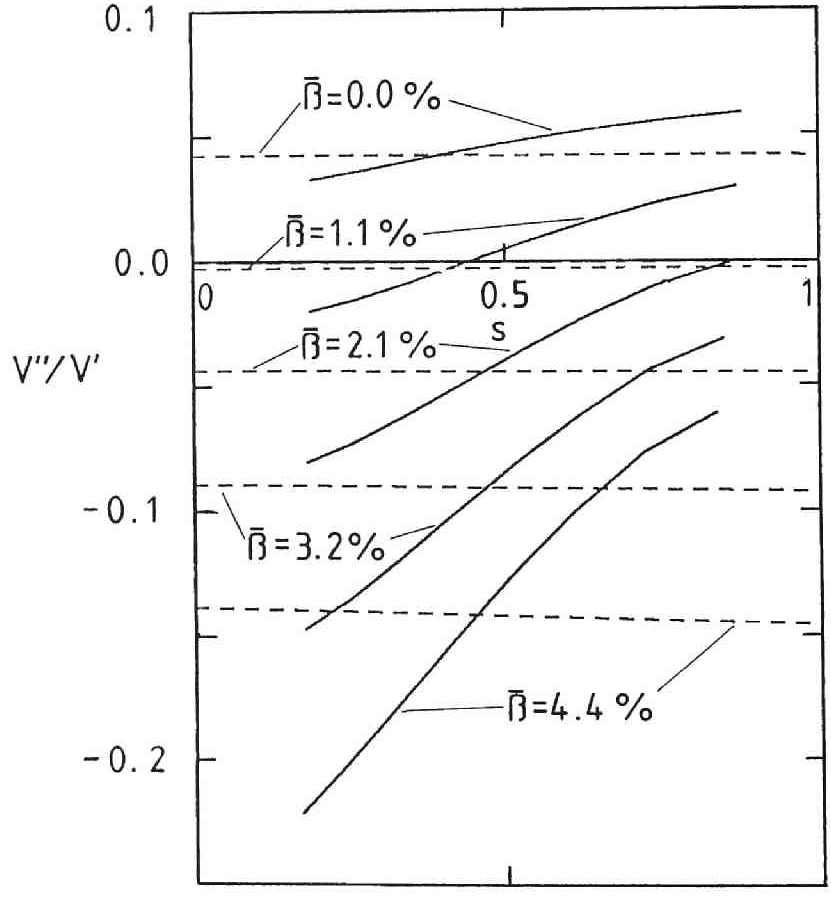

Fig.4.5 Relative magnetic well ($V''(s)/V'(s)$) for several beta values. Solid lines correspond to numerical calculations; dashed lines are given by analytic expression.

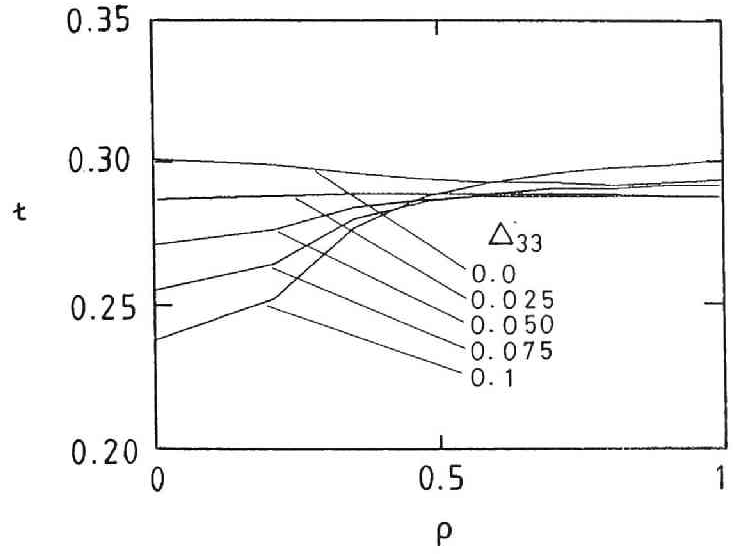

Fig.4.6 Profiles of rotational transform with $\bar{\beta} \simeq 0\%$ for several triangular coefficients, Δ_{33}, at $\Delta_{22} = -0.15$.

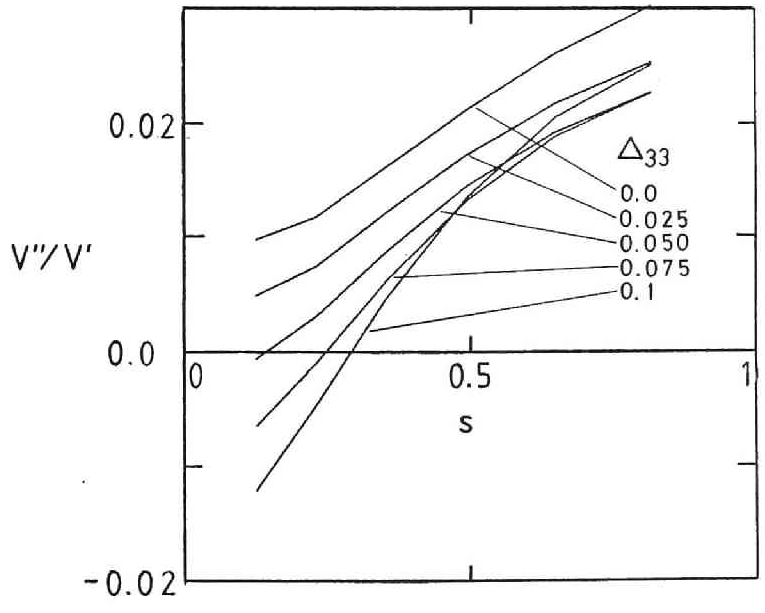

Fig.4.7 Relative magnetic well with $\bar{\beta} \simeq 0\%$ for several triangular coefficients, Δ_{33}, at $\Delta_{22} = -0.15$.

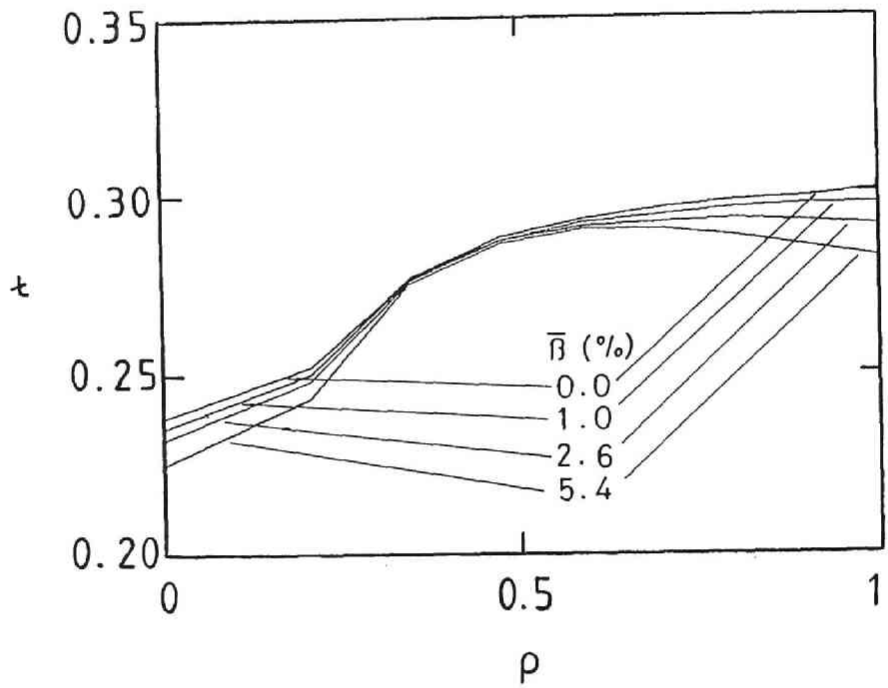

Fig.4.8 Profiles of rotational transform of equilibria with $\Delta_{22} = -0.15$ and $\Delta_{33} = 0.1$ for several beta values.

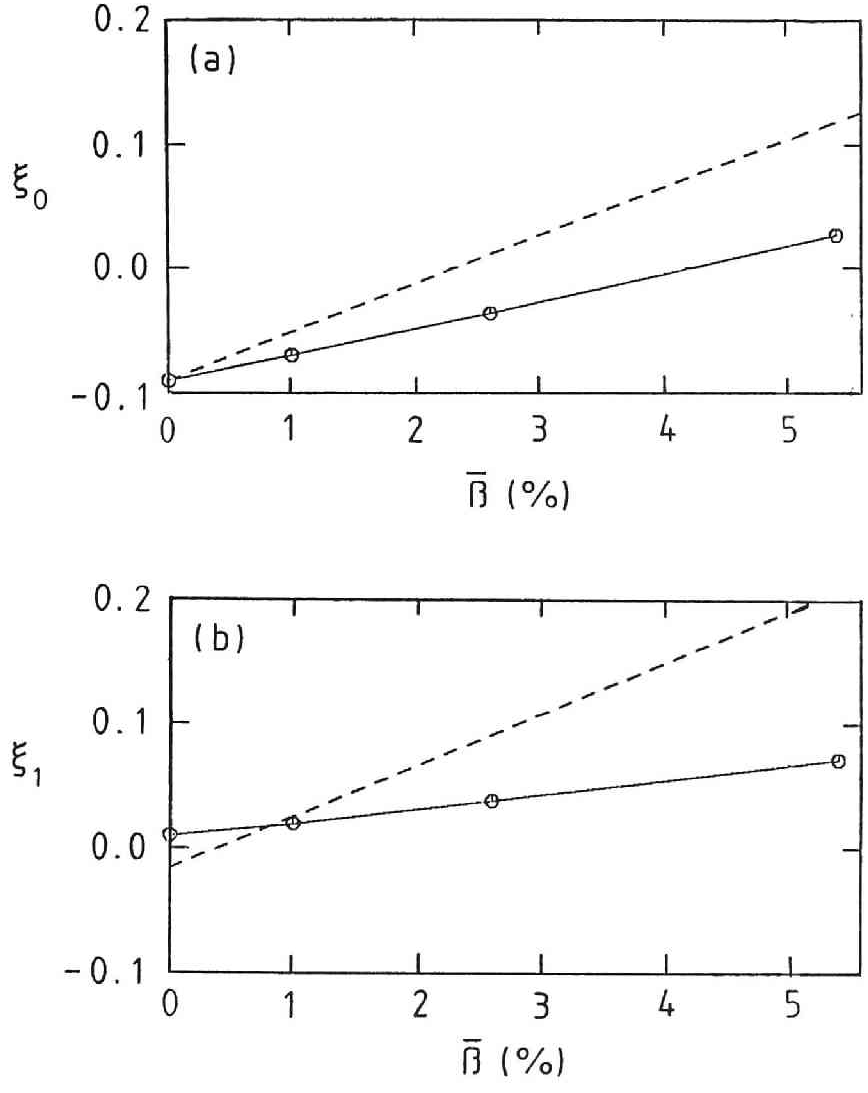

Fig.4.9 (a)Helical and (b) toroidal shift of magnetic axis. Solid lines correspond to numerical calculation for equilibria with $\Delta_{22} = -0.15$ and $\Delta_{33} = 0.1$; dashed lines correspond to analytic expressions for Asperator NP-4 equilibria with circular cross section.

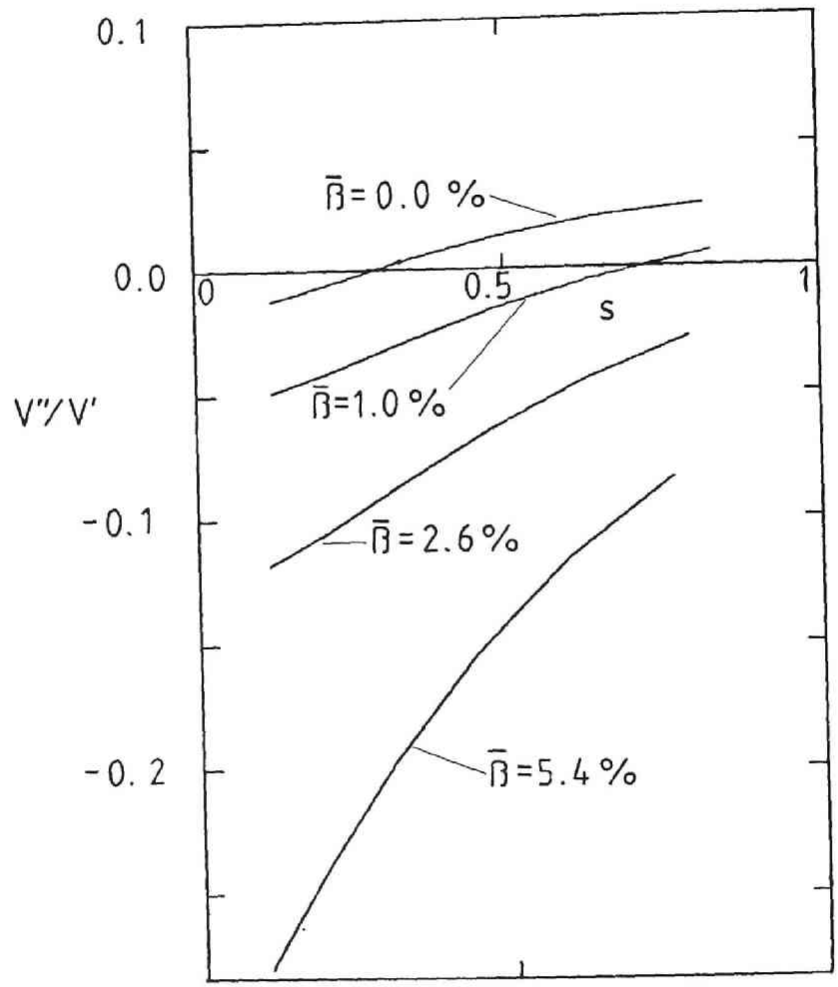

Fig.4.10 Radial dependence of relative magnetic well for equilibria with $\Delta_{22} = -0.15$ and $\Delta_{33} = 0.1$ for several beta values.

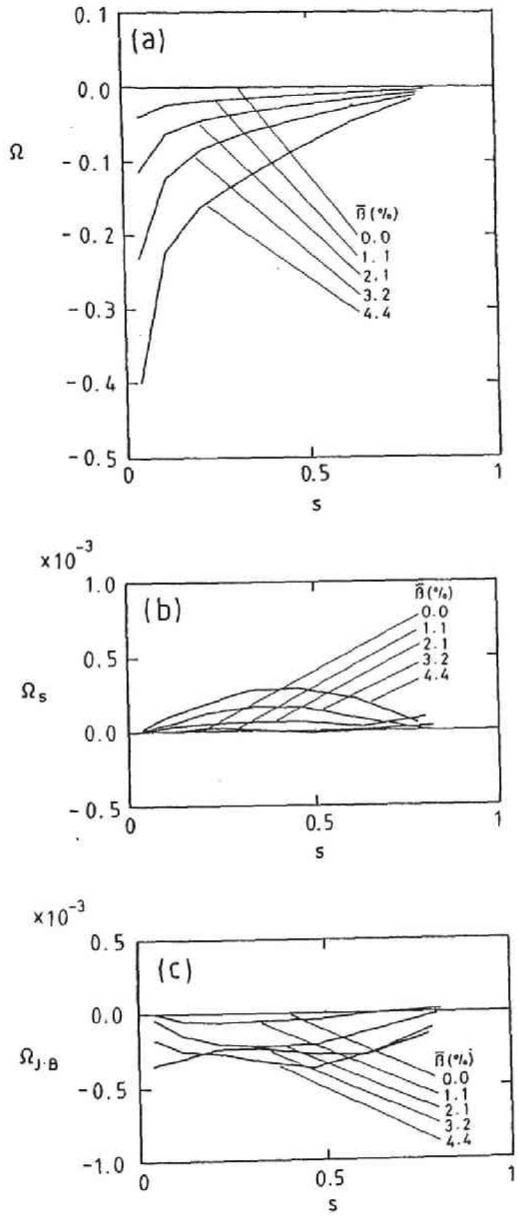

Fig.4.11 Mercier criterion of Asperator NP-4 at $\bar{\beta} = 0.0\%$, 1.0%, 2.1%, 3.2% and 4.4%; (a) Ω, (b) Ω_s, (c) $\Omega_{J\cdot B}$, (d) Ω_W and (e) $\Omega_{P.S.}$.

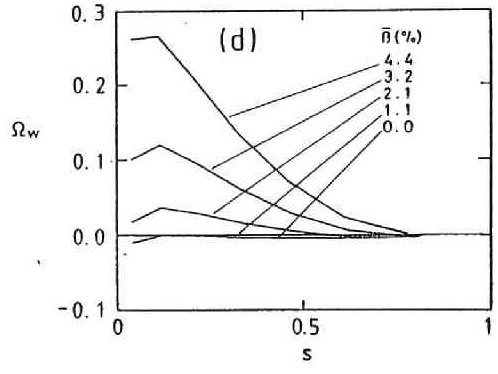
(d)
$\bar{\beta}$(%)
4.4
3.2
2.1
1.1
0.0
Ω_w
0.3
0.2
0.1
0.0
-0.1
0
0.5
1
s

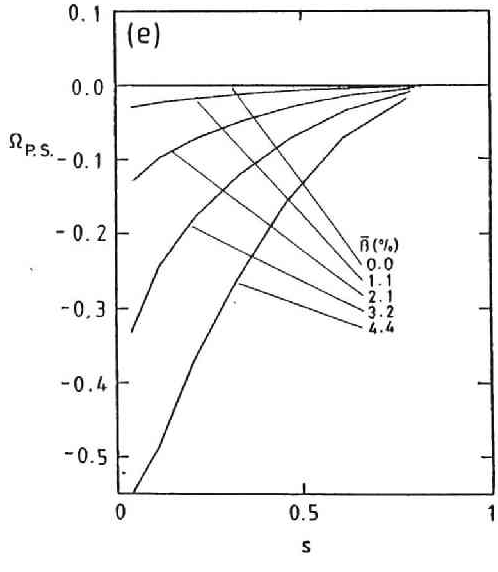
(e)
$\Omega_{P.S.}$
0.1
0.0
-0.1
-0.2
-0.3
-0.4
-0.5
$\bar{\beta}$(%)
0.0
1.1
2.1
3.2
4.4
0
0.5
1
s

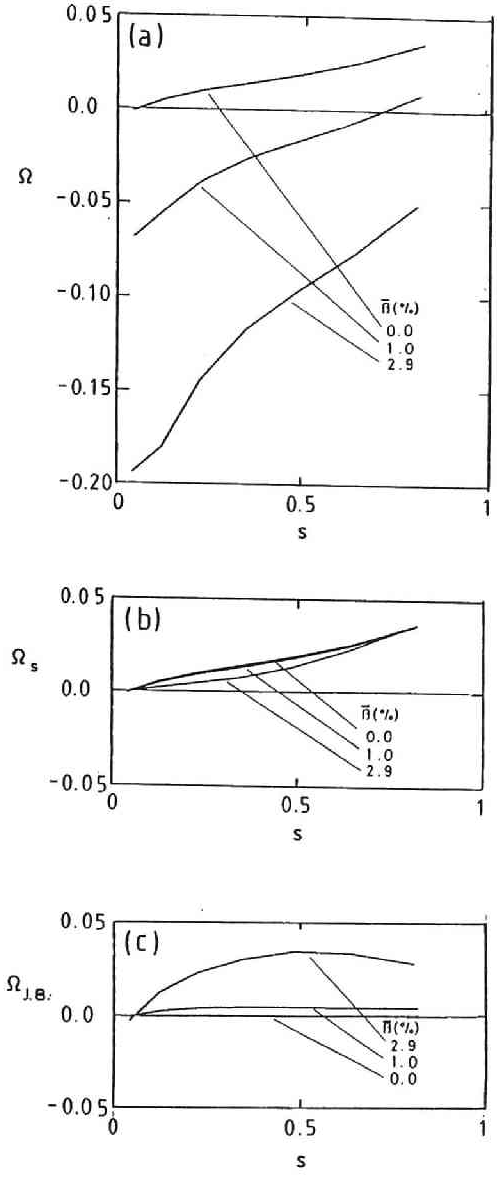

Fig.4.12 Mercier criterion of Heliotron E model with $A = 11$, $\Delta_2 = 0.26$, $N = 19$ and pressure profile $P = P_0(1 - \rho^2)$ at $\bar{\beta} = 0.0\%$, 1.0% and 2.9%; (a) Ω, (b) Ω_s, (c) $\Omega_{J.B}$, (d) Ω_W and (e) $\Omega_{P.S.}$.

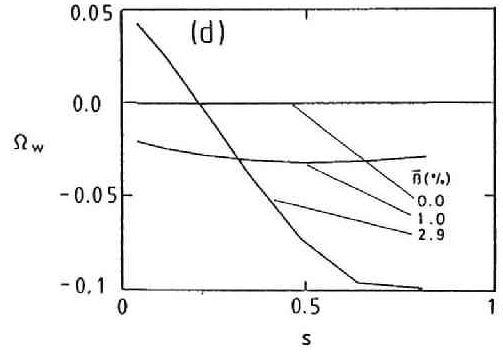
(d)
0.05
0.0
-0.05
-0.1
Ω_w
0
0.5
1
s
$\bar{n}$(%)
0.0
1.0
2.9

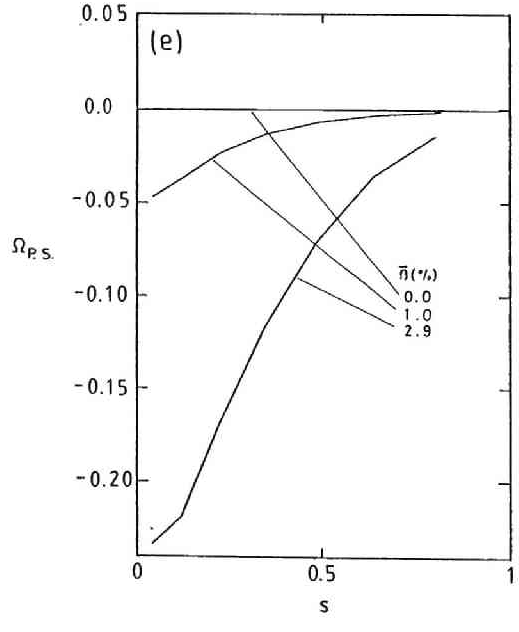
(e)
0.05
0.0
-0.05
-0.10
-0.15
-0.20
$\Omega_{P.S.}$
0
0.5
1
s
$\bar{n}$(%)
0.0
1.0
2.9

Chapter 5

Reduced MHD Equations for Resistive Modes in Stellarator/Heliotron Configurations

5.1 Introduction

For MHD instabilities, we usually consider two types of normal modes from characteristics of the eigenfunction; one is the localized mode in the neighborhood of the mode rational surface (or the resonant surface) and the other is the global mode with a broad mode structure inside the plasma column. For the former case, we usually use the Mercier criterion. The

second minimization of the potential energy is implemented in the BETA code for the latter case. The BETA code can obtain three-dimensional MHD equilibria, examine the Mercier criterion and calculate growth rates of global modes. Particularly, as discussed in Chapter 4, it is very useful for calculating the MHD equilibria and the stability of spatial axis stellarators which seem to be complicated compared to heliotron/torsatron configurations.

A different approach for the analysis of global modes employs the reduced MHD equations. As mentioned in Chapter 1, the reduced MHD approach has been proposed for the study of equilibrium and stability in stellarator configurations[24,25], which is essentially equivalent to the stellarator expansion method[6]. The MHD equilibrium equation obtained from the reduced MHD equations is two dimensional, since only the averaged quantities over the helical period along the toroidal direction are retained in the lowest order. Hence this method has the advantage of exploiting the numerical techniques developed to study tokamak equilibrium and stability. The STEP code [10,11] is one of the numerical codes for studying the ideal MHD equilibrium and stability based on the stellarator expansion method, which is composed of 'Equilibrium', 'Mapping' and 'Stability' parts. It is useful to obtain an currentless finite beta equilibrium and to examine its stability against both global and localized modes in heliotron/torsatron configurations with a reasonable computation time.

It is crucial to study the resistive effects on the MHD stability in the heliotron configurations, because present heliotron plasmas have finite resistivity in the sheared magnetic field belong to the magnetic hill. In this situation the resistivity excites new instabilities called resistive modes. The linear

instabilities of the resistive interchange, tearing and rippling modes were studied intensively in the slab geometry by Furth, Kileen and Rosenbluth [5], where they divided the plasma region into the inner resistive layer and the outer ideal region and found the growth rates by matching the solution in the inner region to that in the outer region asymptotically. Glasser, Greene and Johnson [49] extended this matching procedure to the axisymmetric toroidal configuration and obtained a stability condition called GGJ criterion for the localized resistive interchange and tearing modes. Recently this criterion is extended to the stellarator configuration based on the stellarator expansion including higher order terms [15]. Analysis of the global resistive mode requires to solve the eigenvalue problem composed of the fourth order or sixth order differential equation, and usually the numerical calculation is inevitable.

In Heliotron E and Heliotron DR soft X ray measurement showed the behaviors similar to internal disruptions in tokamaks. In these configurations global resistive interchange modes become a candidate to explain the macroscopic fluctuations, instead of tearing modes, since currentless finite beta plasmas were produced in these devices. Thus, we have developed a code (RESORM code) [50] to study the resistive linear stability for equilibria obtained by using the 'Equilibrium' part of the STEP code[15], which makes the RESORM code include more realistic magnetic configurations of Heliotron E and Heliotron DR than those in the previous studies [6]. We employ the modified stellarator ordering including the higher order toroidal corrections, which is consistent with the modified version of the 'Equilibrium' part of the STEP code [15]. These corrections become important for

the small aspect ratio devices [54]. In the RESORM code, the growth rate and the eigenfunction are determined by following the time evolution of the perturbation as the initial value problem based on the reduced MHD equations for stellarators. In the previous codes of the initial value problem type [51,52,53], the quasi-toroidal coordinates were used and only the lowest order toroidal corrections were kept or the cylindrical configuration was assumed for simplicity. Here we employ the flux coordinates with which it is straightforward to include toroidal effects from the 'Equilibrium' result of the STEP code. This is essentially the same technique as that in the FAR code developed at Oak Ridge National Laboratory[26]. It is remarked that this type of stability code has an advantage that both the resistive and ideal modes can be studied by selecting finite resistivity or zero resistivity as an input parameter.

In Sec.5.2, we explain the stellarator ordering including higher order correction. The stellarator ordering leads to three field equations, and, two of them have the form of the magnetic differential equation including different order terms. However, we obtain the reduced MHD equations composed of uniformly ordered quantities by applying the averaging method to the above three field equations as explained in Sec.5.3. We also discuss the equilibrium equation derived from the reduced equations and the 'Equilibrium' part of the STEP code in Sec5.4. In Sec.5.5, we introduce the flux coordinates which is similar to the PEST coordinates, and linearize the reduced MHD equations. In Sec.5.6, the numerical scheme employed in the RESORM code is discussed. We explain the 'Stability' part of the STEP code briefly in Sec.5.7. In Sec.5.8, the approach using the reduced MHD equations and the

RESORM code are discussed.

5.2 Ordering to derive the reduced MHD equations

The reduced MHD equations for heliotron/torsatron were originally derived based on the stellarator ordering under the assumption of large aspect ratio[24]. Although we follow the same principle, we consider higher order terms of toroidal corrections than those in Ref.[24] in order to investigate heliotron/torsatron with a small aspect ratio similar to ATF. The magnetic field in the heliotron/torsatron configuration is assumed to be

$$\mathbf{B} = B_0 R_0 \nabla\zeta + \delta \mathbf{B}_\delta + \delta^2 \nabla \times \mathbf{A}. \tag{5.1}$$

Here δ is the ratio between the stellarator field produced by the helical windings $|\mathbf{B}_\delta|$ to the longitudinal magnetic field B_0 and $\delta \ll 1$ is assumed. The small parameter δ is assumed to be on the order of $\epsilon^{1/2}$, where $\epsilon = a/R_0$ is an inverse aspect ratio and a and R_0 are the minor and major radii of the torus, respectively. This ordering $\delta \sim \epsilon^{1/2}$ is essential for the stellarator expansion. Here ζ is the toroidal angle.

In the expression of (5.1) higher order terms $O(\delta^n)$ with $n \geq 3$ are ignored. The vacuum field $\mathbf{B}_\delta$ is written with the potential ϕ_δ,

$$\mathbf{B}_\delta = \nabla \phi_\delta, \tag{5.2}$$

and ϕ_δ satisfies the Laplace's equation $\nabla^2 \phi_\delta = 0$. In (5.1), $\mathbf{A}$ denotes the vector potential describing a magnetic field generated by a plasma current. It should be noted that, R/R_0 is not expanded with respect to δ in (5.1), where

$R = R_0 + x$ is the local major radius. However, we use the ordering that $\nabla R/R_0$ is the order δ^2, since the toroidal curvature term appears as $O(\delta^2)$ in the ordinary stellarator expansion. This is called the improved stellarator ordering.

We apply the ordering with respect to the small parameter δ to the full MHD equations (2.1) $\sim$ (2.7). Here the gradient operator is assumed by

$$\nabla f = \nabla_\perp f + \delta^2 \nabla\zeta \frac{\partial f}{\partial \zeta}, \tag{5.3}$$

for a scalar function f except the magnetic potential ϕ_δ. Also $\partial/\partial t$ is assumed to be $O(\delta^2)$ in order to eliminate the compressional Alfven waves because our interest is in the plasma dynamics governed by shear Alfven waves which has a slower time scale than the compressional Alfven waves. Since the pressure driven modes are expected to be the dominant instabilities in currentless plasmas, the ordering of the pressure, P, is assumed to be

$$P = \delta^2 P_0 + \delta^3 P_1. \tag{5.4}$$

We note that this ordering corresponds to the high beta ordering of the reduced MHD equations in tokamaks or $\bar{\beta} \sim O(\delta^2)$ [23].

It is convenient to divide a vector quantity into the component along the ζ-direction and the perpendicular component to it. Then, the last term of eq.(5.1) can be written by

$$\nabla \times \mathbf{A} = \nabla\zeta \times \nabla_\perp A + B_\beta \nabla\zeta, \tag{5.5}$$

where A is defined by

$$A = -R^2 \mathbf{A} \cdot \nabla\zeta. \tag{5.6}$$

Here $2\pi A$ is considered as the poloidal flux produced by the plasma current[55]. . .
From Ampère's law (2.6), the current density $\mathbf{J}$ is given by

$$\begin{aligned} \mathbf{J} &= \nabla_\perp B_\beta \times \nabla\zeta + \Delta^* A \nabla\zeta \\ &\sim O(\delta^2), \end{aligned} \tag{5.7}$$

where

$$\Delta^* A \equiv R^2 \nabla_\perp \cdot \left(\frac{\nabla_\perp}{R^2} A \right). \tag{5.8}$$

Substituting eq.(5.1) into Faraday's law eq.(2.5), we obtain

$$-\frac{\partial \mathbf{A}}{\partial t} + \mathbf{E} = \nabla\chi, \tag{5.9}$$

where $\nabla\chi$ is introduced as the integral constant satisfying $\nabla \times \nabla\chi = 0$.
Making the scalar product of (5.9) with $\mathbf{B}$, the leading order terms become

$$\frac{\partial A}{\partial t} + R^2 \mathbf{E} \cdot \nabla\zeta = \frac{R^2}{R_0 B_0} \mathbf{B} \cdot \nabla\chi. \tag{5.10}$$

Here we include the resistivity η in Ohm's law

$$\mathbf{E} + \mathbf{v} \times \mathbf{B} = \eta \mathbf{J}, \tag{5.11}$$

where η is assumed constant and order of δ^2. This ordering shows that $\mathbf{E} \cdot \nabla\zeta$ in eq.(5.10) is $O(\delta^4)$. We assume that both $\mathbf{v}_\perp$ and $\mathbf{E}_\perp$ are $O(\delta^2)$, where $\mathbf{v}_\perp$ is given by the E×B drift velocity in the lowest order. From eq.(5.9),

$$\mathbf{E}_\perp \times \mathbf{B} = R_0 B_0 \nabla\chi \times \nabla\zeta \tag{5.12}$$

is obtained in the leading order. Then, we have

$$\mathbf{v}_\perp = \left(\frac{R}{R_0} \right)^2 \nabla_\perp u \times \nabla\zeta, \tag{5.13}$$

where we have introduced the stream function $u \equiv R_0\chi/B_0$. Thus, Faraday's law combined with Ohm's law is reduced to

$$\frac{\partial A}{\partial t} - \eta\Delta^* A = -\left(\frac{R}{R_0}\right)^2 \mathbf{B}\cdot\nabla u. \tag{5.14}$$

Here the left hand side is $O(\delta^4)$ while the leading order of right hand side is δ^3. The component of the magnetic field generated by helical windings on order of δ is included in $\mathbf{B}\cdot\nabla$ operator .

Next we consider the ordering of the equation of continuity (2.1) and the adiabatic pressure equation (2.3). In order to eliminate the compressional Alfven wave in the toroidal geometry we employ the following incompressibility condition

$$\nabla\cdot\left(\frac{\mathbf{v}}{R^2}\right) = 0. \tag{5.15}$$

If we assume that the mass density ρ_m is constant in time and $O(\delta^0)$, eq.(2.1) leads to the relation,

$$\rho_m R^2 = \rho_{m0} R_0^2, \tag{5.16}$$

where ρ_{m0} is the density at the magnetic axis $R = R_0$. Substituting eq.(5.15) into eq.(2.3), we have the lowest order equation with $O(\delta^4)$ written by

$$\frac{\partial P_0}{\partial t} + \mathbf{v}_\perp\cdot\nabla P_0 = 0. \tag{5.17}$$

Finally, we will derive vorticity equation from the momentum equation (2.2). If we assume that the mass density, ρ_m, is $O(\delta^0)$, the equation in the leading order of δ^2 is given by

$$\nabla_\perp\left(P_0 + \frac{R_0 B_0}{R^2} B_\beta\right) = 0, \tag{5.18}$$

which shows the balance between the plasma pressure and the variation of the toroidal magnetic field through the diamagnetic effect. Making the scalar products between eq.(2.2) and $\mathbf{B}$, in the lowest order we have

$$\rho_{m0} R_0 B_0 \frac{dv_{\|}}{dt} = -\mathbf{B} \cdot \nabla P, \tag{5.19}$$

where

$$v_{\|} = \mathbf{v} \cdot \nabla \zeta. \tag{5.20}$$

Here, using Faraday's law eq.(2.5), Ohm's law eq.(5.11) and eq.(5.17), we can prove

$$\frac{d}{dt} \mathbf{B} \cdot \nabla P \sim O(\delta^6). \tag{5.21}$$

It implies that the leading order of $v_{\|}$ can be considered to be δ^4 which is higher than that of $\mathbf{v}_{\perp}$ given by eq.(5.13). This is consistent with that, if we consider $v_{\|} = \mathbf{B} \cdot \nabla P = 0$ or an equilibrium at $t = 0$, the time evolution of $v_{\|}$ is very slow.

Instead of using the perpendicular component of the momentum equation directly, we consider the quasi-neutrality condition,

$$\nabla \cdot \mathbf{J} = 0. \tag{5.22}$$

From eq.(2.2), we obtain the plasma current

$$\mathbf{J} = -\frac{1}{B^2} \left(\rho_m \frac{d\mathbf{v}}{dt} + \nabla p \right) \times \mathbf{B} + \sigma \mathbf{B}, \tag{5.23}$$

where

$$\sigma \equiv \frac{\mathbf{J} \cdot \mathbf{B}}{B^2} = \frac{\Delta^* A}{R_0 B_0}. \tag{5.24}$$

The last expression of σ is obtained according to the ordering. Substituting eq.(5.23) into eq.(5.22), we obtain the equation including both the order of δ^3 and δ^4;

$$-\frac{\rho_{m0}}{R_0 B_0}\left(\frac{\partial}{\partial t}+\mathbf{v}_\perp\cdot\nabla\right)\nabla_\perp^2 u=\mathbf{B}\cdot\nabla\sigma+\frac{\nabla B^2\cdot\nabla P\times\mathbf{B}}{B^4}, \tag{5.25}$$

where we have used eq.(5.16). Here, it is noted that the leading order of the right hand side of eq.(5.25) is also $O(\delta^3)$. The last term of the right hand side is explicitly written by

$$\begin{aligned}\frac{\nabla B^2\cdot\nabla P\times\mathbf{B}}{B^4} &= \delta^3\left[2\frac{R^2}{R_0^2B_0^2}\nabla\left(\frac{1}{R}\frac{\partial\phi_\delta}{\partial\zeta}\right)\times\nabla_\perp P_0\cdot\hat{\zeta}\right]\\ &+ \delta^4\left[\left\{\frac{R^3}{R_0^3B_0^3}\nabla_\perp|\nabla\phi_\delta|^2-\frac{2}{R_0B_0}\nabla_\perp R\right\}\times\nabla_\perp P_0\cdot\hat{\zeta}\right.\\ &+ 2\frac{R^2}{R_0^2B_0^2}\left\{\nabla\left(\frac{1}{R}\frac{\partial\phi_\delta}{\partial\zeta}\right)\times\nabla_\perp P_0\cdot\left(\nabla\phi_\delta-4\frac{R}{R_0B_0}\frac{\partial\phi_\delta}{\partial\zeta}\nabla\zeta\right)\right.\\ &+ \left.\left.\nabla\left(\frac{1}{R}\frac{\partial\phi_\delta}{\partial\zeta}\right)\times\nabla_\perp P_1\cdot\hat{\zeta}\right\}\right],\end{aligned} \tag{5.26}$$

where $\hat{\zeta}$ is the unit vector in the ζ-direction. Thus, by ordering with respect to the parameter δ, we have the following three equations

$$\frac{\partial A}{\partial t}-\eta\Delta^* A=-\left(\frac{R}{R_0}\right)^2\mathbf{B}\cdot\nabla u \tag{5.27}$$

$$-\frac{\rho_{m0}}{R_0B_0}\left(\frac{\partial}{\partial t}+\mathbf{v}_\perp\cdot\nabla\right)\nabla_\perp^2 u-\frac{\nabla B^2\cdot\nabla P\times\mathbf{B}}{B^4}=\mathbf{B}\cdot\nabla\sigma \tag{5.28}$$

$$\frac{\partial P_0}{\partial t}+\mathbf{v}_\perp\cdot\nabla P_0=0, \tag{5.29}$$

which include the higher order toroidal corrections than the usual large aspect ratio limit. These equations are not closed because four unknown quantities A, u, P_0, and P_1 exist and the orders of the all terms are not unified

in eq.(5.27) and eq.(5.28). This problem will be resolved by applying the averaging method to the above equations as explained in the next section.

5.3 Averaging method for the reduced MHD equations

As explained in Sec.5.2, the reduced equations (5.27) and (5.28) include terms with different orders with respect to δ. The reason is because the helical magnetic field given by $\nabla\phi_\delta$ contains a rapid variation in ζ with a scale length $2\pi R_0/N$. We have assumed that we can separate the rapid oscillating scale $\tilde{\zeta}$ from the slowly varying scale $\overline{\zeta}$ with the ordering

$$\frac{\partial}{\partial\overline{\zeta}} \sim \delta^2 \frac{\partial}{\partial\tilde{\zeta}}. \tag{5.30}$$

Since we are interested in the global motion of the plasma which has a larger wave length than the scale of $\tilde{\zeta}$, we eliminate the rapid motion associated with the $\tilde{\zeta}$ coordinate by averaging the reduced equations in the ζ-direction. Here we define the average for one field period of the ζ-direction in the following manner

$$\overline{f} \equiv \frac{N}{2\pi}\int_0^{2\pi/N} f d\zeta. \tag{5.31}$$

We also introduce the indefinite integral as

$$\langle f\rangle \equiv \int_0^{\zeta} f d\zeta + C, \tag{5.32}$$

where the constant of integration C determined by

$$\overline{\langle f\rangle} = 0. \tag{5.33}$$

Here we note that eqs. (5.27) and (5.28) have the same form as magnetic differential equation

$$\mathbf{B}\cdot\nabla F = G, \tag{5.34}$$

where F and G are assumed to be expanded in power of δ as

$$\begin{aligned} F &= \delta^2 F_0 + \delta^3 F_1 + \delta^4 F_2 \\ G &= \delta^3 G_1 + \delta^4 G_2, \end{aligned} \tag{5.35}$$

and we note that they depend on both scale $\tilde{\zeta}$ and $\bar{\zeta}$,

$$\begin{aligned} F &= F(R, \tilde{\zeta}, \bar{\zeta}, Z) \\ G &= G(R, \tilde{\zeta}, \bar{\zeta}, Z). \end{aligned} \tag{5.36}$$

Here (R, ζ, Z) is the cylindrical coordinates. The reason why we assume no $O(\delta^2)$ term in G in (5.35) is that the RHS of (5.27) or (5.28) has such a property.

Then, we have the lowest order equation of eq.(5.34) with $O(\delta^2)$ written by

$$\frac{R_0 B_0}{R^2} \frac{\partial F_0}{\partial \tilde{\zeta}} = 0, \tag{5.37}$$

which means that F_0 does not contain the rapid oscillation and

$$F_0 = F_0(R, \bar{\zeta}, Z). \tag{5.38}$$

The next order equation of eq.(5.34) is given by

$$\frac{R_0 B_0}{R^2} \frac{\partial F_1}{\partial \tilde{\zeta}} + \mathbf{B}_\delta \cdot \nabla_\perp F_0 = G_1. \tag{5.39}$$

In order to obtain F_1, we integrate eq.(5.39) with respect to $\tilde{\zeta}$,

$$F_1 = -\frac{R^2}{R_0 B_0} \left[\langle \mathbf{B}^\delta \rangle \cdot \nabla_\perp F_0 - \langle G_1 \rangle \right]. \tag{5.40}$$

For the order of δ^4, eq.(5.34) is expressed by

$$\begin{aligned} \frac{R_0 B_0}{R^2} \frac{\partial F_0}{\partial \bar{\zeta}} + (\nabla \zeta \times \nabla_\perp A) \cdot \nabla_\perp F_0 \\ + \mathbf{B}_\delta \cdot \nabla F_1 + \frac{R_0 B_0}{R^2} \frac{\partial F_2}{\partial \tilde{\zeta}} &= G_2. \end{aligned} \tag{5.41}$$

When we integrate eq.(5.41) over one period in the ζ-direction, the forth term of the left hand side drops and we have

$$\frac{R_0 B_0}{R^2}\frac{\partial F_0}{\partial \bar{\zeta}} + (\nabla\zeta \times \nabla_\perp A)\cdot\nabla_\perp F_0 + \overline{\mathbf{B}_\delta \cdot \nabla F_1} = \overline{G_2}. \tag{5.42}$$

Here we have assumed that A does not depend upon $\tilde{\zeta}$. From eq.(5.40), we obtain

$$\begin{aligned}\overline{\mathbf{B}_\delta \cdot \nabla F_1} &= \frac{1}{R_0 B_0}\overline{\mathbf{B}_\delta \cdot \nabla[R^2\{\langle G_1\rangle - \langle \mathbf{B}_\delta\rangle \cdot \nabla_\perp F_0\}]} \\ &= \frac{1}{R_0 B_0}[\overline{\mathbf{B}^\delta \cdot \nabla(R^2\langle G_1\rangle)} - \frac{1}{2}\nabla_\perp F_0 \times \nabla[R^3\overline{\langle \mathbf{B}^\delta\rangle \times \mathbf{B}^\delta}\cdot\hat{\zeta}]\cdot\nabla\zeta,\end{aligned} \tag{5.43}$$

where we have used $\nabla \times \langle \mathbf{B}_\delta\rangle = \nabla\cdot\langle \mathbf{B}_\delta\rangle = 0$. Substituting eq.(5.43) into eq.(5.42) we have the magnetic differential equation (5.34) averaged over one period which can be written by

$$\overline{\mathbf{B}}\cdot\nabla F_0 = \overline{G_2} - \frac{1}{R_0 B_0}\overline{\mathbf{B}_\delta \cdot \nabla(R^2\langle G_1\rangle)}, \tag{5.44}$$

where the averaged magnetic differential operator is given by

$$\overline{\mathbf{B}}\cdot\nabla = \frac{R_0 B_0}{R^2}\frac{\partial}{\partial\zeta} - \nabla_\perp\Psi \times \nabla\zeta\cdot\nabla_\perp \tag{5.45}$$

with the averaged poloidal flux,

$$\Psi = A + \frac{R^3}{2R_0 B_0}\overline{\langle \mathbf{B}_\delta\rangle \times \mathbf{B}_\delta}\cdot\hat{\zeta}. \tag{5.46}$$

Here the bar on ζ has been dropped for simplicity. Equations (5.45) and (5.46) imply that the operator $\overline{\mathbf{B}}\cdot\nabla$ is on the order of δ^2. When we go back to eqs.(5.27) and (5.28), they can be made to have only terms unified by the order of δ^4 with the averaged magnetic differential operator given by (5.45).

From eq.(5.44), the averaged equation of (5.27) is immediately obtained as

$$\frac{\partial A}{\partial t} - \eta \Delta^* A = -\left(\frac{R}{R_0}\right)^2 \overline{\mathbf{B}} \cdot \nabla u. \tag{5.47}$$

In this case, there is no term corresponding to G_1.

In applying the averaged equation (5.44) to eq.(5.28), G_1 and G_2 are found from eq.(5.26) and the left hand side of eq.(5.28). In order to determine P_1 in eq.(5.26), we also apply eq.(5.40) to the magnetic differential equation $\mathbf{B} \cdot \nabla P = 0$ obtained from eq.(5.21). Then, we find the expression,

$$P_1 = -\frac{R^2}{R_0 B_0} \langle \mathbf{B}_\delta \rangle \cdot \nabla_\perp P_0. \tag{5.48}$$

With eq.(5.48) we can obtain G_1 and G_2, in the following averaged form;

$$\begin{aligned} \overline{G_2} \;=\; & \frac{1}{B_0} \nabla_\perp \left(\frac{R}{R_0} + \frac{R^3}{R_0^3} \frac{\overline{|B_\delta|^2}}{B_0^2} \right) \times \nabla_\perp P_0 \cdot \hat{\zeta} \\ & - \frac{\rho_{m0}}{R_0 B_0} \left(\frac{\partial}{\partial t} + \mathbf{v}_\perp \cdot \nabla \right) \nabla_\perp^2 u \\ & + 2 \frac{R^3}{R_0^3 B_0^3} \left[\nabla_\perp P_0 \times \overline{\nabla_\perp |\nabla_\perp \phi_\delta|^2} - \overline{\mathbf{B}_\delta \times \nabla_\perp (\mathbf{B}_\delta \cdot \nabla_\perp P_0)} \right] \cdot \hat{\zeta} \end{aligned} \tag{5.49}$$

$$\begin{aligned} \frac{1}{R_0 B_0} \mathbf{B}_\delta \cdot \nabla (R \langle G_1 \rangle) \;=\; & \frac{2R^3}{R_0^3 B_0^3} \hat{\zeta} \cdot \left[\overline{\mathbf{B}^\delta \times \nabla_\perp (\nabla_\perp \phi_\delta \cdot \nabla P_0)} \right. \\ & \left. + \overline{\nabla_\perp |\nabla_\perp \phi_\delta|^2} \times \nabla_\perp P_0 \right]. \end{aligned} \tag{5.50}$$

Substituting (5.49) and (5.50) into (5.44), we have the final expression

$$\begin{aligned} \overline{\mathbf{B}} \cdot \nabla \sigma \;=\; & \frac{R_0}{B_0} \nabla_\perp \left(\frac{R^2}{R_0^2} + \frac{R^4}{R_0^4} \frac{\overline{|\mathbf{B}_\delta|^2}}{B_0^2} \right) \times \nabla_\perp P_0 \cdot \nabla \zeta \\ & - \frac{\rho_{m0}}{R_0 B_0} \left(\frac{\partial}{\partial t} + \mathbf{v}_\perp \cdot \nabla \right) \nabla_\perp^2 u. \end{aligned} \tag{5.51}$$

From the above procedures, we have obtained the reduced MHD equations for the resistive modes in stellarator/heliotron and we summarize them in the following way;

$$\frac{\partial A}{\partial t} = -\left(\frac{R}{R_0}\right)^2 \mathbf{B}\cdot\nabla u + \eta J_\zeta \tag{5.52}$$

$$\rho_{m0}\frac{dU}{dt} = -\mathbf{B}\cdot\nabla J_\zeta + R_0^2\nabla_\perp\Omega\times\nabla_\perp P\cdot\nabla\zeta \tag{5.53}$$

$$\frac{dP}{dt} = 0, \tag{5.54}$$

where

$$\mathbf{B}\cdot\nabla = \frac{R_0B_0}{R^2}\frac{\partial}{\partial\zeta} - \nabla_\perp\Psi\times\nabla\zeta\cdot\nabla_\perp \tag{5.55}$$

$$\frac{d}{dt} = \frac{\partial}{\partial t} + \mathbf{v}_\perp\cdot\nabla \tag{5.56}$$

$$U = \nabla_\perp^2 u \tag{5.57}$$

$$J_\zeta = \Delta^* A \tag{5.58}$$

$$\Psi = A + \Psi_v \tag{5.59}$$

$$\Psi_v = \frac{R^3}{R_0B_0}\overline{B_{\delta R}\int_0^\zeta B_{\delta Z}d\zeta} \tag{5.60}$$

$$\Omega = \frac{R^2}{R_0^2} + \frac{R^4}{R_0^4}\frac{\overline{|\mathbf{B}_\delta|^2}}{B_0^2} \tag{5.61}$$

$$\mathbf{v}_\perp = \left(\frac{R}{R_0}\right)^2\nabla_\perp u\times\nabla\zeta. \tag{5.62}$$

Here the bar on $\mathbf{B}\cdot\nabla$ and the subscript 0 of the pressure P are dropped. Equation (5.55) implies that the averaged magnetic field is expressed by

$$\mathbf{B} = R_0B_0\nabla\zeta + \nabla\zeta\times\nabla_\perp\Psi \tag{5.63}$$

and the function $2\pi\Psi$ denotes the averaged poloidal flux. Equations (5.52) $\sim$ (5.55) are the closed three field equations for three scalar functions, A, u,

and P. By comparing them with the reduced MHD equations for stellarators derived by Strauss[24], our three-field equations keep higher order toroidal corrections through the factor R/R_0 and the operator Δ^*. If we put $\phi_\delta = 0$ or the stellarator field is removed, the reduced MHD equations for high beta tokamaks including higher order toroidal corrections are obtained. If we put $\eta = 0$, we can use these three-field equations for studying the ideal pressure-driven modes. A significant limitation for the three-field equation comes from the averaging method. Short wave length modes comparable to or shorter than the pitch length of the stellarator field are not treated by them, since description of such modes is questionable by a kind of course graining or the averaging procedure.

5.4 Averaged equilibrium of heliotron/ torsatron

From the reduced MHD equations, we can derive an equation describing a static equilibrium by putting $\partial/\partial t = u = 0$ in eqs.(5.52)~(5.54). If we assume the averaged equilibrium is axisymmetric and use $P = P(\Psi)$, eq.(5.53) gives the Grad-Shafranov type equation written by

$$\Delta^* A = -R_0^2 \frac{dP}{d\Psi}\Omega + g(\Psi), \tag{5.64}$$

where $g(\Psi)$ is the constant of integration. Equation (5.64) coincides with that derived by Nakamura et al.[15] based on the stellarator expansion technique for the MHD equilibrium equation (2.9) ~ (2.11) including higher order toroidal corrections. Except the higher order toroidal corrections in Δ^* and Ψ_v eq.(5.64) agrees with the equation originally derived by Greene and Johnson [6]. The function, $g(\Psi)$, can be determined by the currentless constraint, which is the most appropriate assumption in stellarators. From eq.(5.7), this constraint for the toroidal net current I_t is expressed by

$$I_t \equiv \int \mathbf{J} \cdot \nabla\zeta dV = \int \frac{\Delta^* A}{R^2} dV = 0. \tag{5.65}$$

By using eq.(5.64) on each magnetic surface, $g(\Psi)$ must satisfy the condition,

$$g(\Psi) = R_0^2 \frac{dP}{d\Psi} \ll \Omega \gg, \tag{5.66}$$

where we have used the flux surface average defined by

$$\ll \Omega \gg = \oint \Omega \frac{d\ell}{B} \Big/ \oint \frac{d\ell}{B}. \tag{5.67}$$

For a given $P(\Psi)$ and $g(\Psi)$, eq.(5.64) is solved by the 'Equilibrium' part of the STEP code with the given data for the vacuum magnetic field, $\mathbf{B}_\delta$. We obtain Ψ_v and Ω defined by (5.60) and (5.61) by performing the averaging procedure in the toroidal direction with vacuum magnetic fields by the Biot-Savart law as the input data for the STEP code, instead of using the Bessel function model corresponding to the straight cylindrical approximation, which was used in the previous calculations[6]. In this code the rectangular coordinates (R, Z) are employed, and the averaged equilibrium for stellarator/heliotron configuration is obtained numerically under the free boundary condition where the vacuum region exists outside the toroidal plasma. The plasma position is decided by assuming a limiter position in the STEP code. Its position is usually chosen so that it coincides with the outermost vacuum flux surface. After the equilibrium is obtained by the STEP code, the stability problem can be studied by using eq.(5.52) $\sim$ (5.54).

The rotational transform and the specific volume characterize the MHD equilibrium state. We need the expression of the averaged toroidal flux Φ to calculate the rotational transform and the specific volume. Φ is defined by

$$\Phi = \frac{1}{2\pi} \int \mathbf{B} \cdot \nabla\zeta dV. \tag{5.68}$$

Substituting (5.63) into (5.68) and using the relation

$$dV = \frac{d\Psi ds R d\zeta}{|\nabla\Psi|}, \tag{5.69}$$

where ds is the line element in the poloidal direction on the $\Psi = const.$ surface, we obtain the averaged toroidal flux by

$$\Phi = R_0 B_0 \int d\Psi \oint \frac{ds}{R|\nabla\Psi|}. \tag{5.70}$$

This expression is essentially same as that for a tokamak. We note that eq.(5.68) is valid in the lowest order or in the limit of cylindrical approximation in the stellarator/heliotron configuration. To improve the accuracy, we use (5.1) for eq.(5.68) and average over one period in the ζ-direction again[15]. Then, the more correct expression of Φ is given by

$$\Phi = R_0 B_0 \int d\Psi \oint \frac{F_t ds}{R|\nabla\Psi|}, \tag{5.71}$$

where

$$F_t = 1 - \frac{R^2}{R_0^2}\overline{|\mathbf{B}^\delta|^2} - \frac{P}{B_0^2} \tag{5.72}$$

which includes higher order corrections. If we assume $F_t = 1$, we recover eq.(5.70). From (5.71) the rotational transform is given by

$$\iota(\Psi) = \frac{d(2\pi\Psi)}{d\Phi} = \frac{2\pi}{R_0 B_0}\left(\oint \frac{F_t ds}{R|\nabla\Psi|}\right)^{-1}. \tag{5.73}$$

The specific volume is obtained from eqs.(5.69) and (5.73) by

$$V'(\Phi) = \frac{dV}{d\Phi} = 2\pi\iota \oint \frac{Rds}{|\nabla\Psi|}. \tag{5.74}$$

5.5 Reduced MHD equations in the flux coordinates (ρ, θ, ζ)

Since the reduced MHD equations (5.52) and (5.53) derived in Sec.5.4 have the form of the magnetic differential equation, it is crucial to calculate the differential operator along the magnetic field line, $\mathbf{B} \cdot \nabla$, accurately. The expression for the operator depends on the coordinate system. In MHD equilibrium the coordinates where magnetic field lines are seen straight make the expression reasonably simple. Thus we introduce the flux coordinates $(\Psi_{eq}, \theta, \zeta)$, where Ψ_{eq} denotes the averaged equilibrium poloidal flux obtained by eq.(5.59) and ζ is the toroidal angle. And the poloidal angle θ is chosen so that the lines of force become straight in (θ, ζ) plane with $\Psi_{eq} = const.$ Then the magnetic field at MHD equilibrium is expressed by[56]

$$\mathbf{B} = \nabla\zeta \times \nabla\Psi_{eq} + \frac{1}{\iota(\Psi_{eq})}\nabla\Psi_{eq} \times \nabla\theta, \tag{5.75}$$

and differential operator $\mathbf{B} \cdot \nabla$ is given by

$$\mathbf{B} \cdot \nabla = D_F \left(\frac{\partial}{\partial\theta} + \frac{1}{\iota}\frac{\partial}{\partial\zeta} \right), \tag{5.76}$$

where D_F is the Jacobian in the flux coordinates given by

$$\begin{aligned} D_F^{-1} &= \nabla\Psi_{eq} \times \nabla\theta \cdot \nabla\zeta \\ &= |\nabla\Psi_{eq}||\nabla_s\theta||\nabla\zeta|. \end{aligned} \tag{5.77}$$

Here the operator ∇_s is defined by[14]

$$\nabla_s \equiv \nabla - \frac{\nabla\Psi_{eq}\nabla\Psi_{eq} \cdot \nabla}{|\nabla\Psi_{eq}|^2}, \tag{5.78}$$

which means the gradient operator along the magnetic surface labeled by the poloidal flux Ψ_{eq}. We have assumed in eq.(5.77) that the averaged equilibrium under the stellarator expansion is axisymmetric, that is,

$$\nabla\Psi_{eq}\cdot\nabla\zeta = 0, \quad \nabla\theta\cdot\nabla\zeta = 0. \tag{5.79}$$

From the analogy of the large aspect ratio limit case, the Jacobian (5.77) is considered to have the form

$$D_F = \frac{H(\Psi_{eq},\theta,\zeta)}{\iota(\Psi_{eq})}. \tag{5.80}$$

By using eq.(5.77) with (5.80), we obtain

$$\frac{d\theta}{ds} = \frac{\iota R}{H|\nabla\Psi_{eq}|}. \tag{5.81}$$

The requirement that θ increases by 2π during one poloidal circuit with the rotational transform eq.(5.73) gives the expression of H,

$$H = \frac{F_t R_0 B_0}{R^2}. \tag{5.82}$$

Thus, the Jacobian D_F is given by

$$D_F = \frac{R^2}{R_0 B_0 \iota(\Psi_{eq}) F_t}, \tag{5.83}$$

which includes the higher order correction, F_t. The coordinates (Ψ_{eq},θ,ζ) having the Jacobian eq.(5.83) with $F_t = 1$ are called the PEST coordinates[13].

In order to write the basic equations in the flux coordinates with forms similar to those in the cylindrical geometry, we introduce ρ instead of Ψ_{eq} as the normalized radial coordinate with $0 \le \rho \le 1$ which is defined by

$$\rho = \left(\frac{\Psi_{eq}-\Psi_{min}}{\Psi_{max}-\Psi_{min}}\right)^{1/2}, \tag{5.84}$$

where Ψ_{min} and Ψ_{max} denote the values of Ψ_{eq} at the magnetic axis and at the outermost surface, respectively. Then, the Jacobian of this (ρ, θ, ζ) coordinates, D_R, is written as

$$D_R = (\nabla\rho \times \nabla\theta \cdot \zeta)^{-1} = R_0 \epsilon^2 \frac{\rho R^2}{\iota F_t}. \tag{5.85}$$

Here we define the normalized minor radius a as

$$a \equiv \left[\frac{2(\Psi_{max} - \Psi_{min})}{B_0}\right]^{1/2}. \tag{5.86}$$

In the (ρ, θ, ζ) coordinates, the reduced MHD equations (5.52) $\sim$ (5.54) are written in the following way,

$$\frac{\partial A}{\partial t} = -\frac{\partial u}{\partial \zeta} - \iota F_t \left(\frac{\partial \Psi}{\partial \rho}\frac{1}{\rho}\frac{\partial u}{\partial \theta} - \frac{1}{\rho}\frac{\partial \Psi}{\partial \theta}\frac{\partial u}{\partial \rho}\right) + \frac{J_\zeta}{S} \tag{5.87}$$

$$\frac{\partial U}{\partial t} + \iota F_t \left(\frac{\partial U}{\partial \rho}\frac{1}{\rho}\frac{\partial u}{\partial \theta} - \frac{1}{\rho}\frac{\partial U}{\partial \theta}\frac{\partial u}{\partial \rho}\right) = \left(\frac{R}{R_0}\right)^2 \left[-\frac{\partial J_\zeta}{\partial \zeta}\right. \tag{5.88}$$

$$\left. -\iota F_t \left(\frac{\partial \Psi}{\partial \rho}\frac{1}{\rho}\frac{\partial J_\zeta}{\partial \theta} - \frac{1}{\rho}\frac{\partial \Psi}{\partial \theta}\frac{\partial J_\zeta}{\partial \rho}\right) + \frac{\beta_0}{2\epsilon^2}\iota F_t \left(\frac{\partial \Omega}{\partial \rho}\frac{1}{\rho}\frac{\partial P}{\partial \theta} - \frac{1}{\rho}\frac{\partial \Omega}{\partial \theta}\frac{\partial P}{\partial \rho}\right)\right]$$

$$\frac{\partial P}{\partial t} + \iota F_t \left(\frac{\partial P}{\partial \rho}\frac{1}{\rho}\frac{\partial u}{\partial \theta} - \frac{1}{\rho}\frac{\partial P}{\partial \theta}\frac{\partial u}{\partial \rho}\right) = 0. \tag{5.89}$$

Here we have normalized the quantities as follows:

$$\left.\begin{array}{ll} \Psi \to a^2 B_0 \Psi, & J_\zeta \to B_0 J_\zeta \\ u \to (a^2 R_0/\tau_{Hp}) u, & U \to (R_0/\tau_{Hp}) U \\ P \to P_0 P, & t \to \tau_{Hp} t \end{array}\right\}, \tag{5.90}$$

where P_0 is the equilibrium pressure at the magnetic axis and τ_{Hp} is the poloidal Alfven time defined by

$$\tau_{Hp} = \frac{R_0\sqrt{\rho_{m0}}}{B_0}. \tag{5.91}$$

$S = \tau_R/\tau_{Hp}$ in eq.(5.87) is the magnetic Reynolds number and $\tau_R = a^2/\eta$ is the resistive diffusion time, and $\beta_0 = 2P_0/B_0^2$ in (5.88) is the beta value at the magnetic axis.

When $F_t = 1$ is assumed in eqs.(5.87)$\sim$(5.89) to keep the lowest order quantity, we also use $(R/R_0)^2 = 1$ in eq.(5.88). Since we are interested in the linear modes and the beta limit determined by them, we linearize eqs.(5.87)$\sim$(5.89);

$$\frac{\partial A}{\partial t} = -\frac{\partial u}{\partial \zeta} - \iota \frac{\partial u}{\partial \theta} + \frac{J_\zeta}{S} \tag{5.92}$$

$$\frac{\partial U}{\partial t} = -\frac{\partial J_\zeta}{\partial \zeta} - \iota \frac{\partial J_\zeta}{\partial \theta} - \iota \left(\frac{\partial A}{\partial \rho} \frac{1}{\rho} \frac{\partial J_{\zeta eq}}{\partial \theta} - \frac{1}{\rho} \frac{\partial A}{\partial \theta} \frac{\partial J_{\zeta eq}}{\partial \rho} \right) + \frac{\beta_0}{2\epsilon^2} \iota \left(\frac{\partial \Omega_{eq}}{\partial \rho} \frac{1}{\rho} \frac{\partial P}{\partial \theta} - \frac{1}{\rho} \frac{\partial \Omega_{eq}}{\partial \theta} \frac{\partial P}{\partial \rho} \right) \tag{5.93}$$

$$\frac{\partial P}{\partial t} = -\iota \frac{dP_{eq}}{d\rho} \frac{1}{\rho} \frac{\partial u}{\partial \theta}, \tag{5.94}$$

where the subscript 'eq' is attached to equilibrium quantities. From eqs.(5.57) and (5.58) U and J_ζ are written in the (ρ, θ, ζ) coordinates as

$$J_\zeta = \frac{R^2}{D_R} \left\{ \frac{\partial}{\partial \rho} \left[\frac{D_R}{R^2} \left(g^{\rho\rho} \frac{\partial A}{\partial \rho} + g^{\rho\theta} \frac{\partial A}{\partial \theta} \right) \right] + \frac{\partial}{\partial \theta} \left[\frac{D_R}{R^2} \left(g^{\rho\theta} \frac{\partial A}{\partial \rho} + g^{\theta\theta} \frac{\partial A}{\partial \theta} \right) \right] \right\} \tag{5.95}$$

$$U = \frac{1}{D_R} \left\{ \frac{\partial}{\partial \rho} \left[D_R \left(g^{\rho\rho} \frac{\partial u}{\partial \rho} + g^{\rho\theta} \frac{\partial u}{\partial \theta} \right) \right] + \frac{\partial}{\partial \theta} \left[D_R \left(g^{\rho\theta} \frac{\partial u}{\partial \rho} + g^{\theta\theta} \frac{\partial u}{\partial \theta} \right) \right] \right\}, \tag{5.96}$$

with the metric elements

$$g^{\rho\rho} = |\nabla \rho|^2, \quad g^{\rho\theta} = \nabla \rho \cdot \nabla \theta, \quad g^{\theta\theta} = |\nabla \theta|^2. \tag{5.97}$$

5.6 Numerical scheme of the RESORM code

To solve the linearized reduced MHD equations (5.92) $\sim$ (5.94) as an initial value problem for both the ideal and resistive modes, we have developed a linear resistive stability code.

We use the Fourier series with respect to angle variables θ and ζ. Since the up-down symmetry is maintained in the usual stellarator/heliotron, the perturbations are expanded as

$$\begin{aligned} A(\rho,\theta,\zeta) &= \sum_{m=-\infty}^{+\infty} A_{mn}(\rho)\cos(m\theta - n\zeta), \\ u(\rho,\theta,\zeta) &= \sum_{m=-\infty}^{+\infty} u_{mn}(\rho)\sin(m\theta - n\zeta), \\ P(\rho,\theta,\zeta) &= \sum_{m=-\infty}^{+\infty} P_{mn}(\rho)\cos(m\theta - n\zeta). \end{aligned} \tag{5.98}$$

These choice are also related to the spatial parity conservation in eqs. (5.92) $\sim$ (5.94). Here it is noted that m and n are poloidal and toroidal mode number, respectively. Since there is no coupling between the different toroidal modes in our approximation, only one toroidal mode number, n, is assigned in (5.98). The equilibrium quantities and the metrics are expanded as

$$\begin{aligned} \Omega_{eq}(\rho,\theta) &= \sum_{m=0}^{+\infty} \Omega_{eqm}(\rho)\cos(m\theta), \\ J_{\zeta eq}(\rho,\theta) &= \sum_{m=0}^{+\infty} J_{\zeta eqm}(\rho)\cos(m\theta), \end{aligned} \tag{5.99}$$

$$
\begin{aligned}
g^{\rho\rho}(\rho,\theta) &= \sum_{m=0}^{+\infty} g_m^{\rho\rho}(\rho)\cos(m\theta), \\
g^{\rho\theta}(\rho,\theta) &= \sum_{m=0}^{+\infty} g_m^{\rho\theta}(\rho)\sin(m\theta), \\
g^{\theta\theta}(\rho,\theta) &= \sum_{m=0}^{+\infty} g_m^{\theta\theta}(\rho)\cos(m\theta),
\end{aligned}
\tag{5.100}
$$

with respect to the poloidal angle θ. It should be noted that, in the present stellarator expansion approximation, the lowest order equilibrium quantities do not depend on ζ. In this case, the linearized reduced equations (5.92) $\sim$ (5.94) for each n are written by

$$
\frac{\partial A_{mn}}{\partial t} = (n - m\iota)u_{mn} + \frac{J_{mn}}{S} \tag{5.101}
$$

$$
\begin{aligned}
&\frac{\partial U_{mn}}{\partial t} = -(n - m\iota)J_{\zeta mn} \\
&+\frac{\iota}{2\rho}\sum_{i+j=m}\left[j\left(\frac{\partial A_{in}}{\partial \rho}J_{\zeta eqj} + \frac{\beta_0}{2\epsilon^2}\frac{\partial P_{in}}{\partial \rho}\Omega_{eqj}\right) - i\left(A_{in}\frac{\partial J_{\zeta eqj}}{\partial \rho} + \frac{\beta_0}{2\epsilon^2}P_{in}\frac{\partial \Omega_{eqj}}{\partial \rho}\right)\right] \\
&-\frac{\iota}{2\rho}\sum_{i+j=m}\left[j\left(\frac{\partial A_{in}}{\partial \rho}J_{\zeta eqj} + \frac{\beta_0}{2\epsilon^2}\frac{\partial P_{in}}{\partial \rho}\Omega_{eqj}\right) + i\left(A_{in}\frac{\partial J_{\zeta eqj}}{\partial \rho} + \frac{\beta_0}{2\epsilon^2}P_{in}\frac{\partial \Omega_{eqj}}{\partial \rho}\right)\right]
\end{aligned}
\tag{5.102}
$$

$$
\frac{\partial P_{mn}}{\partial t} = -\frac{\iota}{\rho}mu_{mn}\frac{dP_{eq}}{d\rho}. \tag{5.103}
$$

In eqs.(5.101) and (5.102), the first term of the right hand side shows the mode resonance at $\iota = n/m$.

We use the finite difference representation in the radial coordinate ρ. We assume the conducting wall at $\rho = 1$, which corresponds to the fixed boundary condition. Since the resistive instabilities have properties of internal mode, this boundary condition is appropriate for the resistive MHD stability. Since $\mathbf{v}_\perp \cdot \nabla\rho = \mathbf{B} \cdot \nabla\rho = 0$ at this boundary, they may lead to

$$
u_{mn} = A_{mn} = P_{mn} = 0 \tag{5.104}
$$

at $\rho = 1$. At the magnetic axis, $\rho = 0$, all quantities must behave regularly. Then we impose the conditions

$$\begin{aligned} u_{mn} = A_{mn} = P_{mn} = 0 \qquad & \text{for } m \neq 0 \text{ and } n \neq 0 \\ \frac{\partial u_{mn}}{\partial \rho} = \frac{\partial A_{mn}}{\partial \rho} = \frac{\partial P_{mn}}{\partial \rho} = 0 \quad & \text{for m} = 0 \text{ and } n \neq 0 \end{aligned} \tag{5.105}$$

As for the numerical method of the time evolution, we employ the two-step algorithm. For the equation with the following form

$$\frac{\partial f}{\partial t} = g, \tag{5.106}$$

the first and the second steps are given by

$$\begin{aligned} f^{t+\Delta t/2} &= f^t + \frac{\Delta t}{2} g^t \\ f^{t+\Delta t} &= f^t + \Delta t g^{t+\Delta t/2}, \end{aligned} \tag{5.107}$$

where $g^{t+\Delta t/2}$ can be calculated by using $f^{t+\Delta t/2}$. The perturbations A_{mn}, u_{mn} and P_{mn} for each n must have the same time-dependence as $e^{\gamma t}$ for the linear eigenmode. Thus, the growth rate γ can be obtained from

$$\gamma = \frac{1}{2}\frac{\partial}{\partial t} \ln E_K = \frac{1}{2}\frac{\partial}{\partial t} \ln E_M, \tag{5.108}$$

where E_K and E_M are the perturbed kinetic and magnetic energies, respectively, given by

$$\begin{aligned} E_K = \frac{1}{2}\int v_\perp^2 dV &= \frac{1}{2}\int |\nabla_\perp u|^2 \frac{R^2}{R_0^4} dV \\ E_M = \frac{1}{2}\int B_\perp^2 dV &= \frac{1}{2}\int |\nabla_\perp A|^2 \frac{R^2}{R_0^4} dV. \end{aligned} \tag{5.109}$$

In the code we calculate the growth rate at each time step. We follow time evolution of the perturbation until γ converges to an exponential growth rate.

When these numerical procedures are applied to the linearized reduced equations (5.101), (5.102) and (5.103), it is essential to consider the coupling between different poloidal modes through the toroidal geometry where the equilibrium quantities have θ-dependence. In the numerical calculations the geometrical coupling makes the matrix size large in obtaining u_{mn} from the Poisson equation $\nabla_\perp^2 u = U$. Since we approximate the ρ-derivatives with the central differences, the matrix which we must invert to solve the Poisson equation becomes block-tridiagonal with $N \times N$ blocks, where N is the number of radial grid points. Each block size is $M \times M$ with M being the number of total poloidal modes included in the calculation. We apply the recurrence formula for the blocks in the matrix inversion procedure. If we use $\mathbf{u}_j$ and $\mathbf{U}_j$ at the j-th radial grid to represent M poloidal components and denote three blocks which operate to $\mathbf{u}_{j-1}$, $\mathbf{u}_j$, $\mathbf{u}_{j+1}$, as L_j, C_j, and R_j, the Poisson equation can be describes as

$$\mathsf{L}_j \mathbf{u}_{j-1} + \mathsf{C}_j \mathbf{u}_j + \mathsf{R}_j \mathbf{u}_{j+1} = \mathbf{U}_j. \tag{5.110}$$

Then the recurrence formula gives the solution u_j as follows,

$$\begin{aligned} \mathbf{u}_j &= \mathsf{A}_j^{-1}(\mathbf{S}_j - \mathsf{B}_j \mathbf{u}_{j+1}) \qquad \text{for } j \neq N \\ \mathbf{u}_j &= \mathsf{A}_j^{-1}\mathbf{S}_j \qquad\qquad\qquad\quad \text{for } j = N, \end{aligned} \tag{5.111}$$

where

$$\left.\begin{aligned} \mathsf{A}_j &= \mathsf{C}_j - \mathsf{L}_j(\mathsf{A}_{j-1})^{-1}\mathsf{B}_{j-1} \\ \mathsf{B}_j &= \mathsf{R}_j \\ \mathbf{S}_j &= \mathbf{U}_j - \mathsf{L}_j(\mathsf{A}_{j-1})^{-1}\mathbf{S}_{j-1} \end{aligned}\right\} \quad \text{for } j \neq 1 \tag{5.112}$$

$$\left.\begin{aligned} \mathsf{A}_j &= \mathsf{C}_j \\ \mathsf{B}_j &= \mathsf{R}_j \\ \mathbf{S}_j &= \mathbf{U}_j \end{aligned}\right\} \quad \text{for } j = 1. \tag{5.113}$$

The code based on the above numerical model is called RESORM (Resistive Stability based on Reduced MHD). The flow chart of this code is shown in Fig.5.1.

5.7 Eigenvalue problem for ideal MHD stability

To investigate the ideal linear MHD stability, there are two ways. One is to use the initial value problem approach by assuming zero resistivity, and the other is based on the energy principle. Here the latter method is explained briefly for the introduction of the 'Stability' part of the STEP code[11].

When the time dependence of the perturbation is given by $\xi \propto e^{\gamma t}$, the Lagrangian for the linearized MHD equations is written by

$$L = \gamma^2 K - \delta W, \tag{5.114}$$

with the kinetic energy of the perturbation

$$K = \frac{1}{2}\int_p dV \rho_m \mid \boldsymbol{\xi} \mid^2, \tag{5.115}$$

and the perturbed potential energy

$$\delta W = \frac{1}{2}\int_p dV[\mid \mathbf{Q} \mid^2 + \mathbf{J}\times\boldsymbol{\xi}\cdot\mathbf{Q} + \boldsymbol{\xi}\cdot\nabla P\nabla\cdot\boldsymbol{\xi} + \Gamma P(\nabla\cdot\boldsymbol{\xi})^2] + \int_v dV \mid \delta\mathbf{B} \mid^2 . \tag{5.116}$$

Here the perturbed magnetic field in the plasma is given by

$$\mathbf{Q} = \nabla\times(\boldsymbol{\xi}\times\mathbf{B}). \tag{5.117}$$

The integrals $\int_p dV$ and $\int_v dV$ mean the volume integral in the plasma region and that in the vacuum region, respectively, and $\delta\mathbf{B}$ denotes the perturbed magnetic field in the vacuum region. Since we assume no surface current

at the plasma-vacuum interface, the surface term does not appear in the potential energy. To find an extremum of the Lagrangian, L, corresponds to obtaining the eigenvalue and the associated eigenfunction of the linear modes. This principle is implemented in the stability analysis part of the STEP code. By applying the stellarator ordering to the potential energy δW, we can eliminate definitely stable modes such as the fast magnetosonic wave and the acoustic wave. As a result, we have the form of the Lagrangian,

$$\begin{aligned} L &= \frac{\gamma^2}{2}\int_p \rho_m \mid \boldsymbol{\xi}^{(0)} \mid^2 dV \\ &\quad -\frac{1}{2}\int_p dV[\mid \mathbf{Q}_\perp^{(2)} \mid^2 + \mathbf{J}_\parallel^{(2)} \times \boldsymbol{\xi}_\perp^{(0)} \cdot \mathbf{Q}_\perp^{(2)} + \boldsymbol{\xi}_\perp^{(0)} \cdot \nabla P^{(2)} \boldsymbol{\xi}_\perp^{(0)} \cdot \nabla \Omega^{(2)}] \\ &\quad + \int_v dV \mid \delta \mathbf{B}^{(2)} \mid^2 . \end{aligned} \tag{5.118}$$

Here the displacement vector in the plasma region is

$$\boldsymbol{\xi}_\perp^{(0)} = \hat{\zeta} \times \nabla_\perp \lambda, \tag{5.119}$$

and the perturbed magnetic field is

$$\mathbf{Q}_\perp^{(2)} = \hat{\zeta} \times \nabla \Sigma \tag{5.120}$$

$$\Sigma \equiv \left(\frac{B_0}{R_0} \frac{\partial}{\partial \zeta} + \nabla \zeta \times \nabla \Psi_{eq} \cdot \nabla \right) \lambda, \tag{5.121}$$

where λ corresponds to the stream function in the reduced MHD equations. The quantities with suffix (0) belong to $O(\delta^0)$ and these with suffix (2) belong to $O(\delta^2)$. Therefore potential energy corresponds to $O(\delta^4)$. In the vacuum region,

$$\delta \mathbf{B}^{(2)} = \hat{\zeta} \times \nabla \alpha, \tag{5.122}$$

where α is obtained from the equation,

$$\nabla \times \delta \mathbf{B}^{(2)} = 0, \tag{5.123}$$

with the boundary conditions,

$$\begin{cases} \alpha = \Sigma & \text{at the plasma-vacuum boundary} \\ \alpha = 0 & \text{at the conducting wall} \end{cases} \tag{5.124}$$

In the 'Stability' part of the STEP code, the PEST coordinate system $(\Psi_{eq}, \theta, \zeta)$ with the Jacobian(5.83) explained in Sec.5.4 is employed. A mapping calculation is carried out to construct this coordinate system from the equilibrium quantities in the rectangular coordinates obtained in the 'Equilibrium' part of the STEP code. The same mapping is used in the initial value problem approach for studying the linear MHD stability with the RESORM code. For the calculation of eigenvalue and eigenfunction in the 'Stability' part of the STEP code, the Galerkin method is employed in the Ψ_{eq}-direction and the Fourier expansion in the θ and ζ direction. Then the growth rate is obtained by solving the eigenvalue problem of the matrix form and the positive eigenvalues correspond to instabilities. This numerical scheme to obtain eigenvalues in the matrix form has an advantage to find all eigenvalues principally for a given equilibrium. However, this procedure cannot be applied to the resistive stability problem straightforwardly, because it is based on the property that the energy principle is hermitian.

5.8 Conclusion

We have derived the reduced MHD equations to describe dynamics of stellarator plasmas based on the stellarator ordering. Without the expansion for R/R_0, we can include higher order toroidal corrections with small changes of the reduced equations in the large aspect ratio limit. This is called the improved stellarator expansion. In the derivation of the three-field equations (5.52) $\sim$ (5.54) the essential procedure is the averaging of the short wave length components over the helical period in the ζ-direction. This means that we consider average effects of rapidly oscillating quantities on the long wave length phenomena.

By using $\partial/\partial t = u = 0$ in the reduced MHD equations and assuming that the equilibrium is axisymmetric in the lowest order, the Grad-Shafranov type equation for the static equilibrium (5.64) is obtained. This equation can be solved by the 'Equilibrium' part of the STEP code.

Based on the rotational transform depending on the flux function given by (5.73), we have introduced the flux coordinates (ρ, θ, ζ), where a line of force on the flux surface is expressed as a straight line with a gradient of ι to the ζ-direction. Using the linearized reduced MHD equations (5.92) $\sim$ (5.94) in this flux coordinates, we have developed the RESORM code to study the linear stability for both the ideal and resistive modes. By employing the flux coordinates, the $\mathbf{B} \cdot \nabla$ operator can be calculated accurately. Numerical procedures in the RESORM code were explained briefly. In the θ and ζ direction Fourier expansions are used and in the ρ direction a finite difference

approximation is used. Since our concern is in the linear stability, we can assign the toroidal mode number, n, in the code. Mode coupling between the different poloidal modes appears from the toroidal geometry where the equilibrium quantities depend on the θ coordinate.

In order to compare the ideal stability result by the RESORM code to that by other independent code, we choose the 'Stability' part of the STEP code using the eigenvalue problem approach based on the energy principle.

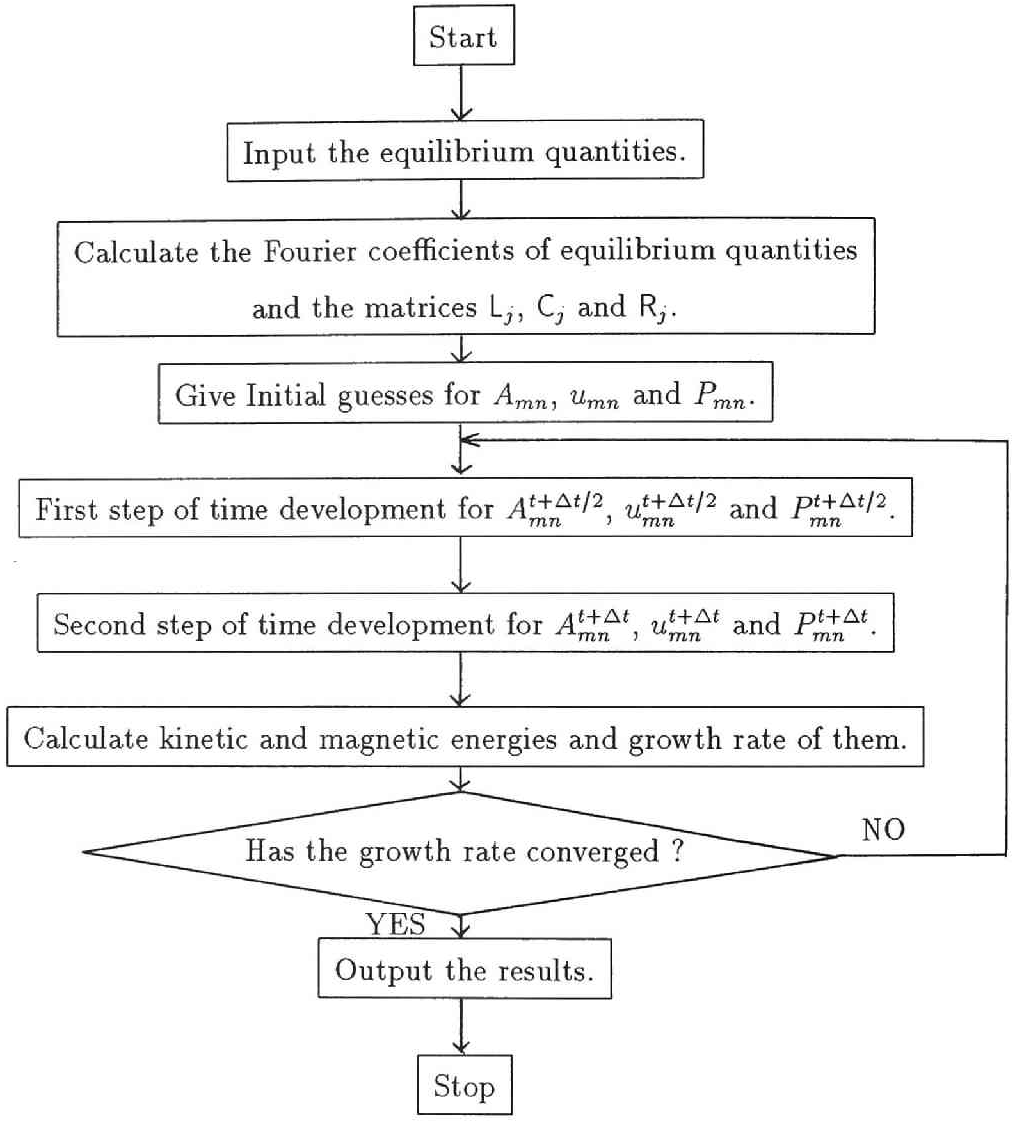

Fig.5.1 Flow chart of the RESORM code.

Chapter 6

MHD Beta Limit Study of Heliotron DR

6.1 Introduction

Recently finite beta currentless plasmas were produced in Heliotron DR by the second harmonic electron cyclotron resonance heating (ECRH) at the central magnetic field of $B_0 \simeq 0.5$T. It has an $\ell = 2$ and $M = 15$ helical winding, where M is a period of helical magnetic field. The major radius is 90cm and the average minor radius, $\bar{a}$, is 7.8cm by the line tracing calculation. It is reported that low frequency fluctuations appear in the soft X ray measurement and the poloidal magnetic field measurement at $\bar{\beta} \simeq 0.5\%$ [57]. They look similar to those observed in the Heliotron E high beta experiment[2]. It is an interesting subject whether the same type of

pressure-driven instabilities plays a role in Heliotron DR as in Heliotron E or not. We apply the RESORM code explained in Chapter 5 to Heliotron DR for studying the resistive mode behaviors and the relation to the ideal pressure-driven mode [50]. For comparison we also use the STEP code for the ideal instabilities.

In Sec.6.2, we discuss properties of currentless equilibrium in Heliotron DR by using the 'Equilibrium' part of the STEP code. Particularly we pay attention to effects of finite beta on the rotational transform, the shift of the magnetic axis and the magnetic well. By using the RESORM code we study the ideal MHD stability of the equilibria obtained by the STEP code in Sec.6.3. The 'Stability' part of the STEP code is also used for the check and comparison with the RESORM code results. In Sec.6.4, the results of the resistive MHD stability of the Heliotron DR plasma by the RESORM code are presented. By comparing the numerical results with the analytic expressions in the cylindrical geometry by Johnson, Greene and Coppi [58], S-dependence of the mode and the relation between the resistive and ideal modes are intensively discussed. In Sec.6.5, the effects of the additional vertical field producing the magnetic axis shift in the vacuum flux surfaces on both the resistive and the ideal instabilities are investigated. Conclusions are given in Sec.6.6.

6.2 Currentless equilibria in Heliotron DR

Heliotron DR device belongs to the $\ell = 2$ helical system of which magnetic coil parameters are shown in Table 6.1[59]. By applying the Biot-Savart law to the Heliotron DR device with an approximation of filamentary current we can calculate the vacuum magnetic field and the flux surfaces are shown in Fig.6.1. This case is called the standard configuration of Heliotron DR. In order to obtain the currentless equilibrium of Heliotron DR plasma, we solve eq.(5.64) by applying the 'Equilibrium' part of the STEP code. As mentioned in Chapter 5, Ψ_v and Ω are obtained from the vacuum magnetic fields with the parameters in Table 6.1. Because Heliotron DR has an aspect ratio of 13, we use the expression for Ω in the large aspect ratio limit

$$\Omega = \frac{2x}{R_0} + \frac{\overline{|\mathbf{B}_\delta|^2}}{B_0^2}. \tag{6.1}$$

In the STEP code the plasma position is also controlled by the external vertical magnetic field, $B_\perp$. For the standard configuration, we use $B_\perp$ to adjust the center of the finite beta plasma to the central position of the outermost vacuum flux surface.

Relying on the experimental data that the toroidal plasma current is negligibly small for the finite beta plasma, we calculate MHD equilibria under the currentless constraint rather than the FCT condition. We use the following pressure profile as the standard one,

$$P(\Psi_{eq}) = P_0(1 - \Psi_{eq})^2, \tag{6.2}$$

which seems to be consistent with that estimated from the diamagnetic measurements and the soft X ray radiation profiles[59].

Figure 6.2 shows the profiles of the pressure $P(\Psi_{eq})$, and the rotational transform $\iota(\Psi_{eq})$ versus average radius, $\bar{r}/\bar{a}$, where $\bar{a}$ denotes the average minor radius, for several beta values at the magnetic axis, β_0. For $\beta_0 = 0.0\%$ (vacuum case), the rotational transform varies from $\iota(0) = 0.8$ at the axis to $\iota(\bar{a}) = 1.84$ at the edge. As beta increases, $\iota(0)$ increases, while $\iota(\bar{a})$ decreases. This is the general tendency of rotational transform profile for the finite beta currentless plasmas in $\ell = 2$ heliotrons/torsatrons as shown in Chapter 3. However, the decrease of $\iota(\bar{a})$ is very small in Heliotron DR as shown in Fig.6.2. Each case includes the $\iota = 1$ surface which is susceptible to the instability with $n/m = 1$, particularly $m = 1$ and $n = 1$, where m and n are poloidal and toroidal mode number, respectively.

The Shafranov shift of the magnetic axis, $\Delta/\bar{a}$, is shown in Fig.6.3 for the pressure profile of (6.2). For the comparison, we also calculated the currentless equilibrium of Heliotron E plasma by using the STEP code with the same pressure profile as eq.(6.2). Since the vacuum rotational transform of Heliotron DR at the axis is larger than that of Heliotron E, which is about 0.5 from the line tracing of the vacuum field [41], the shift of the magnetic axis in Heliotron DR is smaller than that of Heliotron E for the same pressure profile and the same beta value. The larger aspect ratio of Heliotron DR may enhance the difference. This axis shift is directly related to formation of the magnetic well. Figure 6.4 shows the magnetic well region defined by $V'' < 0$ in the plasma column and the position of the $\iota = 1$ surface with white circles in the $(\beta_0, \bar{r}/\bar{a})$ plane, where $V'(\Phi)$ denotes the specific volume defined by

eq.(5.74). While the magnetic hill spreads over the whole plasma at the low beta case, the region of the magnetic well expands from the central region as the beta increases. However, the smallness of the axis shift in Heliotron DR prevents the formation of the substantial well until $\beta_0 \gtrsim 1\%$. It is noted that the $\iota = 1$ surface does not belong to the magnetic well region. This fact suggest that a global instability with $m = 1$ and $n = 1$ resonant at $\iota = 1$ may appear.

6.3 Ideal pressure-driven modes

In the currentless equilibria of Heliotron DR plasma, it is considered that the pressure driven interchange mode is the most crucial instability, because they have the wide magnetic hill region. First, we study the stability against the ideal global modes by using the RESORM code. For the toroidal mode number n, we choose from $n = 1$ to $n = 3$, and for each n poloidal modes with $n - 3 \leq m \leq n + 3$ are included in the stability calculation. It is found that the modes resonant at the $\iota = 1$ surface with the low mode numbers (m, n) = (1,1), (2,2) and (3,3) become unstable at the lowest beta value, although the RESORM and the STEP codes cannot treat high n modes principally. Figure 6.5 shows the growth rate of these modes as a function of β_0. For comparison, the growth rates of the (1,1) mode with the STEP code are plotted and they show reasonable agreement with the results by the RESORM code. The reason why the growth rates given by the RESORM code are a little smaller than those given by the STEP code may be considered that the higher order toroidal corrections in the reduced equations (5.92)~(5.94) which are not included in the STEP code have a stabilizing effect on the pressure-driven modes. In both codes radial mesh number of 192 is assigned in the calculation for the (1,1) mode. For the other modes we used 96 meshes, because the growth rates calculated with the RESORM code are almost independent of the radial mesh number for $1.5\% \lesssim \beta_0 \lesssim 3\%$ in the Heliotron DR case from the convergence study. Profiles of the (1,1) mode eigenfunction obtained by the RESORM code, u_{11}, are shown at two

beta values in Fig.6.6. In Fig.6.5, the beta limit of the standard Heliotron DR configuration is $\beta_0 \simeq 1.2\%$. Although the growth rate becomes larger for the higher n mode, the growth rates of the three modes shown in Fig.6.5 become marginal at the almost same critical beta value. This limit does not change even for the free boundary stability calculation[57] because the mode structure becomes strongly localized in the neighborhood of the singular surface at the beta value just above the critical beta, which is not affected by the free boundary condition. This tendency is also seen in Fig.6.6.

It is generally true that the eigenfunction of the interchange mode is localized at the singular surface. However, when two singular surfaces appear for a single helicity, the mode localization depends on the negative contribution to the potential energy at each singular surface. In the currentless equilibrium, the central rotational transform increases according to the increase of β and two $\iota = 1$ surfaces can be realized in Heliotron DR and Heliotron E. For the latter case there is an example of (m, n)=(1,1) mode localized near the magnetic axis[60]. For Heliotron DR, the beta value at which two $\iota = 1$ surfaces appear is higher than that in Heliotron E and it is beyond our interesting regime of beta value.

The beta limit for the localized mode in the ideal MHD stability is given by the Mercier criterion, which is derived from the potential energy for ideal pressure-driven instability in the limit that the mode is highly localized at the rational surface as discussed in Sec.4.C. The explicit expression consistent with the stellarator ordering is written in the form[15],

$$
\begin{aligned}
D_I \;=\; & -\frac{4\pi^2 p' \iota^4}{\iota'^2}\left\langle \frac{B^2}{\mid \nabla\Psi \mid^2}\right\rangle \left[\frac{(\iota V')'}{2\pi\iota} - p'\left\langle \frac{1}{B^2}\right\rangle \right. \\
& + \frac{R_0 \iota'}{B_0 \iota^2}\left(\frac{\langle \Omega B^2/\mid \nabla\Psi \mid^2\rangle}{\langle B^2/\mid \nabla\Psi \mid^2\rangle} - \frac{\langle \Omega B^2\rangle}{\langle B^2\rangle}\right) \\
& \left. + \frac{4\pi^2 R_0^2 p'}{B_0^2}\left(\frac{\langle \Omega B^2/\mid \nabla\Psi \mid^2\rangle^2}{\langle B^2/\mid \nabla\Psi \mid^2\rangle} - \left\langle \frac{\Omega^2 B^2}{\mid \nabla\Psi \mid^2}\right\rangle\right)\right] - \frac{1}{4}, \qquad (6.3)
\end{aligned}
$$

where the bracket $\langle f\rangle$ means the flux surface average and prime denotes the Ψ-derivative. Here $D_I < 0$ corresponds to the stable region. Figure 6.7 shows that the Mercier unstable region expands in the plasma column as the beta value increases. In the region near the magnetic axis, the Mercier criterion becomes unstable for $\beta_0 \gtrsim 0.3\%$ because of the weakness of the stabilizing effect due to the magnetic well in the standard Heliotron DR configuration as shown in Fig.6.4. On the other hand the stable region near the edge is attributed to the magnetic shear and the small pressure gradient. At the $\iota = 1$ surface whose position is shown by white circles in Fig.6.7 D_I becomes positive (or unstable) at $\beta_0 \simeq 0.7\%$ which is lower than the critical beta value determined by the global modes (see Fig.6.5). In other words, the Mercier criterion gives the more severe limit for the beta value than the low n mode stability. This difference comes from the numerical resolution associated with finite mesh size[61]. For $0.7\% < \beta_0 < 1.2\%$, there may be an unstable mode with strongly localized at the resonant surface which cannot be obtained by the RESORM or the STEP codes. However, the localized modes with very small growth rates may not disturb the plasma significantly in the ideal MHD model.

6.4 Resistive pressure-driven mode

We study resistive modes in the Heliotron DR configuration by using the initial value problem code, RESORM code. In the resistive MHD stability calculation, magnetic Reynolds number S is needed as the input parameter. In Heliotron DR, plasma production and heating are possible only by ECRH. For such an ECRH produced currentless plasma, we typically obtained the electron temperature $T_e \simeq 300\text{eV}$ and the mean particle density $\bar{n} \simeq 2 \times 10^{19}\text{m}^{-3}$, at the central magnetic field $B_0 = 0.5\text{T}$, and hence, $S \sim 10^5$.

Figure 6.8 shows the beta dependence of the growth rates of global resistive modes with toroidal mode numbers $n = 1$, $n = 2$, and $n = 3$ for $S = 10^5$. The poloidal modes with $n - 3 \leq m \leq n + 3$ are also included in the RESORM code for each n. The same in the ideal case, the modes with (1,1), (2,2), and (3,3) resonant at the $\iota = 1$ surface are dominant in Fig.6.8. The growth rates of the $n = 1$ mode for $S = 10^3$, 10^4, 10^5, and 10^6 are shown in Fig.6.9 and those of the $n = 1$ ideal mode are plotted for comparison. For all S values, the unstable modes with significant growth rates exist at the lower beta value than the ideal limit, $\beta_0 = 1.2\%$. It is true that there is no unstable mode at $\beta_0 = 0.0\%$; however, the resistive unstable modes survive until $\beta_0 \sim 0\%$ within the incompressible MHD model. In $S = 10^6$ case, where the resistivity is relatively small, the growth rates of the $n = 1$ resistive mode are a little larger than those of the ideal $n = 1$ mode for $\beta_0 > 1.2\%$ and they decrease gradually for $\beta_0 < 1.2\%$. On the other hand, beta dependence for $S = 10^3$, is quite different from the ideal case. The growth rates of resistive

modes are much larger than those of ideal modes.

In the cylindrical geometry, we can estimate the growth rate of the resistive interchange mode analytically by following the analysis given by Johnson, Greene and Coppi (JGC) [58]. The resistive mode with the mode number (m, n) is assumed localized within the resistive layer around the singular surface, $r = r_s$, where,

$$\iota(r_s) = \frac{n}{m}, \tag{6.4}$$

and in the outer region far from the singular surface the resistivity can be neglected. Since the thickness of the resistive layer $|r - r_s|$ is approximated by the resistive skin depth, we can employ the ordering,

$$|r - r_s| \sim \gamma \sim \eta^{1/3} \sim \hat{\epsilon}, \tag{6.5}$$

where $\hat{\epsilon}$ is the small ordering parameter. Noting that the equilibrium quantities depend on only r, and assuming that A_{mn}, u_{mn} and P_{mn} are the same order and $\partial/\partial r \sim \hat{\epsilon}^{-1}$, the reduced equations (5.101)$\sim$(5.103) are written by

$$\gamma A_{mn} = -m(r - r_s)\iota' u_{mn} + \frac{1}{S}\frac{d^2 A_{mn}}{dr^2} \tag{6.6}$$

$$\gamma \frac{d^2 u_{mn}}{dr^2} = m(r - r_s)\iota' \frac{d^2 A_{mn}}{dr^2} - m^2 \iota'^2 \frac{D_s u_{mn}}{\gamma}. \tag{6.7}$$

Here P_{mn} has been eliminated by substituting eq.(5.103) into eq.(5.102), and

$$\mathbf{B} \cdot \nabla \simeq (r - r_s) \left.\frac{d\iota}{dr}\right|_{r=r_s} \frac{d}{d\theta}, \tag{6.8}$$

and

$$D_s = -\frac{\beta_0}{2\epsilon^2 r_s^2 \iota'^2} \frac{d\Omega_{eq}}{dr} \frac{dP_{eq}}{dr}, \tag{6.9}$$

are used.

are used.

By considering the dimension we can replace the stream function u_{mn} by the displacement ξ as

$$u_{mn} = -\gamma\xi. \tag{6.10}$$

With the normalizations

$$\gamma = \left(\frac{m^2 t'^2}{S}\right)^{1/3} Q \tag{6.11}$$

$$|r - r_s| = (Sm t')^{-1/3} X \tag{6.12}$$

$$A_{mn} = \left(\frac{m^2 t'^2}{S}\right)^{-1/3} \psi, \tag{6.13}$$

we obtain the eigenvalue equations from eqs.(6.6) and (6.7),

$$\psi'' = Q(\psi - X\xi) \tag{6.14}$$

$$Q^2\xi'' = -D_s\xi - X\psi'', \tag{6.15}$$

which are the same equations derived by JGC [58], where primes denote the derivative with respect to X.

When the Fourier transform defined by

$$\hat{\xi}(k) = \frac{1}{2\pi}\int_{-\infty}^{+\infty} \xi(X)\exp(-ikX)dX, \tag{6.16}$$

is used, the eigenfunction of eqs. (6.14) and(6.15) has the form of series expansion with respect to k,

$$\hat{\xi}(k) = k^N \exp\left(-\frac{1}{2}Q^{1/2}k^2\right)\sum_{j=0}^{n} a_j k^{2j}. \tag{6.17}$$

Then the eigenvalue

$$Q^{3/2} = \frac{D_s}{N + 2n + \frac{1}{2} + \left[4Nn + \left(2n + \frac{1}{2}\right)^2\right]^{1/2}}, \tag{6.18}$$

is obtained, where

$$N = -\frac{1}{2} + \frac{1}{2}(1 - 4D_s)^{1/2}. \tag{6.19}$$

Equation (6.18) implies that $Q^{3/2}$ becomes positive when D_s is positive, and this means that the instability is driven by the pressure gradient in resistive plasma. Therefore, this mode is called resistive interchange mode or g mode. From eq.(6.11), we find that the growth rate is proportional to $S^{-1/3}$. Based on the ordering of eq.(6.5) JGC showed that the eigenfunction $\xi(X)$ of the g mode in the real space decays rapidly in the large X region. The eigenvalue is determined by the matching condition of the resistive layer solution in the large X region with the asymptotic solution from the outer region to the singular surface. For the resistive interchange mode, there are two types of parity with respect to the singular surface, 'EVEN' mode and 'ODD' mode. Here the former means that ξ is even and ψ is odd, the latter is that ξ is odd and ψ is even. It is remarked that the unstable mode produces the magnetic island in the neighborhood of $r = r_s$ when ψ is even. By extending this analysis Glasser, Greene and Johnson [49] derived the GGJ criterion for the resistive interchange and tearing modes.

To compare the unstable modes obtained by the RESORM code with the analytic results, we examine the S-dependence of the growth rates and the radial mode structure. Fig.6.10 shows the S-dependence of the (1,1) mode at the several beta values. In the case of $\beta_0 = 0.5\%$, where the ideal

mode is completely stable, the growth rates are proportional to $S^{-1/3}$ clearly. This mode is considered as the pure resistive interchange mode. As the beta increases, the deviation from the $S^{-1/3}$ dependence becomes large. It is considered that the ideal instability affects the resistive interchange mode growth rate. Deviations already appear at $\beta_0 = 0.7\%$ and 1.0%, where there is no unstable ideal global mode by both the RESORM and the STEP codes. As discussed in Sec.6.3, these beta values belong to the marginal unstable region with very small growth rates. Therefore, the properties of the low n resistive mode are changed by the ideal instability effect in the Mercier unstable region ($\beta_0 \gtrsim 0.7\%$) even if it is difficult to obtain the ideal interchange instability by the numerical calculation. In Fig.6.11, we show the eigenfunctions $u_{m1}(\rho)$ and $A_{m1}(\rho)$ of the unstable $n = 1$ mode at $S = 10^5$ and $\beta_0 = 2.0\%$. The u_{11} profile localized around the $\iota = 1$ surface has the even mode structure, and the A_{11} profile shows the odd mode structure. They coincide with the 'EVEN' mode in the resistive interchange mode theory by JGC. There is no change of these mode structures from $\beta_0 = 0.5\%$ to $\beta_0 = 3\%$. The similar mode structures are also obtained in the case of $n = 2$ and $n = 3$.

6.5 Effects of magnetic axis shift on ideal and resistive MHD stabilities of Heliotron DR

It is known that formation of magnetic well or hill depends on the position of magnetic axis in heliotron/torsatron configurations as discussed in Chapter 3 [40,42]. By controlling magnitude of vertical magnetic field, the magnetic axis position changes easily in the vacuum magnetic configuration. On the other hand, in finite beta plasmas, the Shafranov shift occurs due to the Pfirsch-Schlüter current. It makes outward shift of the plasma column which is favorable for deepening the magnetic well.

In order to obtain an equilibrium with the additional vertical field, the 'Equilibrium' part of the STEP code is used to solve the equation,

$$\Delta^*(A - A_{av}) = -R_0^2 \frac{dP}{d\Psi}\Omega + G, \tag{6.20}$$

where $2\pi A_{av}$ denotes the poloidal flux generated by the additional vertical field. Then, the vertical field $B_{av}\mathbf{e}_Z$ is written by

$$\nabla_\perp A_{av} \times \nabla\zeta = B_{av}\mathbf{e}_Z. \tag{6.21}$$

By integrating (6.21) with the boundary condition, $A_{av}(R = R_0) = 0$,

$$A_{av} = \frac{(R^2 - R_0^2)}{2} B_{av} \tag{6.22}$$

is obtained. The magnitude of the vertical field B_{av} is used as the input parameter in the STEP code.

Figure 6.12 shows the changes of rotational transform profile due to the magnetic axis shift in the vacuum configuration. It is seen that the new resonant surface of $\iota = 4/5$ appears at the axis and the $\iota = 1$ surface moves to the outer region with inward shift of $\Delta_v = -0.79$cm, where Δ_v denotes the shift of the magnetic axis at $\beta = 0$ from the position of the standard configuration. While, in the outward shift case of $\Delta_v = +0.73$cm, the $\iota = 1$ surface moves to the inner region. Figure 6.13 shows the change of the rotational transform due to finite beta effects. In the case of $\Delta_v = -0.79$cm, the change of $\iota(0)$ is smaller than that in the standard configuration with $\Delta_v = 0$, while it is larger for the outward shift case of $\Delta_v = +0.73$cm. Figure 6.14 shows the magnetic well (or hill) region for the cases of $\Delta_v = -0.79$cm and $\Delta_v = +0.73$cm in the $(\beta_0, \bar{r}/\bar{a})$ plane. By comparing with Fig.6.4 for the standard case, it is seen that the magnetic well region expands for $\Delta_v > 0$, while it shrinks for $\Delta_v < 0$.

STEP code results for the ideal linear stability under the free boundary condition are given in Fig.6.15 with the same pressure profile $P = P_0(1-\Psi_{eq})^2$ as in eq.(6.2) . Here our concern is in the most unstable mode for various Δ_vs. The $\iota = 4/5$ surface appeared for $\Delta_v \lesssim -0.39$cm destabilizes the $n = 4$ mode strongly and the beta limit decreases by the increase of the inward shift. On the other hand, for $\Delta_v \geq 0$ the $m = 1$ and $n = 1$ mode resonant at the $\iota = 1$ surface is the dominant mode; however, there is no stabilizing tendency with the increase of $\Delta_v > 0$, because the $\iota = 1$ surface moves inward and the pressure gradient becomes larger than that in the standard case at a fixed beta value under the same pressure profile.

Figure 6.16 shows growth rates of resistive mode as a function of central

beta value for several Δ_vs at $S = 10^5$. There is a destabilizing tendency for $\Delta_v = -0.79$cm and a stabilizing tendency for $\Delta_v = +0.73$cm, which is consistent with the expectation from the MHD theory. By the increase of the outward shift, the growth rate of the $m = 1$ and $n = 1$ mode becomes smaller than that in the standard case or $\Delta_v = 0$. However, the difference of the growth rates between $\Delta_v = 0$ and $\Delta_v = +0.73$cm is very small for $\beta_0 < \beta_{0c}$ given in Fig.6.15. The $n = 4$ mode resonant at $\iota = 4/5$ is the new strong instability and it may enhance magnetic fluctuations in experiments with the inward shift of the magnetic axis. In this case, at $\beta_0 \lesssim 1.5\%$ the dominant mode (m, n) is (5,4), however, the dominant mode changes to (4,4) at $\beta_0 \gtrsim 2\%$. By comparing this result with Fig.6.14(a), it is found that the resistive interchange mode resonant at the $\iota = 4/5$ surface is stabilized by the magnetic well as β_0 increases, and the mode resonant at $\iota = 1$ surface in the outer region becomes dominant. This transition also can be seen in the corresponding eigenfunctions in Fig.6.17.

6.6 Conclusion

We have investigated both the ideal and resistive instabilities in Heliotron DR plasmas by using the STEP code and the RESORM code.

First, we calculated the vacuum magnetic field from the coil configuration of Heliotron DR based on the Biot-Savart law, and then, averaged it in the toroidal direction to obtain the vacuum poloidal flux, Ψ_v, and the curvature Ω. By using the 'Equilibrium' part of the STEP code, in which Ψ_v and Ω are used as input parameters, we obtained the currentless equilibrium of the standard case for the pressure profile of $P = P_0(1 - \Psi_{eq})^2$ which describes reasonably the experimental pressure profile. The rotational transform varies from $\iota(0) = 0.8$ at the magnetic axis to $\iota(\bar{a}) = 1.84$ at the outermost surface in the vacuum case. However, $\iota(0)$ increases and $\iota(\bar{a})$ decreases as beta increases under the constraint of currentless equilibrium. Since $\iota(0)$ at $\beta = 0$ and the aspect ratio are larger than those of Heliotron E, the Shafranov shift of the magnetic axis is smaller than that of Heliotron E. If we compare the Shafranov shift of Heliotron E by the STEP code with that by the BETA code shown in Fig.3.3, it is seen that the BETA code gives a little smaller Shafranov shift. This difference comes from the assumption for the Heliotron E configuration in the BETA code, where we carefully treated the inside region including the $\iota = 1$ surface. It can be understandable from the analytic expression of Shafranov shift.

In the Heliotron DR equilibrium of the standard configuration, since the $\iota = 1$ surface always exists even for finite beta plasmas, the mode resonant

there becomes the most unstable one. We have examined the ideal stability of the several currentless equilibria in the standard configuration by using both the STEP code and the RESORM code with zero resistivity. They show reasonable agreement each other for the growth rate of the same ideal interchange mode. The critical beta value against the ideal global modes is $\beta_0 \simeq 1.2\%$. However, the Mercier criterion indicates the lower beta limit, $\beta_0 = 0.7\%$, than that by the global modes. It is considered that the equilibrium is marginally unstable in the region of $0.7\% \lesssim \beta_0 \lesssim 1.2\%$ where the global modes are practically stable and the Mercier mode is unstable.

We have studied the resistive instability by applying the RESORM code to the equilibria in Heliotron DR. The resistive modes resonant at the $\iota = 1$ surface survive with substantial growth rates even for $\beta_0 < 1.2\%$. The $S^{-1/3}$ dependence of the resistive mode growth rate is clearly seen in the region where the Mercier mode is stable. However, in the Mercier unstable region of $\beta_0 > 0.7\%$ the resistive mode is modified by the ideal instability effect significantly.

The effect of the magnetic axis shift in the vacuum configuration on the MHD stability against the pressure-driven mode was also studied for Heliotron DR. From the numerical results, both inward and outward axis shift are destabilizing in the Heliotron DR due to the behaviors of the two resonant surfaces $\iota = 1$ and $\iota = 4/5$. In the inward shift case, the new resonant surface with $\iota = 4/5$ appears in the hill region and it destabilizes strongly both the ideal and resistive modes. In the outward shift case, the effect of the movement of the $\iota = 1$ surface to the region with the larger pressure gradient destabilizes the ideal mode and degrades the beta limit, although

the magnetic well region appears at the lower beta value than that in the standard case. The degradation of stability in the case of outward shift is a particular case. Usually a stabilizing tendency is seen in Heliotron E and Heliotron H as discussed in Chapter 3. The resistive modes in the outward shift case, however, are stabilized by the magnetic well a little, and the growth rates are smaller than those in the standard case.

It is noted that Galerkin method that is used in the STEP code is similar to the usual finite element approximation and the eigenvalue depends on the mesh size. Therefore the convergence check is important to judge whether the instability is true one or numerical one. Usually radial mesh number 192 is sufficient enough to decide the stability by the STEP code[60]. We also evaluated the mesh size dependence of the growth rate in the initial value code, RESORM code, by using N =96, 144, and 192, where N is the radial grid number. In the Heliotron DR configuration, the differences of the growth rates among the three cases are less than 1% in both the ideal and the resistive modes. On the other hand, in the application of the RESORM code to Heliotron E we found that the γ^2 is proportional to the $(1/N)^2$ and converges to a small growth rate. This different behavior of the convergence seems to come from the radial mode structure because this $(1/N)^2$ dependence is obtained for the ideal mode fairly localized near the resonant surface.

Table 6-1 Coil parameters of Heliotron DR

Helical winding		
Major radius	(R_0)	90cm
Minor radius	(a_h)	13.5cm
Number of poles	(ℓ)	2
Number of pitch	(M)	15
Number of turns	(n_h)	6

Vertical windings		
Radius	(R_v)	138cm
Height	(H_v)	$\pm$41.4cm

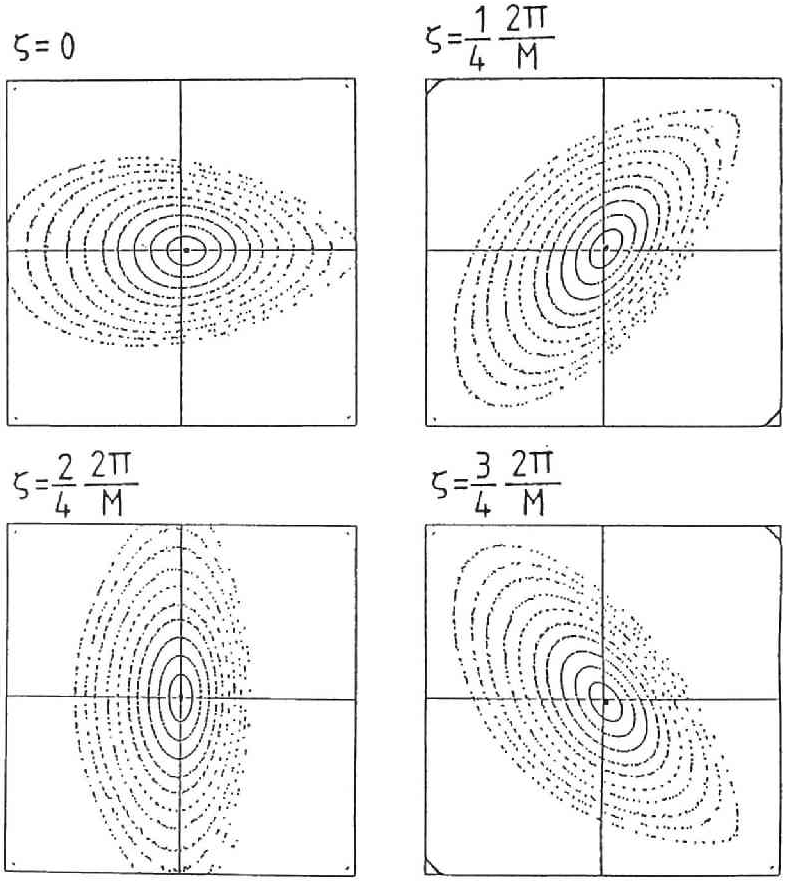

Fig.6.1 Vacuum flux surfaces at different cross-sections by line tracing calculation. The average minor radius, $\bar{a}$, is 7.8cm.

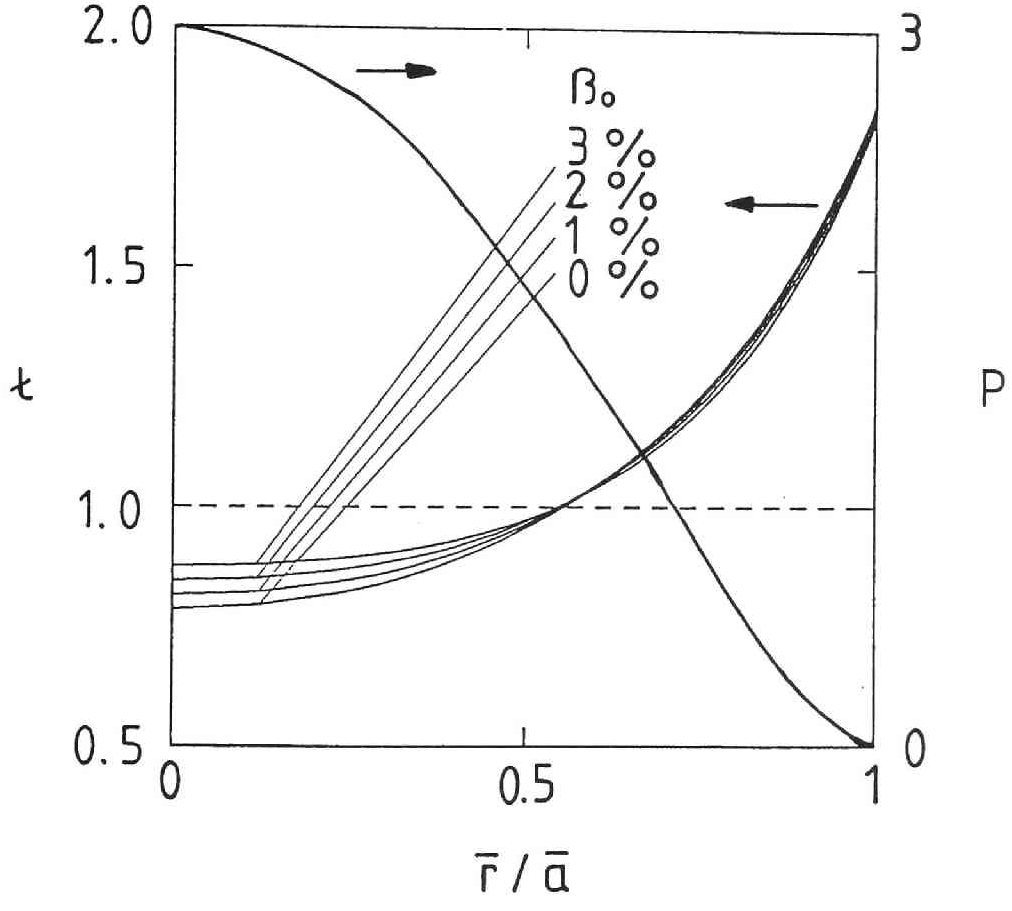

Fig.6.2 Pressure profile for $\beta_0 = 3\%$ and rotational transform profiles for $\beta_0 = 0\%$, 1%, 2% and 3%. $\bar{r}$ and $\bar{a}$ denote radius and average minor radius equal to 7.8cm, respectively.

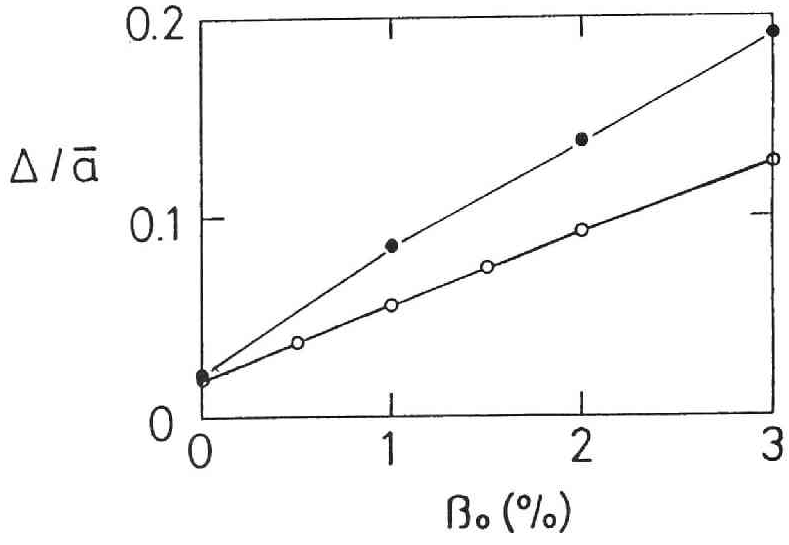

Fig.6.3 Magnetic axis position versus β_0; white circles show shift of magnetic axis in Heliotron DR, black circles show shift of magnetic axis in Heliotron E, by the STEP code.

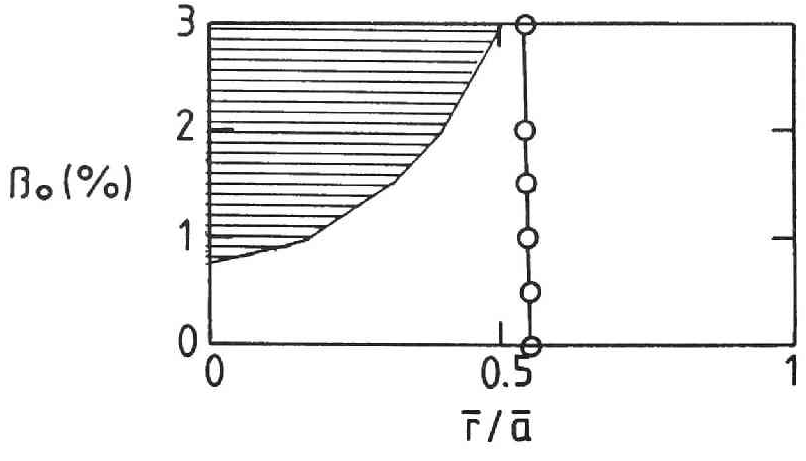

Fig.6.4 Boundary between the magnetic well and the magnetic hill is shown in $(\beta_0, \bar{r}/\bar{a})$ plane. Shaded region belongs to the magnetic well. $\iota = 1$ position is also shown with white circles.

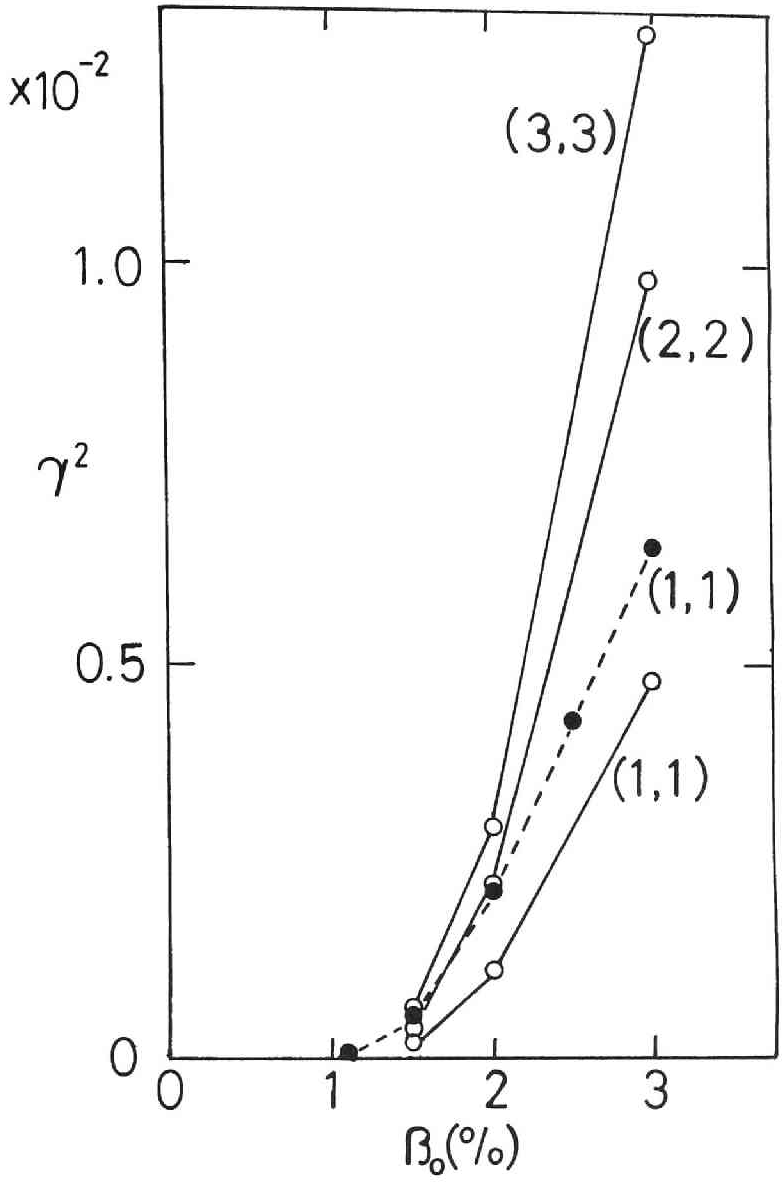

Fig.6.5 Growth rates of ideal pressure driven modes resonant at $\epsilon = 1$ surface. White circles correspond to the modes with (m, n) = (1,1), (2,2) and (3,3) obtained by the RESORM code and black circles correspond to the (1,1) mode obtained by the STEP code.

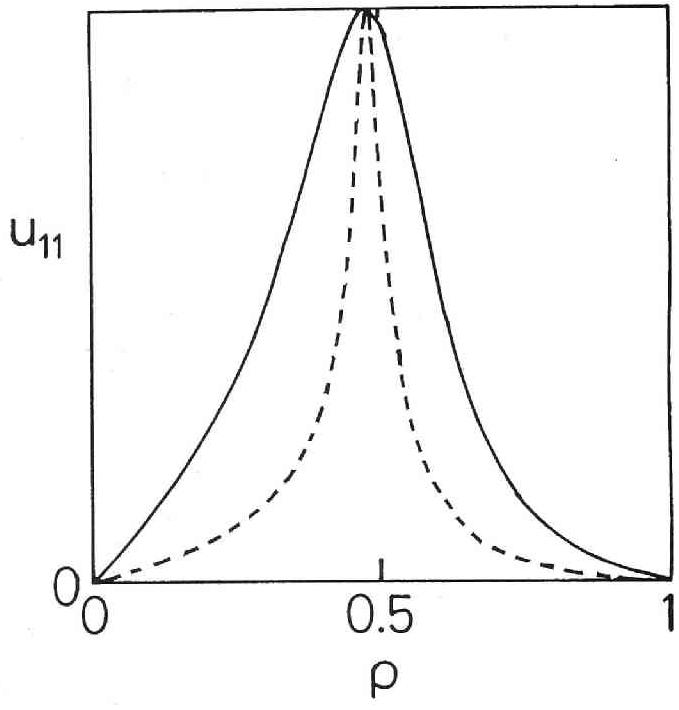

Fig.6.6 Eigenfunctions u_{11} of the $m = 1$ and $n = 1$ ideal mode for $\beta_0 = 1.5\%$ (dotted line) and $\beta_0 = 3\%$ (solid line) obtained by the RESORM code.

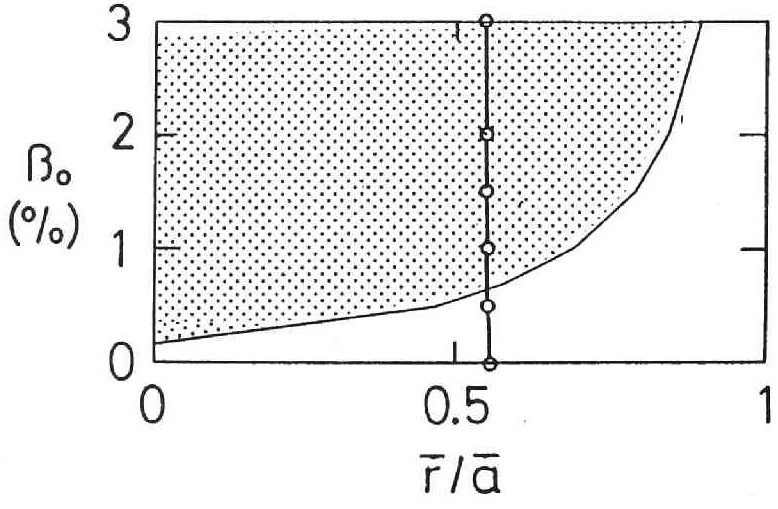

Fig.6.7 Mercier criterion in $(\beta_0, \bar{r}/\bar{a})$ plane. $\iota = 1$ position is also shown with white circles. Shaded region shows the Mercier unstable region.

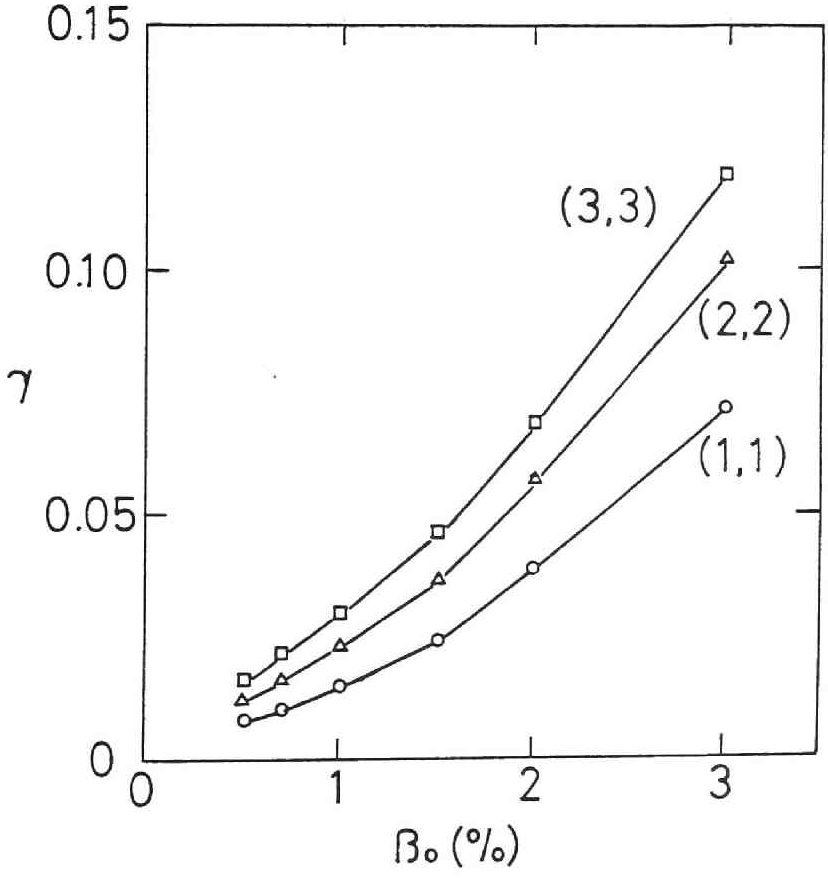

Fig.6.8 Growth rates of resistive pressure driven modes with $(m, n) =$ (1,1), (2,2) and (3,3) versus β_0 at $S = 10^5$.

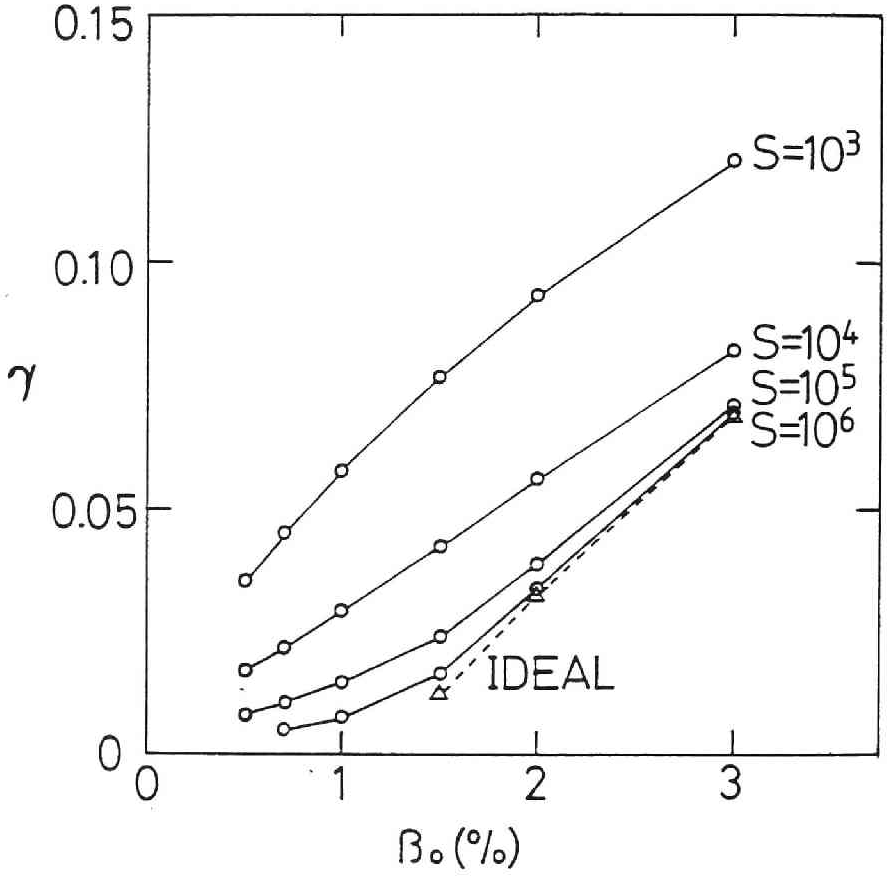

Fig.6.9 Growth rates of resistive pressure driven $n = 1$ modes versus β_0 for $S = 10^3$, 10^4, 10^5 and 10^6. Growth rates at $S = \infty$ or ideal case are shown for comparison by the dotted line.

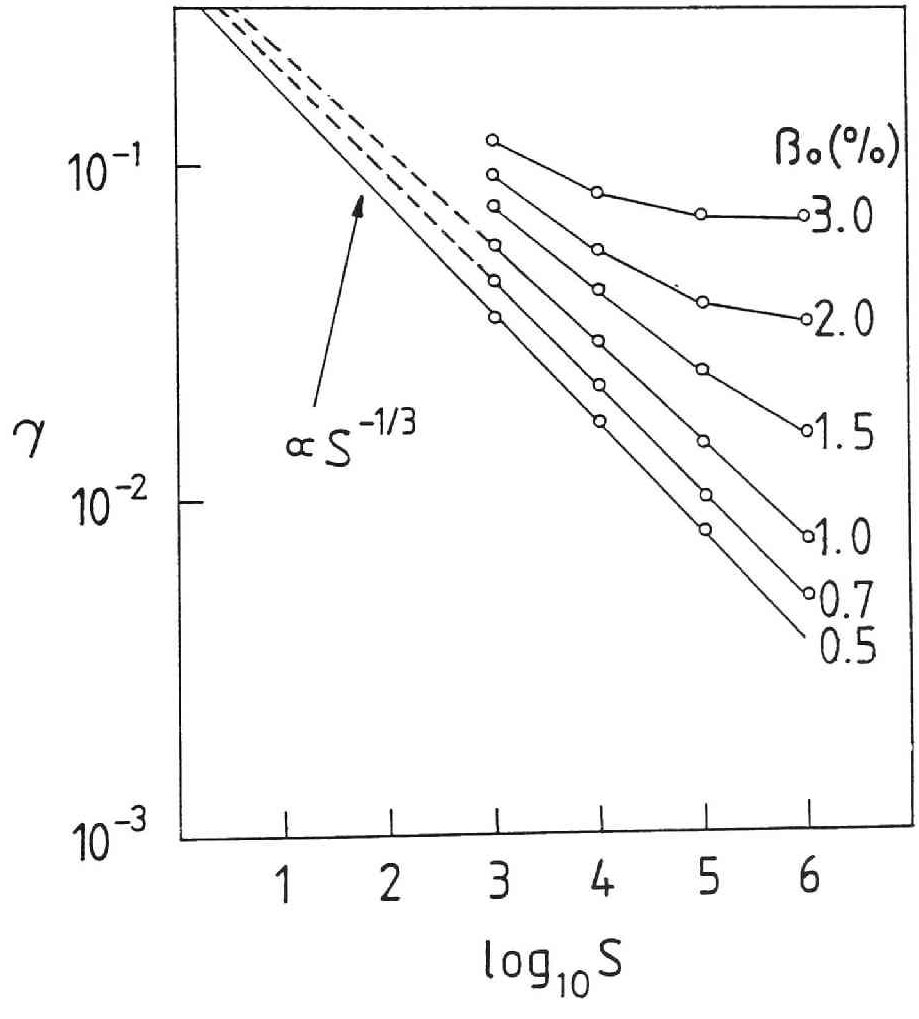

Fig.6.10 Dependence of the growth rate of the $n = 1$ mode on the magnetic Reynolds number S for various β_0 values.

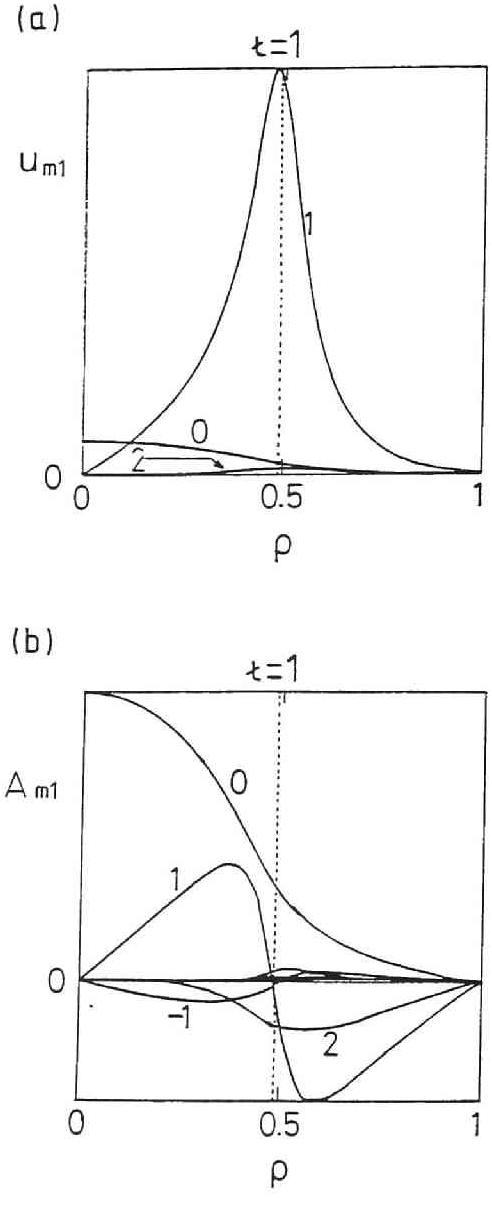

Fig.6.11 Eigenfunctions (a) $u_{m1}(\rho)$ and (b) $A_{m1}(\rho)$ of the $n = 1$ mode at $\beta_0 = 2\%$ and $S = 10^5$. The numbers denote the value of m .

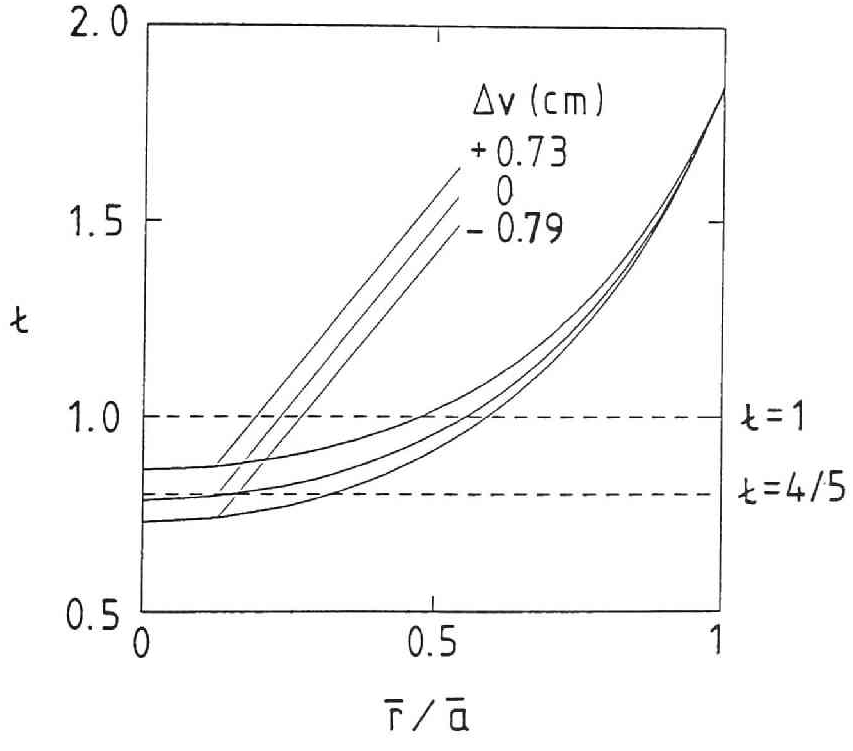

Fig.6.12 Variations of rotational transform due to the magnetic axis shift in the vacuum configuration.

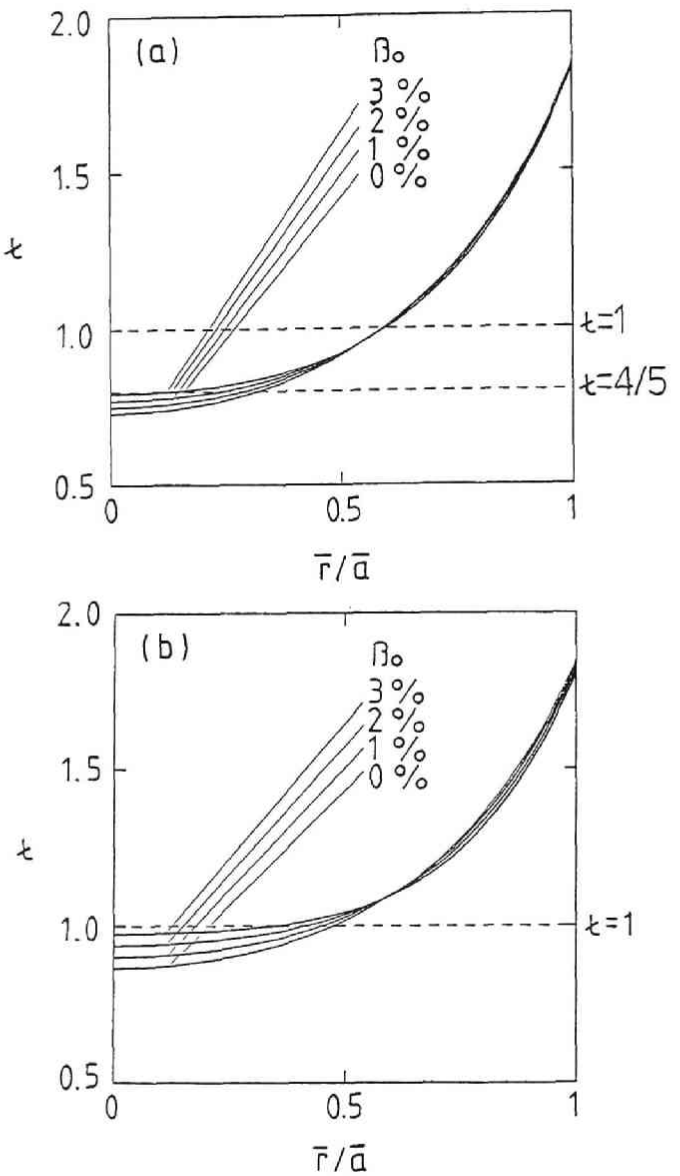

Fig.6.13 Variations of rotational transform due to finite beta effects for (a) inward shift case of $\Delta_v = -0.79$ cm and (b) outward shift case of $\Delta_v = +0.73$ cm.

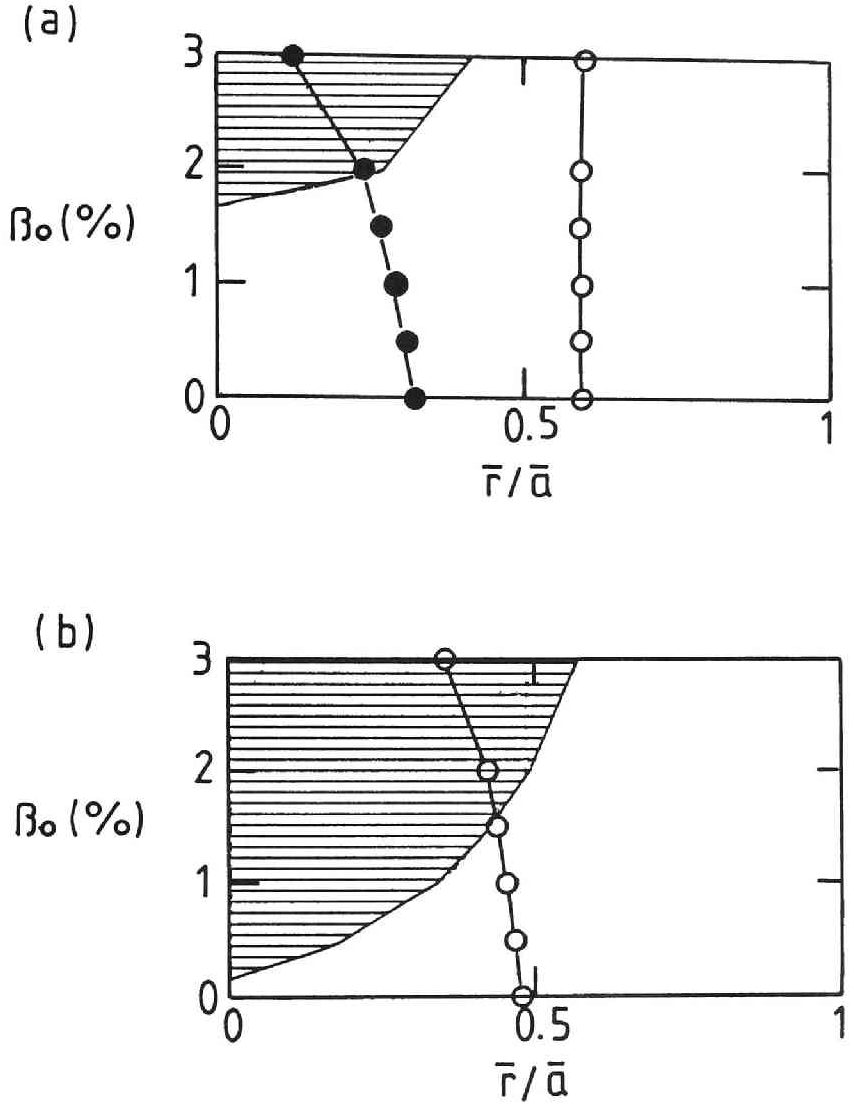

Fig.6.14 Magnetic well region in the $(\beta_0, \bar{r}/\bar{a})$ plane for (a) inward shift case of $\Delta_v = -0.79$cm and (b) outward shift case of $\Delta_v = +0.73$ cm. Shaded region belongs to the magnetic well. White circles denote the position of the $\iota = 1$ surface and black circles denote the position of the $\iota = 4/5$ surface.

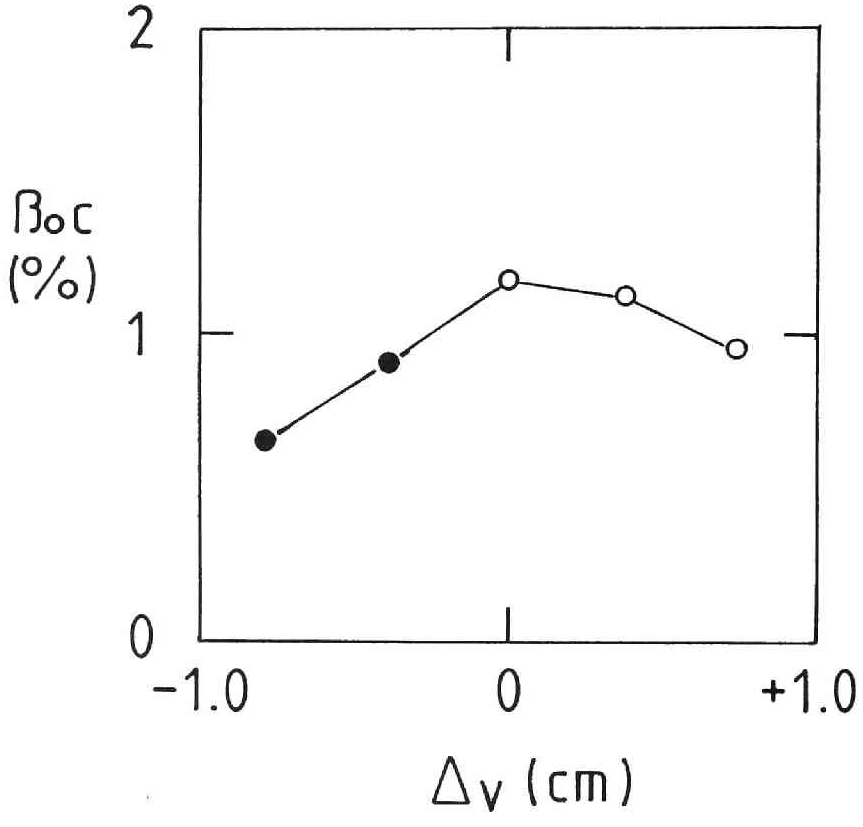

Fig.6.15 Beta limit of the most unstable mode when the magnetic axis is shifted inward or outward. White circles show $m = 1$ and $n = 1$ mode and the black circles show $m = 5$ and $n = 4$ mode.

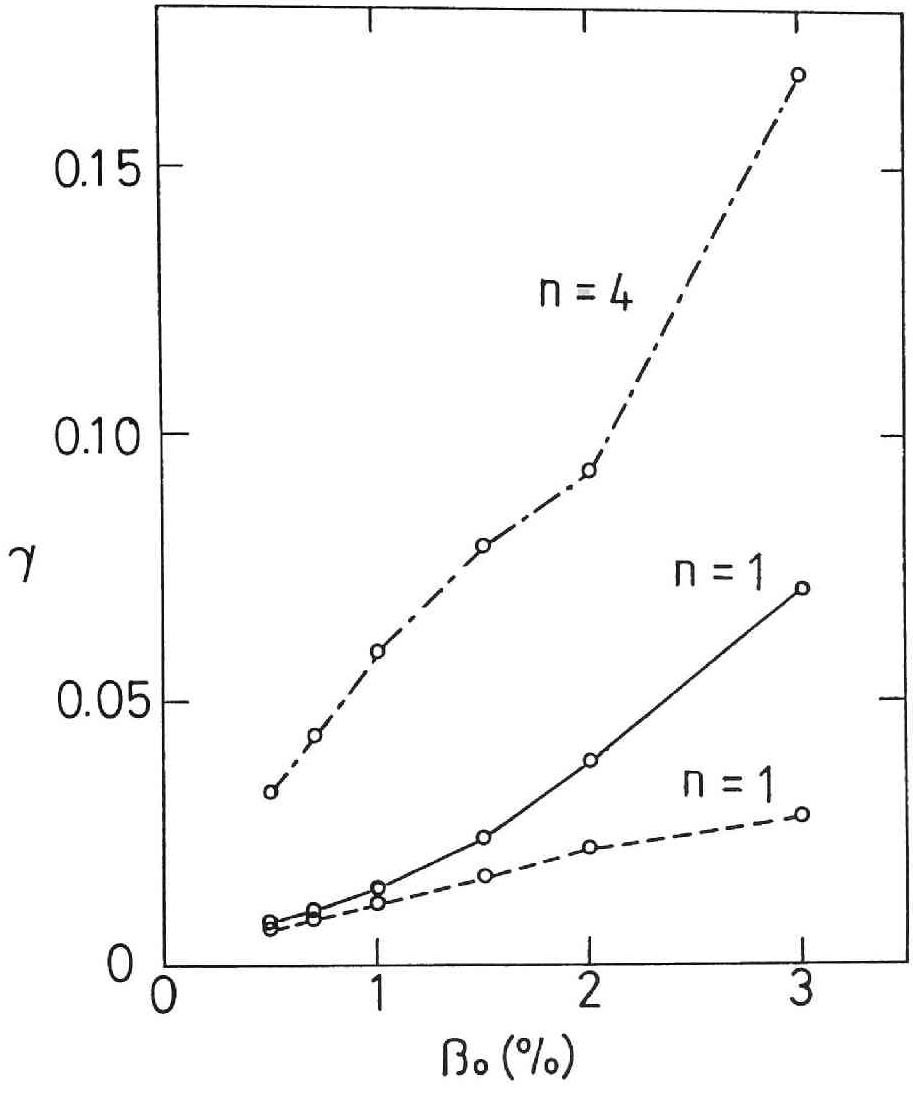

Fig.6.16 Growth rate of the unstable resistive modes corresponding to Fig.6.15 versus β_0 for $\Delta_v = -0.79cm$(dot and dashed line), $\Delta_v = 0$(solid line) and $\Delta_v = +0.73$ cm(dotted line). For β_0 =2% and 3%, the most unstable mode is $m = 4$ and $n = 4$ when $\Delta_v = -0.79cm$, while for $\beta_0 < 2\%$, it is $m = 5$ and $n = 4$. Here $S = 10^5$ and $P = P_0(1 - \Psi_{eq})^2$.

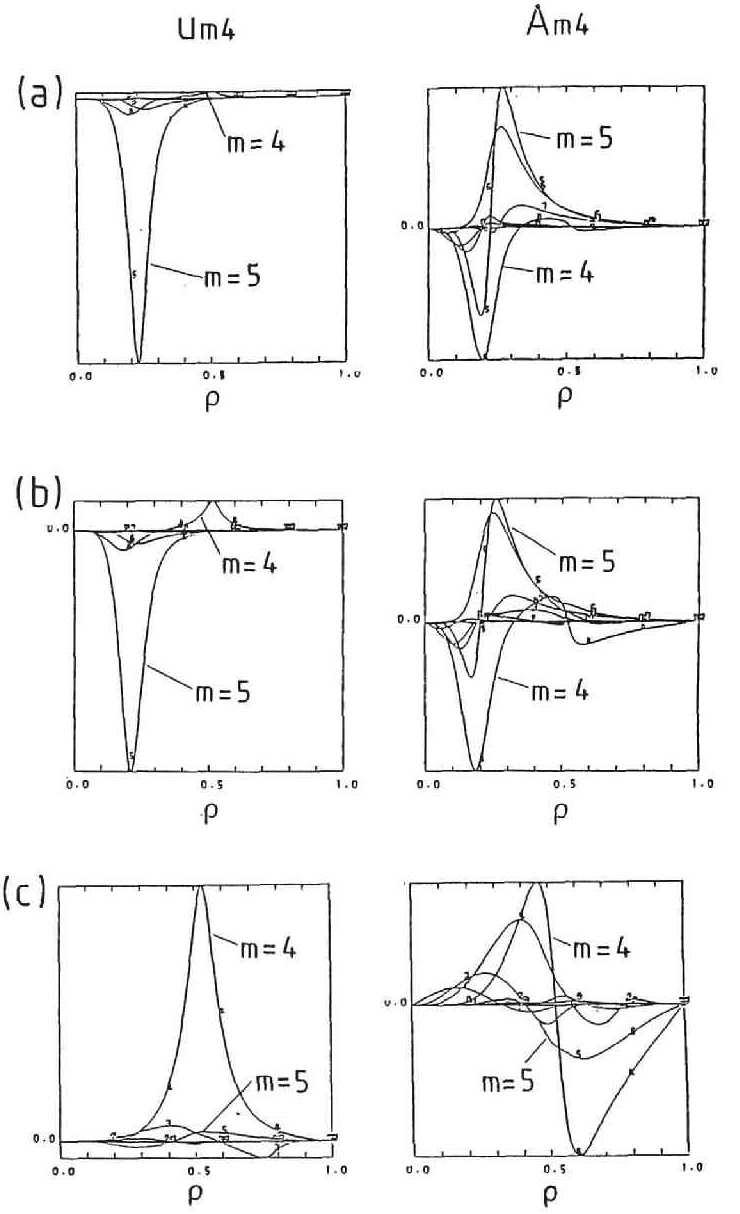

Fig.6.17 Eigenfunctions $u_{m4}(\rho)$ and $A_{m4}(\rho)$ of the resistive mode with $n = 4$ for several beta values corresponding to Fig.6.16 in the case of $\Delta_v = -0.79$cm; (a) $\beta_0 = 1.5\%$, (b) $\beta_0 = 2\%$ (c) $\beta_0 = 3\%$.

Chapter 7

Comparison between Equilibrium and Stability Theory and High Beta Experiments in Heliotron Devices

7.1 Introduction

Recently, experiments in both Heliotron E and Heliotron DR devices have been progressed and reliable data of MHD activities particularly for sawtooth type oscillations and internal disruptions have been accumulated. Here we

use 'internal disruption' for the large collapse in the soft X ray and density measurements without recovery of the electron temperature and the density. In this chapter, therefore, we compare the theoretical results in Chapters 3 and 6 with these experimental results and study how the theoretical models for the equilibrium and stability work.

In Heliotron E, the high-beta experiment was started in 1983 and the MHD activities were investigated for the two types of pressure profiles [2]. One was a fairly peaked profile where sawtooth oscillations and internal disruptions were observed. This type of experiment was called S mode. The other was a flat profile where soft X ray fluctuations were very weak and the highest beta value of $\bar{\beta} \sim 2\%$ was obtained. We called this experiment Q mode. During 1985 and 1986 we tried the high beta experiment again in Heliotron E with increase of NBI heating power from 2MW to 4MW [62]. We could reproduce the previous results and confirm that for a peaked or a highly peaked pressure profile the internal disruption is inevitable for $\beta_0 \gtrsim 2.0\%$, while for flat pressure profile the highest average beta value was realized. However, $\bar{\beta} \sim 2\%$ was not improved clearly. In recent two years, the effects of the axis shift by the additional vertical field on the MHD activities have been studied, and variations of soft X ray and density fluctuations with the axis shifts have been measured [63]. In Sec.7.2, we compare these experimental data of the Heliotron E with the numerical results obtained by using the BETA code in Chapter 3.

In the Heliotron DR experiment, finite beta plasma with $\bar{\beta} \lesssim 0.5\%$ were produced by ECRH with the 28GHz and 200kW gyrotron. The MHD instabilities limit the maximum beta value at $\bar{\beta} \sim 0.5\%$ for various magnetic

field intensities by using the second harmonic and the third harmonic ECRH [57,59,64]. The effects of the additional vertical field on the beta limit have been intensively studied [65]. We also try to explore a theoretical model to explain these MHD activities observed in Heliotron DR from the point of view of the ideal and resistive modes in Sec.7.3.

Conclusion is given in Sec.7.4.

7.2 Comparison of theoretical results with experiments in Heliotron E

The high beta experiments were carried out in Heliotron E device at the central magnetic field, $B_0 = 0.94$T [2]. By controlling gas puffing, two types of currentless finite beta plasma were generated. One was the type which had a broad pressure profile by the strong gas puffing. In this case, a maximum value of $\bar{\beta} \simeq 2\%$ was achieved associated with low level MHD fluctuations. This operation was called Q mode. One example with a fairly broad pressure profile is shown in Fig.7.1. When the gas puffing was stopped during the high power NBI heating phase, the other type of the plasma was realized. In this operation, the plasma had a fairly peaked pressure profile and sawtooth oscillations which were terminated by the internal disruption were observed as shown in Fig.7.2, which enhanced the energy loss significantly and degrade the critical beta value. Although the central beta value β_0 before the internal disruption in this case was comparable or higher than that of Q mode, the average beta value was always smaller than the maximum average beta value in the Q mode. From the soft X ray measurement, it was found that the mode structure triggering the internal disruption was estimated as the $m = 1$ mode (see Fig.7.3). This discharge was called S mode. By plotting the beta value versus the amplitude of the internal disruption, we may estimate the beta limit as shown in Fig.7.4.

We have examined the ideal stability of Heliotron E currentless equilib-

rium with the pressure profile of $P = P_0(1-0.6\bar{r}^2)^2$ for the inner tube model and obtained the critical beta value of $\bar{\beta} = 2\%$ for the $m = 1$ and $n = 1$ mode in Chapter 3. This pressure profile may correspond to the S mode rather than Q mode. Therefore, this result seems to be optimistic compared to the experimental data. Other calculations based on the STEP code by Rewoldt et al. [60], also showed that the beta limit of the $n = 1$ mode in Heliotron E is around $\beta_0 \lesssim 4\%$ or $\bar{\beta} \sim 2\%$ for the similar pressure profile, which is also higher than the experimental values. Hence the origin of the MHD activity producing the internal disruption is expected to be resistive modes. In the analysis for the Heliotron DR plasma in Chapter 6, we showed that the resistive modes have significant growth rates in the stable region to the ideal modes when $S \simeq 10^5 \sim 10^6$. Recently, we also studied the resistive instability with $n = 1$ in the Heliotron E plasma by using the RESORM code for the pressure profile of $P = P_0(1-\Psi_{eq})^2$. The growth rates are shown in Fig.7.5 where the effects of the vertical magnetic field are also included [66]. Here $S = 10^6$ is used, which is estimated from $B_0 = 0.94$T, $T_e \simeq 400$eV and $n_e \simeq 5 \times 10^{19}\mathrm{m}^{-3}$ obtained in the experiments. As shown in this figure, the resistive instability with the substantial growth rate exists for $\beta_0 \lesssim 4\%$ where the $n = 1$ ideal mode is stable. This supports that the low n resistive instability is a candidate to explain the MHD activities in the standard Heliotron E currentless plasmas. Nonlinear calculation of the $m = 1$ and $n = 1$ resistive interchange mode by Wakatani et al., [52] demonstrated behaviors similar to the internal disruption driven by this mode. When the pressure profile becomes broad, which corresponds to the Q mode, growth rate of the resistive instability is decreased for $\bar{\beta} \lesssim 2\%$ by the decrease of the pressure

gradient at $\iota = 1$ surface.

We have shown in Chapter 3 that the outward shift of the magnetic axis can suppress the ideal MHD instability with the $m = 1$ and $n = 1$ mode and produce the second stability region. According to this result, the effects of the additional vertical field on MHD stability have been investigated in Heliotron E [63] and Heliotron DR[65] experiments. In the inward shift case of Heliotron E, the sawtooth oscillations and the internal disruption were observed at lower beta value than the standard case as shown in Fig.7.6. This tendency is explained by the theoretical result. However, the critical beta value obtained by the BETA code is still larger than the experimental data. This difference also may be attributed to the resistive effect on the instability. In Fig.7.5, growth rates of the $n = 1$ mode are shown for both outward and inward axis shift case, which correspond to the cases of $\Delta_v = 2cm$ and $\Delta_v = -2cm$, respectively, in Fig.7.6. In the inward axis shift case, the significant growth rate is obtained at $\beta_0 \simeq 1\%$ in the inward shift case. This agrees with that MHD activities are observed experimentally for $\beta_0 \gtrsim 1\%$. Figure 7.5 also shows that the $m = 2$ and $n = 1$ mode resonant at $\iota = 0.5$ is dominant for $\beta_0 \lesssim 2\%$ (see black squares); however, we did not pay attention to this mode in the stability analysis using the BETA code as explained in Chapter 3. This $m = 2$ and $n = 1$ mode is already observed experimentally, which shows the inversion radius of the sawtooth oscillation in the neighborhood of $\iota = 0.5$ surface.

In the outward axis shift case of Heliotron E, the growth rate of the $n = 1$ resistive mode decreases and an improved plasma behaviors are expected. However, because of the unexpected degradation of the transport or the

increase of the direct loss of high energy particles, the beta value did not increase according to the theoretical prediction. Thus, in order to increase the beta stability limit in the outward shift case, we must invent to keep the good confinement during the high power NBI heating, which is a future experimental subject beyond the MHD equilibrium and stability.

7.3 Comparison of the ideal and resistive stability results with experiments in Heliotron DR

First we discuss the beta limit for the standard configuration. Heliotron DR results give $\bar{\beta} \simeq 0.5\%$ as the maximum average beta value when the magnitude of magnetic field is varied from 0.2T to 0.55T as shown in Fig.7.7 [57]. Magnetic fluctuations are always observed when the beta value becomes close to $\bar{\beta} \simeq 0.5\%$. Many cases show that the sawtooth oscillations and the internal disruption occur at this average beta value, whose characteristics are very similar to those observed in Heliotron E. They are triggered by the $m = 1$ and $n = 1$ mode resonant at the $\iota = 1$ surface by considering the time evolution of radial profiles of the soft X ray, which is obtained during the sawtooth oscillations in Heliotron DR as shown in Fig.7.8 [64]. The peak of the soft X ray fluctuation amplitude exists around the $\iota = 1$ surface and displacement of the region within the $\iota = 1$ surface estimated from the soft X ray profile is consistent with the $m = 1$ mode. These results of the mode structure are also supported by the eigenmode shown in Fig.6.11.

Ideal MHD stability calculations of low n pressure-driven modes by the STEP code give the results that the maximum central beta value is $\beta_0 \simeq 1.2\%$ and the corresponding average beta value is $\bar{\beta} \simeq 0.5\%$ as shown in Fig.6.5. Resistive MHD calculations by the RESORM code show that the resistive pressure-driven modes or resistive interchange modes are unstable even for

$\beta_0 < 1.2\%$ with substantial growth rates as shown in Fig.6.8. Experimentally it is not clear at what beta value the magnetic fluctuations appear. However, it is not unreasonable that they appear at the lower beta value than the ideal MHD beta limit by the STEP code and the beta value saturates at $\bar{\beta} \simeq 0.5\%$ by the degradation of the confinement with the increase of the magnetic fluctuation amplitude or by the sawtooth oscillations and the internal disruption. This scenario for the saturation of the beta limit seems consistent with the Heliotron DR results. If it is true, the dominant instability may be the resistive one. However, since the ideal MHD beta limit is very low, it is not clear which type of mode is important, the resistive one or the ideal one, in the Heliotron DR experiment. It should be noted that, in Heliotron E, the MHD activities appear at $\beta_0 \gtrsim 2\%$ for peaked pressure profiles, which is clearly lower than that corresponding to the ideal MHD stability limit.

When the vertical magnetic field was changed to shift the magnetic axis inward or outward in the vacuum configuration, Heliotron DR results showed that the beta limit decreased in both cases as shown in Fig.7.9 [65]. This could be explained from the STEP code and the RESORM code results. In the inward shift case, the new resonant surface at $\iota = 4/5$ appears in the region of significant pressure gradients and weak shear. Then the pressure-driven mode with $n = 4$ gives the lower beta limit than that by the $n = 1$ mode in the standard configuration. On the other hand, in the outward shift case, the $\iota = 1$ surface moves to the region with the larger pressure gradient than that of the standard configuration at the fixed beta value under the same pressure profile. Then the beta limit determined by the $m = 1$ and $n = 1$ ideal mode decreases to $\beta_0 \simeq 0.9\%$. Although the magnetic well region

expands in the central region by the outward shift of the magnetic axis, the $\iota = 1$ surface still belongs to the magnetic hill region and the growth rates of the $n = 1$ resistive mode in the outward case are almost the same as those in the standard case for $\beta_0 \lesssim 1\%$ (see Fig.6.16). Hence, the resistive modes may be dominant in the outward shift case. These results are not general in the heliotron configurations including Heliotron E and Heliotron H. Usually the magnetic well produced by the outward magnetic shift gives favorable effects on the MHD stability theoretically.

7.4 Conclusion

We have compared the theoretical results in Chapters 3 and 6 with the experimental data in Heliotron E and DR to study validity of the ideal and the resistive models in heliotron/torsatron configurations.

In the Heliotron E high beta experiments, the sawtooth oscillations with $(m, n) = (1, 1)$ dominantly and the internal disruption were observed in the S mode regime with the peaked pressure profiles. The numerical calculation of the ideal stability for the currentless equilibrium with such a peaked pressure profile by the BETA code gave the higher beta limit for the $m = 1$ and $n = 1$ mode than the experimental data. According to the resistive stability calculation with the RESORM code, the resistive modes become unstable with substantial growth rates in the stable region against the ideal modes. Therefore, we conclude that the resistive mode is crucial in explaining the Heliotron E experimental data.

In the inward axis shift case by the additional vertical field, the beta limit degrades experimentally both in Heliotron E and Heliotron DR. This tendency coincides with the theoretical result in Chapter 3, however, the critical beta value, $\bar{\beta}_c$, by the BETA code is still higher than the experimental data. The resistive stability calculation with the RESORM code shows that the $m = 1$ and $n = 1$ mode becomes strongly unstable for $\bar{\beta} < \bar{\beta}_c \simeq 1.3\%$, however, the $m = 2$ and $n = 1$ mode becomes dominant for $\bar{\beta} \sim \beta_0/3 \lesssim 0.6\%$. It coincides with the fact that the $m = 2$ and $n = 1$ mode was observed in the Heliotron E experiments.

In the outward shift case, the improvement of the experimental beta value is not significant in contrast to the theoretical expectation. This is related to the unexpected degradation of the transport or increase of the direct loss.

In the standard configuration of Heliotron DR, the maximum beta value obtained experimentally, $\bar{\beta} \simeq 0.5\%$, is almost the same as the theoretical critical value by the ideal low n stability analysis for the pressure profile close to the experimental one (see Chapter 6). However, the MHD fluctuations seems to be seen at lower beta values than the ideal stability limit. The resistive stability calculation in Chapter 6 shows that there exist the $n = 1$ resistive modes with substantial growth rates in the stable region against the ideal modes. Therefore, the resistive modes seem to be more important than the ideal ones; however, the experimental beta values saturate at around the ideal beta limit.

For both the outward and inward axis shifts the beta limit decreases experimentally, which is somewhat different from the Heliotron E case. The theoretical results in Chapter 6 may explain these results. In the inward shift case, the $\iota = 4/5$ resonant surface appears in the weak shear region with significant pressure gradient, and the $m = 5$ and $n = 4$ mode resonant at this surface becomes more unstable than the $m = 1$ and $n = 1$ mode. In the outward shift case, the $\iota = 1$ surface moves to the larger pressure gradient region than that in the standard case under the same pressure profile. Hence the $m = 1$ and $n = 1$ mode becomes more unstable and the beta limit decreases.

In summary, the ideal MHD model is useful to give a crude estimation at which beta value global MHD instabilities appear. The resistive MHD

model is crucial to investigate the physics of the observed macroscopic MHD phenomena such as sawtooth like oscillation and internal disruption.

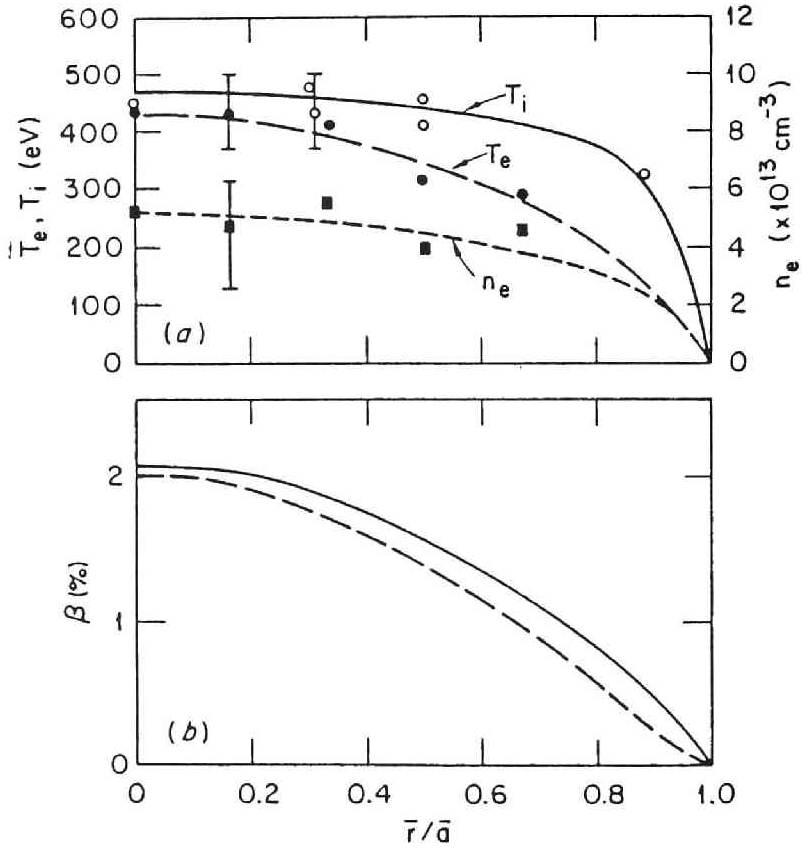

Fig.7.1 Profiles for a discharge at the threshold for the onset of MHD activity ($\beta_0 \simeq 2.1\%$, $\bar{\beta} \simeq 1\%$) in Heliotron E; (a) temperature and density profiles (charge-exchange and single-shot Thomson scattering measurement) (b) $\beta(\bar{r})$ profiles derived from fits to experimental data. In (b) the T_i profile was used for the solid curve, while the assumption $T_i(\bar{r}) = T_e(\bar{r})$ was used for the dotted curve [2].

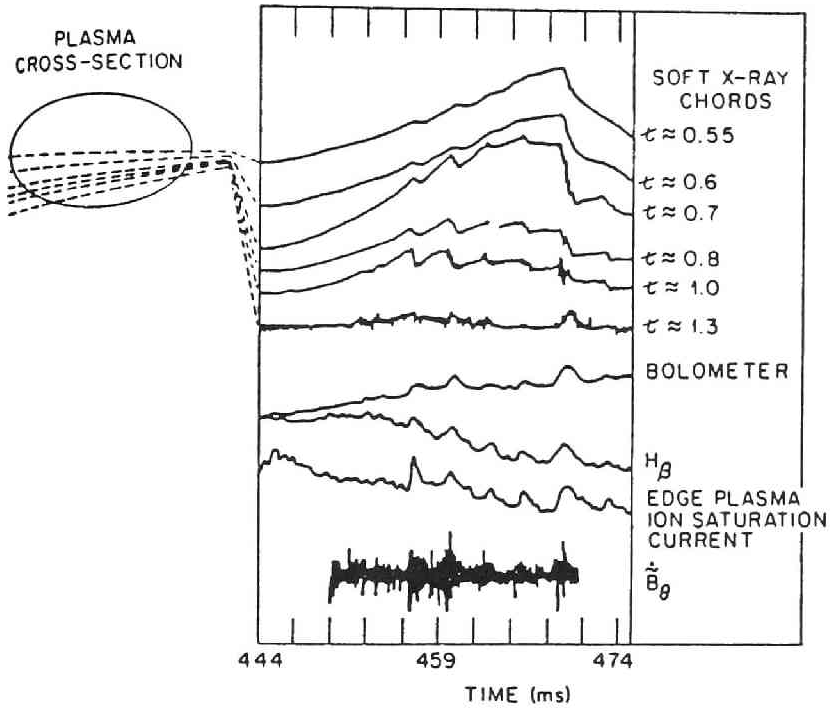

Fig.7.2 Diagnostic signals for a high beta Heliotron E discharge with sawteeth. The chordal soft X ray signals are labeled with ι values of their tangent flux surfaces. The last sawtooth (at $t \simeq 469$ ms) is an internal disruption [2].

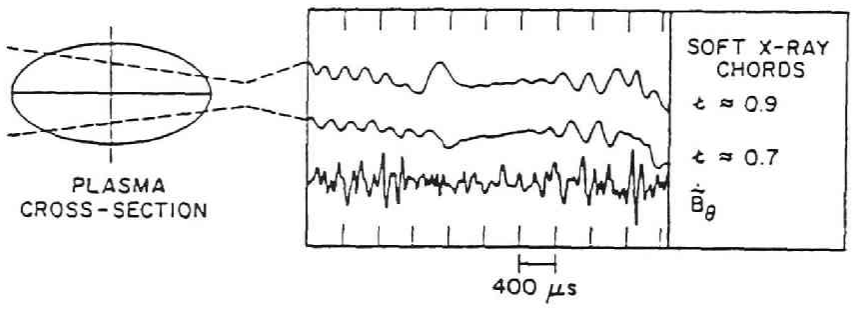

Fig.7.3 Time expansion of soft X ray and Mirnov-loop ($\tilde{B}_\theta$) signals during successive $m = 1$ instability cycles in Heliotron E [2].

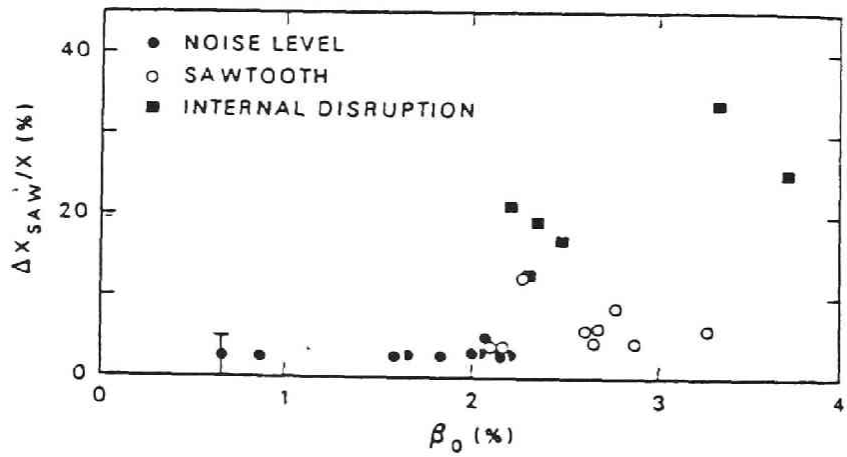

Fig.7.4 Central-chord X ray sawtooth amplitude of Heliotron E plasma ($\Delta X_{SAW}/X$) as a function of β_0 for discharges with moderately peaked profiles. For $\beta_0 < 2\%$, only weak fluctuations are observed [2].

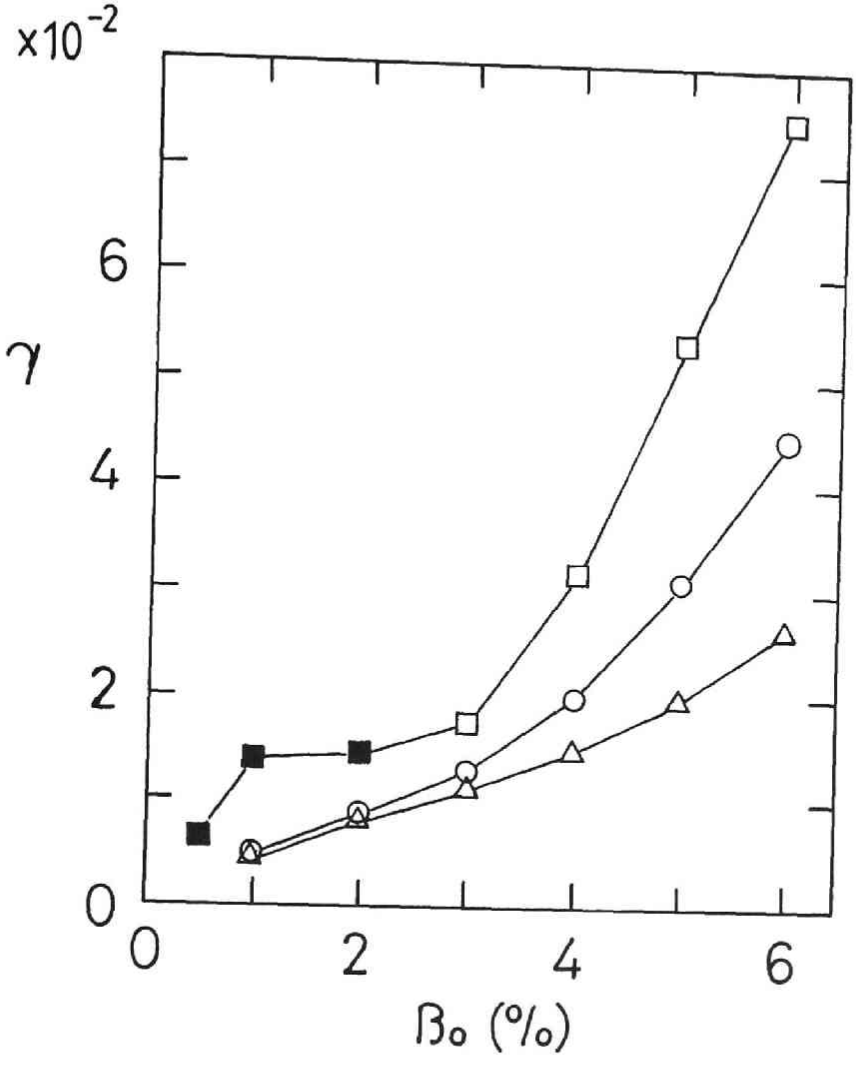

Fig.7.5 Growth rates of $n = 1$ resistive mode in Heliotron E obtained by RESORM code. Circles show the growth rates for the standard case, squares for the inward axis shift case of 2cm and triangles for the outward axis shift case of 2cm. Except black squares denoting that $m = 2$ and $n = 1$ mode is dominant, $m = 1$ and $n = 1$ is a dominant mode.

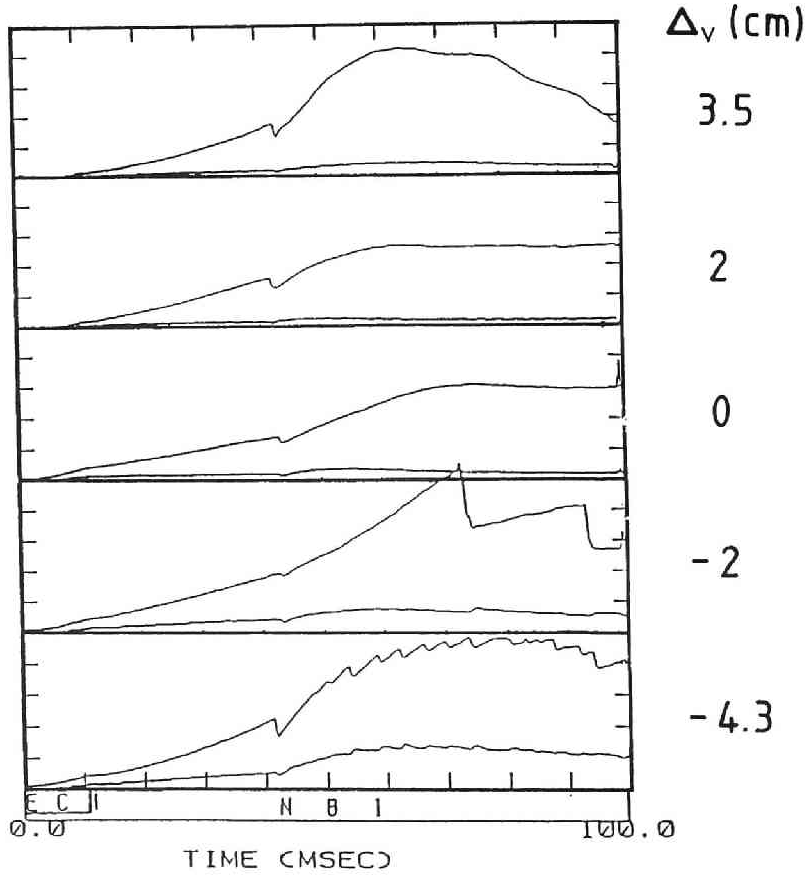

Fig.7.6 Soft X ray measurements at different magnetic axis positions controlled by the additional vertical field in Heliotron E plasma with $\beta_0 \lesssim 1.5\%$. Δ_v denotes magnetic axis shift measured from the standard position in vacuum configuration . Upper and lower lines of each figure correspond to the central and peripheral chords, respectively [63].

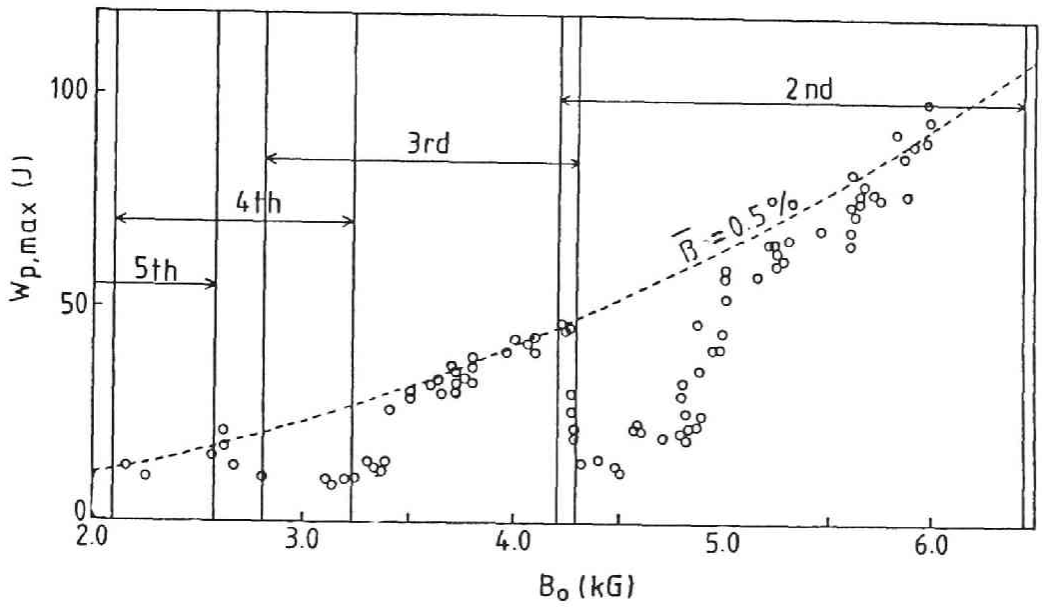

Fig.7.7 The maximum stored plasma energy W_p versus magnetic field intensity B_0 in Heliotron DR. Harmonic numbers of the ECRH used in the plasma heating are also shown [57].

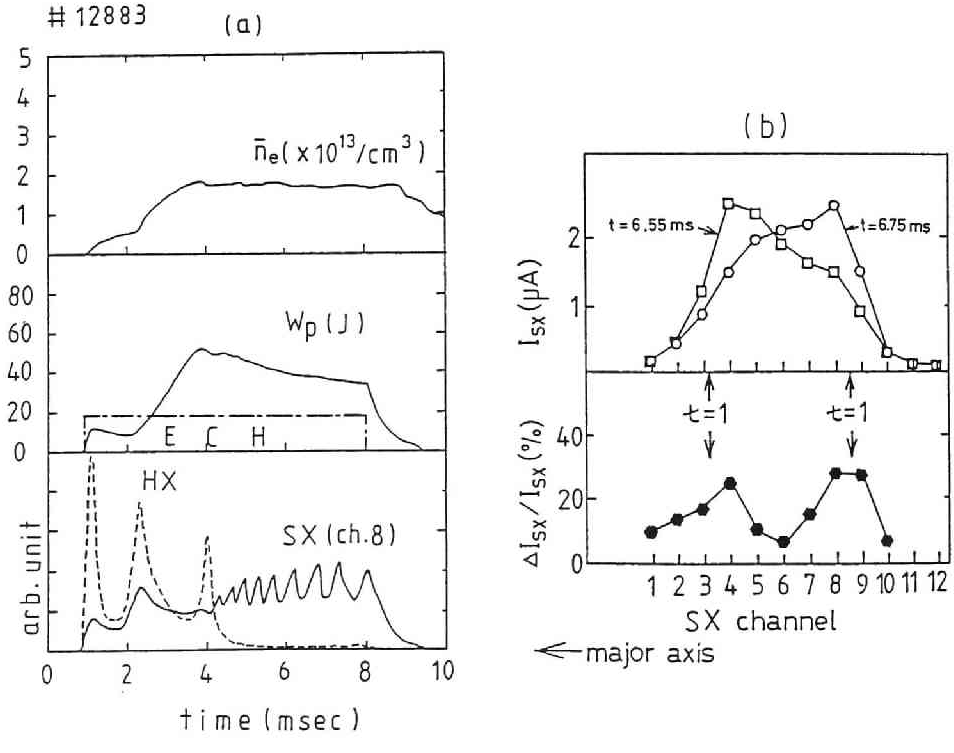

Fig.7.8 Discharge with sawtooth oscillations in Heliotron DR; (a)time evolution of density (n_e), stored energy (W_p) and X ray signals (SX denotes soft X ray and HX denotes hard X ray), (b) radial profiles of total and fluctuations of soft X ray during sawtooth oscillation [64].

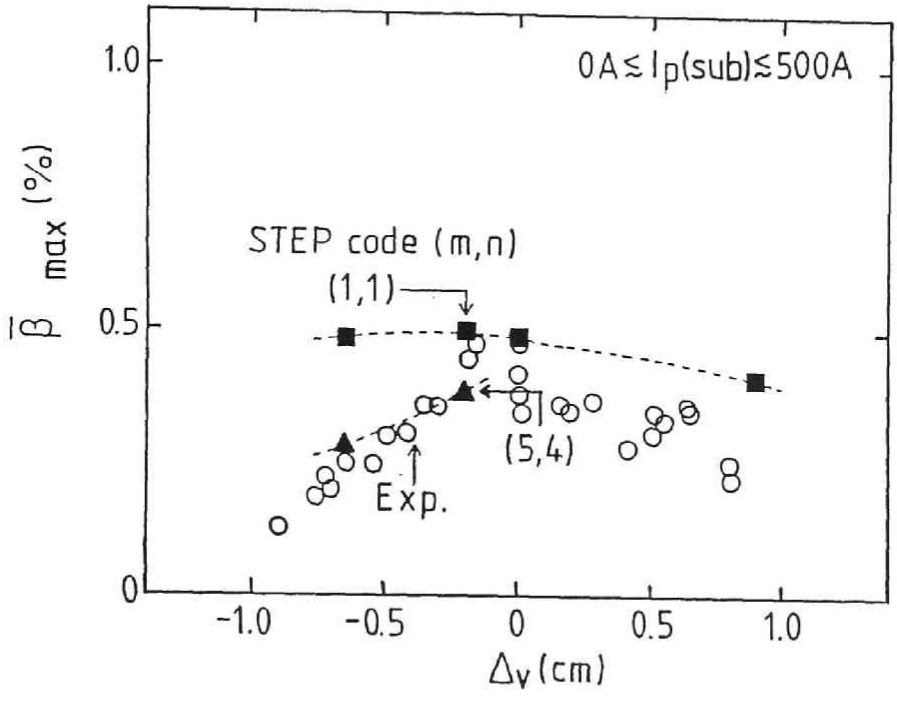

Fig.7.9 Maximum beta values versus shift of magnetic axis in vacuum. Black squares and triangles show results by STEP code. White circles show experimental data [65].

Chapter 8

Concluding Remarks

We have studied three-dimensional MHD equilibrium and stability for stellarator/heliotron configurations intensively. We have used the two different theoretical approaches; one is the pure three-dimensional numerical calculations and the other is based on the reduced MHD equations for stellarators. The main results are summarized here.

First, we have investigated both Heliotron E and Heliotron H plasmas by using the three-dimensional MHD code, BETA code.

(1) In the currentless equilibrium of Heliotron E, the average stability beta limit by the resonant $m = 1$ and $n = 1$ ideal pressure-driven mode under the fixed boundary condition is $\bar{\beta} = 2\%$ which was given by the BETA code. Until now there is no other theoretical result using the three-dimensional MHD code; however, this value is close to the highest beta value obtained in Heliotron E high beta experiments. The FCT

equilibria of Heliotron E is more unstable; however, the decrease of the beta limit is not large. By studying the equilibrium properties for these equilibria according to the increase of the beta value, it is found that the main stabilizing effect to enter the second stability region is the magnetic well.

(2) With the BETA code the critical beta value of the currentless equilibrium of Heliotron H for the non-resonant $m = 1$ and $n = 1$ ideal mode is $\bar{\beta} = 3.2\%$, which is obtained under the fixed boundary condition. It seems more stable than that of the Heliotron E currentless plasma. Under the free boundary condition, the stability of the Heliotron H degrades, since the non-resonant mode becomes more dangerous.

(3) When the magnetic axis is shifted outward significantly in the vacuum configuration, the ideal $m = 1$ and $n = 1$ mode is stabilized completely in both the Heliotron E and Heliotron H configurations. On the other hand the inward shift destabilizes the mode significantly by losing the magnetic well or enhancing the magnetic hill.

We have investigated the equilibrium properties of the spatial axis stellarator, Asperator NP-4, by using the BETA code and compared the results to the same quantities evaluated by the Solov'ev-Shafranov theory.

(4) It is found that the variation of the rotational transform due to the plasma pressure effect is small. The rotational transform is estimated by the value in the straight helical axis configuration at $\beta = 0$ with sufficient accuracy. This point is significantly different from the Heliotron

E case. By estimating the toroidal correction in the curvature and the torsion of the magnetic axis accurately, the analytic relations to obtain the helical and the toroidal shifts of the magnetic axis in the Asperator NP-4 configuration are given. These quantities agree reasonably with the values by the BETA code.

(5) The magnetic well due to the Shafranov shift is estimated analytically and it is found that the magnetic hill changes to the well at $\bar{\beta} \simeq 1\%$ which agrees with the results by the BETA code in the neighborhood of the magnetic axis. By introducing the triangularity in the shape of the plasma boundary, the magnetic well expands and becomes deep even in the vacuum configuration of Asperator NP-4 type.

(6) From the point of the Mercier criterion for the local stability, which is estimated by the BETA code numerically, the Asperator NP-4 configuration without the triangular deformation is more unstable than heliotron configurations. Therefore, stability improvement may be required to confine high beta plasmas in this device, although there is no theoretical result for the global mode stability.

In order to study the resistive instability we have developed the RESORM code which is the initial value code based on the reduced MHD equations for stellarator/heliotron configurations.

(7) The reduced equations including the higher order toroidal corrections are derived without the expansion for R/R_0, which is called the improved stellarator expansion. The stellarator equilibrium equation ob-

tained from the reduced MHD equations by assuming $\partial/\partial t = \mathrm{v}_\perp = 0$ is the same as that given by Nakamura et al.[15]

The currentless equilibrium and the linear stability for both the ideal and resistive modes are studied in the Heliotron DR configuration.

(8) It is shown that the Shafranov shift is small in Heliotron DR which prevents the formation of the magnetic well. In consequence of this property, the stability beta limit is $\beta_0 \simeq 1.2\%$, which is determined by the $m = 1$ and $n = 1$ ideal pressure-driven mode resonant at the $\iota = 1$ surface in the plasma column. The beta limits obtained by the both RESORM and STEP codes agree with each other.

(9) The Mercier criterion derived by using the improved stellarator expansion gives the lower limit of $\beta_0 \simeq 0.7\%$. In the region of $0.7\% \lesssim \beta_0 \lesssim 1.2\%$, growth rate of the ideal mode becomes very small and the mode structure becomes localized sharply at the resonant surface. Therefore, the numerical code using a finite difference method with a finite mesh size can not treat such a strongly localized mode. Practically, this region is marginally stable to the low n modes.

(10) The resistive pressure gradient driven mode resonant at the $\iota = 1$ surface has substantial growth rates even for $\beta_0 < 1.2\%$. The $S^{-1/3}$ dependence of the growth rate is clearly seen in the Mercier stable region, however, the resistive modes are affected by the ideal instabilities in the Mercier unstable region.

(11) It is found that both the inward and outward shifts of the magnetic axis in the vacuum configuration caused by the additional vertical field have the tendency destabilizing the ideal modes. This is a unique property of Heliotron DR. Usually the outward shift has the stabilizing effects on the pressure-driven modes as discussed for the Heliotron E case. In the inward shift case, the ideal and resistive modes resonant at the $\iota = 4/5$ surface are destabilized. On the contrary, in the outward shift case, the ideal mode of $(m, n) = (1, 1)$ is destabilized by the effect of the inward movement of the $\iota = 1$ surface to the larger pressure gradient region; however, the growth rates of the unstable resistive mode are decreased a little by the magnetic well formation.

We have compared above theoretical results with the experimental data in Heliotron E and Heliotron DR.

(12) The MHD activity with $(m, n) = (1, 1)$ was observed in many cases of Heliotron E experiments, and they usually appeared for $\beta_0 \gtrsim 2.0\%$ and this beta value depends on the pressure profiles. The ideal beta limit given by the BETA code is higher than the critical beta value at which the fluctuation appears, and the $m = 1$ and $n = 1$ resistive mode with substantial growth rate exists at $\beta_0 \simeq 2\%$. Therefore, the resistive mode with $(m, n) = (1, 1)$ seems to be a candidate to explain the MHD activity observed experimentally. Based on the nonlinear calculations of the resistive interchange modes, this point is confirmed definitely [52].

(13) In the case of the inward shift of the magnetic axis by the additional

vertical field, the destabilizing tendency obtained theoretically is consistent with the Heliotron E experiment. However, in the outward shift case, the experimental beta limit of Heliotron E did not improved. This point seems contradictory with the theoretical results within the MHD model. Tentative explanation to resolve the discrepancy is that a degradation of the particle and energy transports or an increase of the direct loss of the high energy particles occurs induced by the outward magnetic axis shift and it becomes difficult to increase the beta value with the same heating power.

(14) In Heliotron DR plasma, the $m = 1$ and $n = 1$ fluctuation was also observed when the beta value becomes close to $\bar{\beta} \simeq 0.5\%$ which seems consistent with the ideal MHD beta limit of $\beta_0 \simeq 1.2\%$ or $\bar{\beta} \simeq 0.5\%$ obtained by the STEP and RESORM codes. Therefore, it is not clear that which determines the beta limit of Heliotron DR, resistive one or ideal one, although the resistive instabilities are more dangerous.

(15) By the theoretical studies, the beta limit is decreased with the magnetic axis shift for both inward and outward directions. These results are also consistent with Heliotron DR experiments.

Finally we will discuss future problems of three-dimensional MHD studies for stellarator/heliotron configurations. As discussed in this thesis extensively there are two approaches. One is to calculate the three-dimensional equilibrium without any averaging procedure which is firstly established by the BETA code. The other one is to use the averaging method over the helical field period with or without the stellarator ordering. In order to calculate

both the ideal and resistive linear stabilities for the low n global modes with sufficient accuracy, the best way is to developed the initial value code such as the RESORM code or the FAR code, where the averaging process is essential to reduce computation time and to keep numerical accuracy. Another advantage of this approach is that this type of numerical codes can be easily extended to study nonlinear evolution of the unstable modes. Thus we propose a new approach that MHD equilibrium is calculated by the three-dimensional code, and then, the global MHD stability is examined by the initial value code after averaging the three-dimensional equilibrium by appropriate procedures. We believe that a code development based on this idea will work efficiently for studying the global modes in the three-dimensional configurations.

References

[1] K.Uo, A.Iiyoshi, T.Obiki, O.Motojima, S.Morimoto, M.Wakatani, A.Sasaki, K.Kondo, M.Sato, K.Hanatani, T.Mutoh, H.Zushi, H.Kaneko, S.Besshou, M.Nakasuga, F.Sano, T.Mizuuchi, S.Sudo, J.H.Harris, J.E.Rice, J.L.Terry, I.Ohtake, M.Iima, H.Okada, K.Magome, Nucl. Fusion **24** (1984) 1551.

[2] J.H.Harris, O.Motojima, H.Kaneko, S.Besshou, H.Zushi, M.Wakatani, F.Sano, S.Sudo, A.Sasaki, K.Kondo, M.Sato, T.Mutoh, T.Mizuuchi, M.Iima, T.Obiki, A.Iiyoshi, K.Uo, Phys. Rev. letter **53** (1984) 2242.

[3] J.P.Freidberg, *'Ideal Magnetohydrodynamics'* (Plenum Press, New York, 1987).

[4] J.D.Lawson, Proc. Roy. Soc. (London) **B70** (1957) 6.

[5] H.P.Furth, J.Killeen, M.N.Rosenbluth, Phys. Fluids **6** (1963) 459.

[6] J.M.Greene, J.L.Johnson, Phys. Fluids **4** (1961) 875.

[7] J.M.Greene, J.L.Johnson, Phys. Fluids 4 (1961) 1417.

[8] F.Bauer, O.Betancourt, P.Garabedian, *'A Computational Method in Plasma Physics'* (Springer-Verlag, New York, 1978).

[9] F.Bauer, O.Betancourt, P.Garabedian, *'Magnetohydrodynamic Equilibrium and Stability of Stellarators'* (Springer-Verlag, New York, 1984).

[10] G.Anania, J.L.Johnson, K.E.Weimer, Phys. Fluids **26** (1983) 2210.

[11] G.Anania, J.L.Johnson, Phys. Fluids **26** (1983) 3070.

[12] I.B.Bernstein, E.A.Frieman, M.D.Kruskal, R.M.Kulsrud, Proc. Roy. Soc. (London) **A244** (1958) 17.

[13] J.L.Johnson, H.E.Dalhed, J.M.Greene, R.C.Grimm, Y.Y.Hsieh, S.C.Jardin, J.Manickam, M.Okabayashi, R.G.Storer, A.M.M.Todd, D.E.Voss, K.E.Weimer, J. Comp. Phys. **32** (1979) 212.

[14] R.C.Grimm, R.L.Dewar, J.Manickam, J. Comp. Phys. **49** (1983) 94.

[15] Y.Nakamura, K.Ichiguchi, M.Wakatani, J.L.Johnson, J. Phys. Soc. Jpn. **58** (1989) 3157.

[16] L.M.Kovrizhnykh, S.V.Shchepetov, Sov. J. Plasma Phys. **6** (1980) 533.

[17] B.A.Carreras, H.R.Hicks, J.A.Holmes, V.E.Lynch, L.Garcia, J.H.Harris, T.C.Hender, B.F.Masden, Phys. Fluids **26** (1983) 3569.

[18] J.Todoroki, J. Phys. Soc. Jpn. **56** (1987) 128.

[19] R.Gruber, J.Rappaz, *'Finite Element Methods in Linear Ideal Magnetohydrodynamics'* (Springer-Verlag, New York, 1985).

[20] L.S.Solov'ev, V.D.Shafranov, *Revs.of Plasma Phys. (M.A.Leontovich Ed.)* vol.5 (Consultant Bureau, New York, 1970).

[21] T.C.Hender, B.A.Carreras, Phys. Fluids **27** (1984) 2101.

[22] A.E.Koniges, J.L.Johnson, Phys. Fluids **28** (1985) 3127.

[23] H.R.Strauss, Phys. Fluids **20** (1977) 1354.

[24] H.R.Strauss, Plasma Phys. **22** (1980) 733.

[25] M.Wakatani, IEEE Trans. Plasma Sci. **PS–9** (1981) 243.

[26] V.E.Lynch, B.A.Carreras, L.A.Charlton, T.C.Hender, L.Garcia, H.R.Hicks, T.A.Holmes, J. Comp. Phys. **66** (1986) 411.

[27] M.D.Kruskal, R.M.Kulsrud, Phys. Fluids **1** (1958) 265.

[28] R.Chodura, A.Schlüter, J. Comp. Phys. **41** (1981) 68.

[29] T.C.Hender, B.A.Carreras, L.Garcia, J.A.Rome, V.E.Lynch J. Comp. Phys. **60** (1985) 76.

[30] A.H.Boozer, Phys. Fluids **25** (1982) 520.

[31] K.Harafuji, T.Hayashi, T.Sato, J. Comp. Phys. **81** (1989) 169.

[32] F.Bauer, O.Betancourt, P.Garabedian, M.Wakatani, *'The BETA Equilibrium, Stability and Transport codes'* (Academic Press, New York, 1987).

[33] S.P.Hirshman, W.I.Van Rij, P.Merkel, Comput. Phys. Commun. **43** (1986) 143.

[34] O.Betancourt, Commun. on Pure and Applied Math. **XLI** (1988) 551.

[35] L.L.Lao, J.M.Greene, T.S.Wang, F.J.Helton, E.M.Zawadzki, Phys. Fluids **28** (1985) 869.

[36] U.Schwenn, Comput. Phys. Commun. **31** (1984) 167.

[37] L.M.Degtyarev, V.V.Drozdov, M.I.Mikhailov, V.D.Pustovitov, V.D.Shafranov, Sov. J. Plasma Phys. **11** (1985) 22.

[38] G.Bateman, *'MHD Instabilities'* (MIT Press, 1978).

[39] F.Bauer, O.Betancourt, P.Garabedian, Phys. Fluids **24** (1981) 48.

[40] M.Wakatani, K.Ichiguchi, F.Bauer, O.Betancourt, P.Garabedian, Nucl. Fusion **26** (1986) 1359.

[41] K.Uo, M.Nakasuga, K.Hanatani, *'Heliotron Magnetic Surfaces'* PPLK Rep. PPLK-3 (1982).

[42] M.Wakatani, K.Ichiguchi, H.Sugama, K.Itoh, A.Hasegawa, J.Todoroki, H.Naitou, Plasma Physics and Controlled Nuclear Fusion Research 1986 (Proc. 11th Int. Conf. Kyoto, 1986) CN-47/D-V-3.

[43] T.C.Hender, B.A.Carreras, V.E.Lynch, *'Heliac equilibria'* Rep. ORNL-TM-10171 Oak Ridge National Lab. TN(1986).

[44] Y.Funato, I.Sakamoto, H.Watanabe, Jpn. J. Appl. Phys. **22** (1983) 1188.

[45] K.Ichiguchi, M.Wakatani, Nucl. Fusion **28** (1988) 411.

[46] C.Mercier, H.Luc, *'Lectures in Plasma Physics'* CEC, Luxembourg (1974).

[47] J.L.Johnson, J.M.Greene, Plasma Phys. **9** (1967) 611.

[48] B.A.Carreras, N.Dominguez, *private communication.*

[49] A.H.Glasser, J.M.Greene, J.L.Johnson, Phys. Fluids **18** (1975) 875.

[50] K.Ichiguchi, Y.Nakamura, M.Wakatani, N.Yanagi, S.Morimoto, to be published in Nucl. Fusion.

[51] M.Wakatani , Nucl. Fusion **18** (1978) 1499.

[52] M.Wakatani, H.Shirai, M.Yamagiwa, Nucl. Fusion **24** (1984) 1407.

[53] H.R.Strauss, D.A.Monticello, Phys. Fluids **24** (1981) 1148.

[54] B.A.Carreras, N.Dominguez, L.Garcia, V.E.Lynch, J.F.Lyon, J.R.Cary, J.D.Hanson, A.P.Navarro, Nucl. Fusion **28** (1988) 1195.

[55] R.D.Hazeltine, J.D.Meiss, Phys. Rep. **121** (1985) 1.

[56] J.M.Greene, J.L.Johnson, Phys. Fluids **5** (1962) 510.

[57] O.Motojima, T.Mutoh, M.Sato, H.Zushi, H.Okada, N.Noda, H.Kaneko, T.Mizuuchi, K.Kondo, S.Sudo, Y.Takeiri, F.Sano, K.Itoh, S.Morimoto, K.Hanatani, K.Akaishi, Y.Yanagi, S.Besshou, S.Kobayashi, S.Iima, K.Ichiguchi, M.Wakatani, T.Obiki, A.Iiyoshi, in 12th Int. Conf. on Plasma Physics and Controlled Nuclear Fusion Research (Nice, 1988) CN-50/E-1-4.

[58] J.L.Johnson, J.M.Greene, B.Coppi, Phys. Fluids **6** (1963) 1169.

[59] S.Morimoto, N.Yanagi, M.Nakasuga, T.Obiki, A.Iiyoshi, K.Uo, Nucl. Fusion **28** (1988) 1491.

[60] G.Rewoldt, M.Wakatani, J.L.Johnson, Plasma Phys. and Controlled Nucl. Fusion **29**(1987) 1643.

[61] H.Sugama, M.Wakatani, J. Phys. Soc. Jpn. **58** (1989) 1128.

[62] H.Zushi, O.Motojima, M.Wakatani, F.Sano, S.Sudo, H.Kaneko, K.Kondo, T.Mizuuchi, K.Yaguchi, M.Sato, A.Iiyoshi, K.Uo, Nucl. Fusion **27** (1987) 895.

[63] H.Zushi, F.Sano, K.Itoh, T.Mizuuchi, H.Kaneko, S.Sudo, M.Nakasuga, K.Hanatani, K.Kondo, K.Ichiguchi, M.Harada, M.Wakatani, T.Obiki, A.Iiyoshi, *'The effects of the magnetic axis shift on transport and MHD Stability in Heliotron E', in Proc. of 7th International Workshop on Stellarators, Apr. 10-14, Oak Ridge*, 1989.

[64] S.Morimoto, N.Yanagi, S.Sato, S.Kobayashi, M.Iima, S.Besshou, H.Nakamura, M.Nakasuga, K.Hanatani, T.Obiki, A.Iiyoshi, Nucl. Fusion **29** (1989) 1697.

[65] S.Morimoto, N.Yanagi, K.Ichiguchi, S.Sato, M.Wakatani, T.Obiki, A.Iiyoshi, *'MHD Instabilities and Maximum β value in Heliotron DR', in Proc. of 7th International Workshop on Stellarators, Apr. 10-14, Oak Ridge*, 1989.

[66] K.Ichiguchi, Y.Nakamura, M.Wakatani, *'Resistive Instabilities in Heliotron E and Heliotron DR', in Proc. of U.S. Japan Workshop on Theoretical Problems with Non-Axisymmetric Toroidal Configurations, Oct. 16-20, Kyoto*, 1989.